# Hydraulic stability of Cubipods on gentle slopes with an impermeable core

## A physical model study motivated by the IJmuiden breakwater reconstruction

CIEM0500 Master thesis

Peter Ramondt

Delft University of Technology

TU Delft

Rijkswaterstaat
*Ministerie van Infrastructuur en Waterstaat*

# Hydraulic stability of Cubipods on gentle slopes with an impermeable core

## A physical model study motivated by the IJmuiden breakwater reconstruction

by

Peter Ramondt

In partial fulfilment of the degree of Master of Science

at the Delft University of Technology,

to be defended publicly on Wednesday July 8, 2026 at 3:00 PM.

| | | |
|---|---|---|
| Student number: | 4800176 | |
| Project duration: | February 1, 2025 – July 8, 2026 | |
| Thesis committee: | dr. ir. B. Hofland, | TU Delft (Chair) |
| | prof. dr. ir. M.R.A. van Gent, | TU Delft & Deltares |
| | ir. S.G. van den Berg | Rijkswaterstaat |
| | ir. A. Casteleijn | Rijkswaterstaat |

Cover: Photograph of an experiment with Cubipods in the wave flume.

An electronic version of this thesis is available at `http://repository.tudelft.nl/`.

TU Delft

Rijkswaterstaat
*Ministerie van Infrastructuur en Waterstaat*

# Preface

This thesis is the final work to finish my Master's degree in Civil Engineering. My Bachelor's thesis at Delft University of Technology was based on laboratory experiments at the hydraulic engineering lab, looking at the flow of plastic particles in front of hydraulic structures. Working in the laboratory inspired me and made me want to do more.

This thesis was carried out in collaboration with Rijkswaterstaat, who are responsible for the upcoming IJmuiden breakwater reconstruction. It is written for their reconstruction team and for anyone interested in concrete armour units on gentle slopes with impermeable cores.

Starting my experiments, I expected the Cubipods to be more stable on 1:2 and 1:3 slopes than on 1:1.5 slopes due to a larger gravity component pushing the Cubipods into the slope. The experiments showed the opposite. This means Cubipods require a more conservative design value on the IJmuiden cross-section than initially expected. This came as a surprise to me, and my supervisors had not expected the gentler slopes to be less stable either. It shows why physical model experiments are important: without them, the IJmuiden design could have been based on assumptions that turn out to be wrong. The experiments have made me even more enthusiastic about hydraulic engineering, breakwaters, and wave-structure interaction. During my thesis, I worked across CAD design, 3D printing, embedded systems for the instrumented rocking Cubipods, wave-flume experimentation, 3D photogrammetry, and the data analysis behind it all. This has been an incredible learning experience, and I am proud of my thesis.

This work would not have been possible without the help and support of my supervisors: Bas Hofland, Stefan van den Berg, Arnaud Casteleijn, and Marcel van Gent. I would also like to thank SATO for providing the Cubipods used for testing, and Antonio Corredor for coming to Delft from Spain to give valuable advice. Furthermore, I would like to thank the lab staff for providing much needed help with setting up my laboratory experiments, developing the 3D-printed Cubipod units, and building the breakwater model. Finally, thanks to my family and my girlfriend for supporting me on this journey.

*Peter Ramondt*
*Delft, July 2026*

# Summary

The Southern Breakwater in IJmuiden has suffered persistent damage at the roundhead and parts of the trunk, with significant displacement of armour units at wave heights well below the original design conditions. Rijkswaterstaat is planning a permanent reconstruction of the armour layer at the outer end of the Southern Breakwater. The structure has an impermeable asphalt-like core, with the slope locally as flat as $\cot\alpha = 4.5$ at the roundhead. One of the reconstruction options under consideration is a fill that brings this slope to $\cot\alpha = 3$. This combination of an impermeable core with such a gentle slope sits outside the calibration range of standard design guidelines, which were developed for steeper slopes on permeable rubble-mound cores. The applicability of standard armour units, including Cubipods, to this geometry has therefore not been established.

This thesis investigates the hydraulic stability of single-layer Cubipod armour on the trunk, at $\cot\alpha = 2$ and $\cot\alpha = 3$ slopes on an impermeable core. These slopes match the post-fill reconstruction geometry and a steeper reference. The programme comprised 22 two-dimensional physical model tests in the TU Delft Hydraulic Engineering Laboratory wave flume, across six configurations: single-layer Cubipod on the 1:2 and 1:3 slopes with $t_f = 0.5\,D_n$ and $1.0\,D_n$ underlayers (A1 to A4), single-layer cubes on the 1:3 slope (C1), and a double-layer Cubipod on the 1:3 slope (B1). In each test the wave height was raised step by step, in $2$ cm increments of the target $H_{m0}$, at a fixed wave steepness $s_{m-1,0} = 0.04$, covering incident wave heights $H_{m0,\text{inc}}$ from approximately $7$ to $20$ cm with a JONSWAP spectrum. Damage was recorded as the dimensionless count $N_{od}$ at the initiation of damage (IDa, first extracted unit) and at the initiation of destruction (IDe, $N_{od} = 0.2$ for single-layer, $2.0$ for double-layer). Five units carried custom-built embedded rocking sensors with on-board inertial measurement units, developed specifically for this study to record angular velocities throughout each test.

The 1:3 slope had lower stability than the 1:2 slope. The mean stability number at IDe, pooled over the $0.5\,D_n$ and $1.0\,D_n$ underlayers, was $N_s = 3.21$ on $\cot\alpha = 2$ and $3.00$ on $\cot\alpha = 3$. The Hudson formula predicts a $14\,\%$ gain on the flatter slope. It does not hold here. Translating the laboratory data to design values yielded $N_{sd} = 1.98$ on $\cot\alpha = 2$ and $N_{sd} = 1.81$ on $\cot\alpha = 3$, set in both cases by the initiation of damage. Single-layer cubes on the matched 1:3 impermeable cross-section (series C1) gave $N_{sd} = 1.62$ through the same framework, with a stricter no-damage margin applied because cubes are more brittle. Cubes show the same sensitivity, so the slope-related decrease is not specific to Cubipods. Failure on the 1:3 slope developed as a rapidly progressive collapse in which tens of units were extracted across five to eight rows around the still water line within a single wave-height step.

Doubling the underlayer from $0.5\,D_n$ to $1.0\,D_n$ did not improve stability on either slope. One test at the supplier-recommended placement porosity of $n_v = 42\,\%$ failed at the lowest tested wave height, motivating a tighter placement specification. Rocking, measured around the still water line, increased with wave height. On the 1:3 slope more rocking corresponded to more damage, while on the 1:2 slope no such relationship was found. The rocking signal tracked the overall damage at the structure level but did not identify which individual units would be extracted. A first-order structural-fatigue analysis based on the recorded impact velocities indicates that rocking-induced fracture is not expected to be a limiting failure mode at the design $N_{sd}$.

For the tested 1:3 impermeable trunk cross-section, the results support a design stability number of $N_{sd} = 1.8$. This holds for a single-layer placement at a maximum placement porosity of $n_v \leq 41\,\%$ on a $0.5\,D_n$ underlayer. The benchmark Cubipod Manual permeable design value of $N_s = 2.62$ cannot be transferred to this cross-section without a combined slope and core permeability correction. The IJmuiden Southern Breakwater is more low crested than the model tested here. Dedicated 2D tests on the low-crested IJmuiden geometry are still required to determine the optimal design. The roundhead, with locally gentler slopes and oblique wave attack, falls outside the present 2D scope and requires dedicated 3D basin testing before Cubipods can be specified for that part of the structure.

# Nomenclature

## Abbreviations

| Abbreviation | Definition |
|---|---|
| ARC | Active Reflection Compensation |
| CAU | Concrete Armour Unit |
| DAQ | Data Acquisition |
| IDa | Initiation of Damage |
| IDe | Initiation of Destruction |
| IDe,s | Initiation of Destruction, single-layer armour ($N_{od} = 0.2$) |
| IDe,d | Initiation of Destruction, double-layer armour ($N_{od} = 2.0$) |
| IMU | Inertial Measurement Unit |
| JONSWAP | Joint North Sea Wave Observation Project (spectrum) |
| MEMS | Micro-Electro-Mechanical System |
| RMS | Root Mean Square |
| SF | Safety Factor |
| SWL | Still Water Level |
| VN | Virtual Net (method) |

## Roman symbols

| Symbol | Definition | Unit |
|---|---|---|
| $a$ | Centre-to-centre distance between units in one row (placement grid) | [m] |
| $b_{\text{horiz}}$ | Horizontal distance between consecutive placement rows | [m] |
| $b_{\text{slope}}$ | Distance between row centres measured along the slope surface | [m] |
| $B$ | Flume width | [m] |
| $D$ | Palmgren-Miner cumulative fatigue damage sum | [–] |
| $D_e$ | Equivalent dimensionless damage (Virtual Net method) | [–] |
| $D_n$ | Nominal diameter of armour unit ($= (M/\rho_c)^{1/3}$) | [m] |
| $D_{n15}, D_{n50}, D_{n85}$ | Nominal diameters describing the underlayer rock grading | [m] |
| $f_{ck}$ | Characteristic concrete compressive strength | [MPa] |
| $Fr$ | Froude number | [–] |
| $g$ | Gravitational acceleration | [m/s$^2$] |
| $h$ | Still water depth | [m] |
| $h_{toe}$ | Water depth at structure toe | [m] |
| $H_{m0}$ | Spectral significant wave height | [m] |
| $H_{m0,\text{inc}}$ | Incident spectral significant wave height | [m] |
| $H_{1/3}$ | Significant wave height (zero-crossing) | [m] |
| $I$ | Moment of inertia | [kg m$^2$] |

| Symbol | Definition | Unit |
|---|---|---|
| $K_D$ | Hudson stability coefficient | [–] |
| $K_r$ | Reflection coefficient | [–] |
| $L$ | Wavelength | [m] |
| $L_0$ | Deep-water wavelength based on peak period $T_p$ | [m] |
| $L_{m-1,0}$ | Deep-water wavelength based on $T_{m-1,0}$ | [m] |
| $M$ | Mass of armour unit | [kg] |
| $n$ | Number of repetitions or data points in a sample | [–] |
| $n_L$ | Geometric scale factor ($L_p/L_m$) | [–] |
| $n_v$ | Placement porosity of the armour layer | [–] |
| $N_{\text{ext}}$ | Number of extracted units within a strip of width $B$ | [–] |
| $N_{od}$ | Damage number (extracted units per strip of width $D_n$) | [–] |
| $N_s$ | Stability number ($H_{m0}/\Delta D_n$) | [–] |
| $N_{sd}$ | Design stability number | [–] |
| $N_w$ | Number of waves per test step | [–] |
| $P$ | Notional permeability parameter (Van der Meer, 1988) | [–] |
| $R_c$ | Crest freeboard | [m] |
| $R_{u,2\%}$ | 2% exceedance run-up level | [m] |
| $Re$ | Reynolds number | [–] |
| $s_{m-1,0}$ | Wave steepness ($H_{m0}/L_{m-1,0}$) | [–] |
| $t_f$ | Underlayer (filter) thickness | [m] |
| $T_{m-1,0}$ | Spectral wave period ($m_{-1}/m_0$) | [s] |
| $T_p$ | Peak wave period | [s] |
| $v_i$ | Rocking impact velocity | [m/s] |
| $W$ | Weight of armour unit | [N] |
| $W_{\parallel}, W_{\perp}$ | Downslope and normal components of armour unit weight | [N] |
| $z_{\text{armour}}$ | Elevation of the armour crest above the flume floor | [m] |
| $z_{\text{plank}}$ | Elevation of the impermeable core crest above the flume floor | [m] |
| $z_{\text{toe}}$ | Elevation of the structure toe above the flume floor | [m] |

# Greek symbols

| Symbol | Definition | Unit |
|---|---|---|
| $\alpha$ | Slope angle (measured from horizontal) | [rad] or [°] |
| $\beta$ | Dimensionless wave parameter $(h/L_0)(H_I/L_0)$ for reflection | [–] |
| $\gamma$ | JONSWAP peak enhancement factor | [–] |
| $\Delta$ | Relative buoyant density ($(\rho_c - \rho_w)/\rho_w$) | [–] |
| $\Delta\theta$ | Rotation amplitude per rocking event | [°] |
| $\mu$ | Mean of the Gaussian stability distribution | [–] |
| $\nu$ | Kinematic viscosity of water | [m$^2$/s] |
| $\xi_{m-1,0}$ | Iribarren number ($\tan\alpha/\sqrt{s_{m-1,0}}$) | [–] |
| $\rho_c$ | Density of armour unit (concrete) | [kg/m$^3$] |
| $\rho_r$ | Density of underlayer rock | [kg/m$^3$] |
| $\rho_w$ | Density of water | [kg/m$^3$] |
| $\sigma$ | Standard deviation of the Gaussian stability distribution | [–] |
| $\omega$ | Angular velocity (absolute) | [°/s] |
| $\omega_s$ | Signed angular velocity (rocking signal) | [rad/s] or [°/s] |

# Contents

# 1

# Introduction

## 1.1. Context

In the Netherlands, the responsibility for protection against flooding lies with Rijkswaterstaat, the executive agency of the Ministry of Infrastructure and Water Management. The agency manages the main road network, the national waterway network and the main water systems, including the coastal defences and the breakwaters that protect the major port entrances (Rijkswaterstaat, 2024). One of the assets currently requiring intervention is the Southern Breakwater at IJmuiden, which protects the entrance to the Port of Amsterdam and the adjacent Tata Steel facilities. The outer 350 meters of this breakwater, comprising the straight trunk and the exposed roundhead, form the section under consideration for reconstruction. Figure 1.1 illustrates the location of the breakwater relative to the Netherlands, and Figure 1.2 shows an aerial view of the structure.

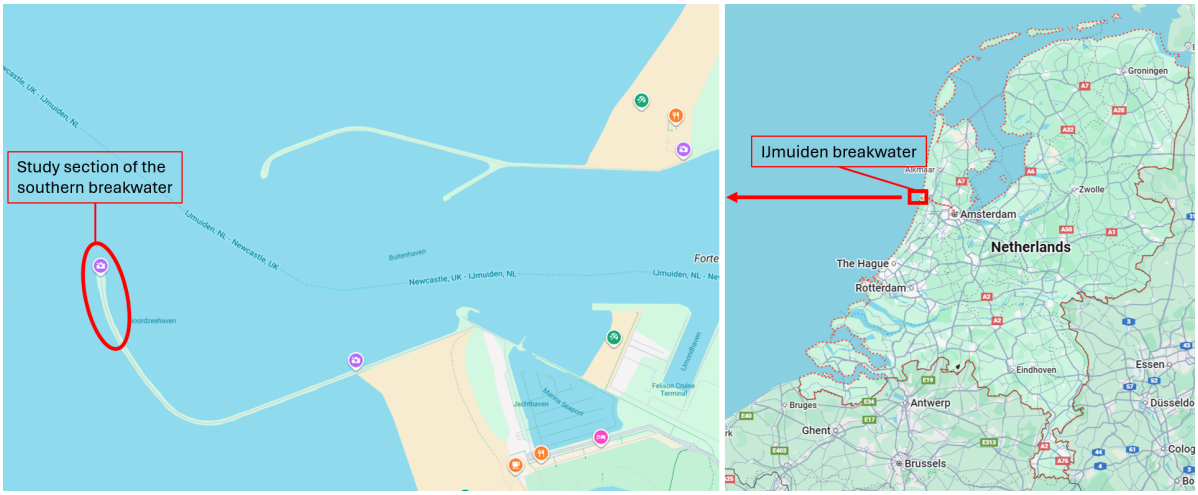


**Figure 1.1:** Left: a zoom-in of the IJmuiden port entrance, with the research area (trunk and head) encircled. Right: a map of the Netherlands highlighting the North Sea Canal entrance. Map data from (Google, 2026).

**Figure 1.2:** Aerial view of the Southern Breakwater at IJmuiden, with the port and the town of IJmuiden in the background. Drone photograph by R. Bruins (Rijkswaterstaat), 2025.

The southern breakwater was reconstructed in the 1960s with an impermeable asphalt protection layer, chosen at the time as a modern and cost-efficient alternative to concrete armour units (Van den Berg et al., 2024). However, the structure has suffered from chronic instability. Despite repeated reinforcement efforts over the last decade, including the placement of concrete blocks and extensive patching, damage persists. Significant damage occurs even during storms with wave heights of 3.5–4 m, well below the design wave height of 7.5 m (Van den Berg et al., 2024). Rijkswaterstaat has concluded that the current cycle of repair is unsustainable and that a robust, permanent reconstruction of the armour layer is required (Rijkswaterstaat, 2023). Figure 1.3 displays the state of the structure following storm damage in 2023.

**Figure 1.3:** The Southern Breakwater at IJmuiden showing the configuration of asphalt and armour blocks. This image was taken in 2023 following storm damage. Repairs have since been executed (Rijkswaterstaat, 2023).

The reconstruction will replace the damaged protection with a layer of concrete armour units. Rijkswaterstaat is evaluating several unit types for this purpose, including concrete cubes, Xbloc units and

Cubipod units (Rijkswaterstaat, 2023). The present thesis focuses on Cubipods. The final roundhead design will require three-dimensional physical model tests to capture diffraction and refraction effects, but the basic feasibility of the armour unit must first be established in two dimensions. This thesis therefore studies the cross-sectional stability of a Cubipod armour layer representative of the breakwater trunk, and provides the physical basis needed before future 3D basin tests by Rijkswaterstaat.

## 1.2. Research problem

While standard design guidelines exist for armour layers, they are predominantly based on structures with steep, permeable cores. The case of IJmuiden deviates on two aspects: the gentle slope, locally as flat as $\cot\alpha = 4.5$ at the roundhead and brought to $\cot\alpha = 3$ by the reconstruction fill, and the impermeable core. The impermeable core is expected to reduce internal energy dissipation and to increase wave reflection, run-down velocities and uplift pressures. The gentle slope reduces the along-slope gravity component that presses the units together, which is expected to weaken the interlocking between units. Together these two aspects alter the dominant failure mechanisms compared to conventional permeable rubble mound breakwaters. For this initial assessment, the problem is studied in two dimensions, focusing on the cross-sectional stability of the breakwater trunk. While modern bulk units like Cubipods present a promising solution due to their robustness and high friction (Medina and Gómez-Martín, 2016), their performance has not been experimentally verified for this specific configuration. Without fundamental experimental data, any design proposal for the IJmuiden breakwater carries a high degree of uncertainty regarding hydraulic stability and failure modes.

## 1.3. Research questions

The main research question is formulated as:

> *How do Cubipod armour units perform on gentle slopes (1:2, 1:3) with an impermeable core in terms of hydraulic stability and failure mechanisms?*

This main question is answered through the following sub-questions:

1. How does the stability of the Cubipod armour layer compare between a 1:2 slope and the gentler slope of 1:3?
2. How does the stability of Cubipods on the 1:2 reference slope compare to the performance of cubes tested under the same conditions by Ruijter (2026)?
3. How does the thickness of the granular underlayer, expressed as a fraction of the top-layer armour unit nominal diameter $D_n$, affect the hydraulic stability and settlement of the armour layer in the tested configurations?
4. What are the dominant failure mechanisms on gentle slopes with an impermeable core, and do they differ from those observed on steeper, permeable structures?

## 1.4. Approach

The research questions are answered with two-dimensional physical model tests in a wave flume. Physical model testing is chosen because no validated design rules exist for this combination of a gentle slope and an impermeable core, and physical tests are the established way to obtain stability numbers and to observe the failure mechanisms of a new armour configuration directly. The aim of the experimental programme is to quantify the hydraulic stability of Cubipod armour units on gentle slopes with an impermeable core and to identify the governing failure mechanisms for the tested configurations. The outcome consists of experimentally derived design stability numbers ($N_{sd}$) and a qualitative classification of failure mechanisms, which together provide a physical basis for assessing the feasibility of Cubipods in the reconstruction of the IJmuiden breakwater.

The test programme covers four single-layer Cubipod configurations (1:2 and 1:3 slope, each with a $0.5\,D_n$ and a $1.0\,D_n$ underlayer, where $D_n$ is the nominal diameter of the top-layer Cubipod armour units), a double-layer Cubipod configuration on the 1:3 slope (B1), and a single-layer cube reference series on the 1:3 slope (C1). Throughout this thesis, cube refers to single-layer, regularly placed cubes (also called paved cubes), as opposed to the conventional randomly placed double-layer cubes. The

comparison with cubes on the 1:2 slope draws on the results of Ruijter (2026) for cubes on the same impermeable cross-section, complemented by the C1 reference series on the 1:3 slope.

The stability and failure behaviour of these configurations is assessed through the following primary measurements:

- Damage assessment by direct counting of the extracted units in the flume, supported by photographs and synchronised video recordings (top-view GoPro, occasional side-view iPhone clips, and rocking sensors, all time-aligned). Details in chapter 4.
- Photogrammetric reconstruction of the armour slope for the double-layer test (B1), producing displacement maps per wave-height step. The method allows gaps and damage extent to be quantified spatially and is reported in section 5.2.6.
- Rocking and failure detection: Cubipods with embedded rocking sensors measure unit movement, building on the laboratory's experience with this technology (Hofland et al., 2023). The angular-velocity signals are processed into individual rocking events, from which the event count, the event rate per 1000 waves, and the peak angular velocity per event are analysed as a function of the stability number (chapter 5).

## 1.5. Research scope

The scope of the experimental programme is limited to the hydraulic stability of the armour layer. The following boundaries and simplifications apply:

- **2D flume testing (trunk focus):** The experiments are conducted in a 2D wave flume and simulate the cross-section of the breakwater trunk under perpendicular wave attack. Perpendicular long-crested waves are more demanding than the oblique, short-crested attack that the actual structure experiences, so the 2D trunk configuration is conservative in this respect. The roundhead is outside the scope and requires dedicated 3D basin tests.
- **Test configurations:** Two underlayer thicknesses are tested on each slope ($0.5\,D_n$ and $1.0\,D_n$ single-layer Cubipod, with $D_n$ the nominal diameter of the top-layer armour units, four A-configurations in total). The programme is complemented by one double-layer Cubipod test on the 1:3 slope (B1) and a three-repetition cube reference series on the 1:3 slope (C1).
- **Toe structure:** The toe of the model is designed to be robust and placed at a sufficient depth to prevent toe failure from acting as the initiating failure mechanism. Detailed toe design is excluded.
- **Deep-water conditions:** The seabed is idealised as a horizontal plane, and the model simulates deep-water wave attack to exclude foreshore interactions, local scour and shoaling from the scope. Deep water is conservative relative to a gently sloping shallow foreshore, where depth-induced breaking limits the highest individual waves so that the maximum wave height for a given significant wave height is lower.

## 1.6. Thesis outline

The theoretical background on armour stability, slope and permeability effects, and rocking measurement is presented in chapter 2. The model setup, test configurations, and test procedure are described in chapter 3. The instrumentation, including the wave gauges, rocking sensors, and damage assessment method, is detailed in chapter 4. The experimental results, stability curves, failure mechanisms, and rocking sensor data, are presented in chapter 5. The findings are discussed in the context of existing design guidance and the IJmuiden case in chapter 6. The conclusions and recommendations for design and future research are given in chapter 7.

# 2

# Theoretical framework

This chapter presents the theoretical background for analysing the hydraulic stability of Cubipod armour units on gentle impermeable slopes.

## 2.1. Rubble mound breakwaters

Rubble mound breakwaters dissipate wave energy through wave breaking on the slope, friction within the armour layer, and infiltration into the porous core (Rock Manual, 2007). On impermeable cores, infiltration is absent. Wave rundown concentrates along the slope surface, increasing uplift and outward forces on the armour.

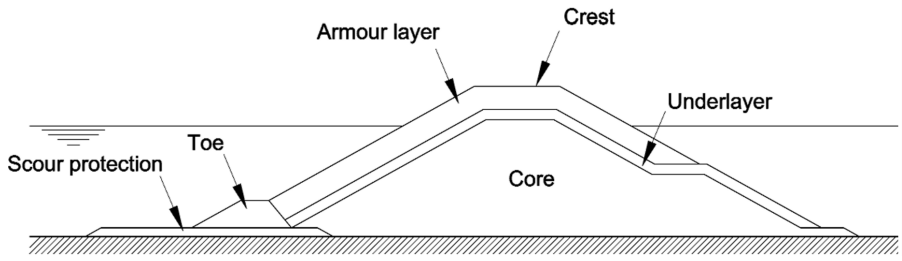


**Figure 2.1:** Typical rubble mound breakwater cross-section. Source: (Rock Manual, 2007).

## 2.2. Failure modes

A rubble mound breakwater can fail through several distinct mechanisms (figure 2.2): armour erosion or breakage, capping-wall sliding or tilting, slip failure of the slope, berm and toe erosion, filter instability, and core or subsoil settlement. The figure depicts a generic rock-armoured cross-section, but the mechanisms apply equally to a breakwater armoured with concrete armour units. The present thesis treats only the hydraulic stability of the armour layer under wave loading, specifically for single- and double-layer Cubipod and cube units. Toe failure, overtopping, capping-wall response and geotechnical mechanisms are explicitly out of scope (section 1.5). The figure is included to make this scope boundary visible to the reader.

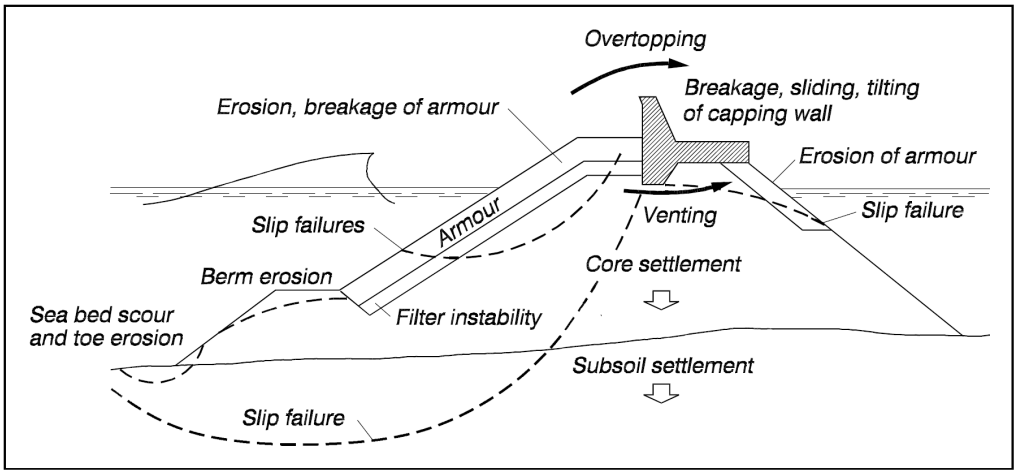


**Figure 2.2:** Failure modes of a rubble mound breakwater (rock-armoured cross-section, but the mechanisms apply to concrete armour units as well). The present thesis covers armour erosion and breakage only. The other mechanisms shown are out of scope. Source: (Burcharth, 1992), reproduced in (CEM, 2006).

## 2.3. Armour stability

The hydraulic stability of armour layers is expressed using the stability number:

$$N_s = \frac{H_{m0}}{\Delta\, D_n} \tag{2.1}$$

with the relative buoyant density $\Delta = (\rho_c - \rho_w)/\rho_w$ and $D_n$ the nominal diameter of the armour unit. A higher $N_s$ means the armour is subjected to relatively larger waves for a given unit size.

Damage is quantified using the damage number:

$$N_{od} = \frac{N_{\text{ext}}}{B/D_n} \tag{2.2}$$

where $N_{\text{ext}}$ is the number of extracted units within a strip of width $B$ along the breakwater (Van der Meer, 1988). Two limit states are used throughout this thesis, both defined in terms of $N_{od}$:

- Initiation of damage (IDa): the first extracted unit, that is, the smallest non-zero damage ($N_{od} > 0$).
- Initiation of destruction (IDe): $N_{od} = 0.2$ for single-layer armour, written IDe,s, and $N_{od} = 2.0$ for double-layer armour, written IDe,d (Rock Manual, 2007; Van der Meer, 1988). Where the layer type is clear from the context the general term IDe is used.

The double-layer threshold is ten times higher because the second layer provides redundancy: the upper layer can lose a number of units before the lower layer is exposed. How these thresholds are detected in the experiments, the number of extracted units they represent for the present model, and the reasons for the chosen values are given in section 3.3.[1]

For concrete armour units, the design size is often set with the Hudson stability coefficient $K_D$ (Hudson, 1959). Using the design $K_D$ in Hudson's relation gives the design stability number:

$$N_{sd} = \left(K_D\, \cot\alpha\right)^{1/3} \tag{2.3}$$

where $\alpha$ is the slope angle. A higher $K_D$ allows for smaller and lighter units at a given slope. The same relation, used in reverse, gives the $K_D$ that corresponds to a measured stability number (the back-calculation reported in section G.2). This single coefficient is adequate for randomly placed rock

[1] This extraction-count definition of IDe is supplemented in one tested case. In repetition A1_R2 destruction was reached through a large-scale sliding mechanism, in which the armour and the underlayer shifted downslope together and opened gaps larger than several $D_n^2$ while $N_{od}$ remained near zero. This exception to the $N_{od}$-based criterion is described in chapter 5 and chapter A.

and for double-layer units (Hudson, 1959), but not for single-layer interlocking units such as Cubipods, whose stability does not scale with $(\cot\alpha)^{1/3}$ on slopes flatter than about $\cot\alpha = 1.5$ (Medina and Gómez-Martín, 2016; Delta Marine Consultants, 2024) (section 2.4.1). Stability is therefore expressed in $N_s$ throughout this thesis, and the back-calculated $K_D$ values are reported only as a methodological exercise in section G.2.

Table 2.1 gives an overview of the design stability number $N_{sd}$ and the safety factors for several concrete armour units, as reported by Medina et al. (2012). The design $K_D$ values given there are converted to $N_{sd} = (K_D \cot\alpha)^{1/3}$ for consistency with the rest of this thesis. These values are based on tests with slopes of 1:1.5 (cubes, Cubipods) and 1:1.33 (Accropode, Xbloc). The safety factors express the ratio between the stability number at a given limit state and the design stability number $N_{sd}$. A value greater than 1.0 means the design wave height is below the limit state.

**Table 2.1:** Design stability number $N_{sd}$ and global safety factors to initiation of destruction (IDe) and initiation of damage (IDa). The $N_{sd}$ column is converted from the design $K_D$ of Medina et al. (2012) as $N_{sd} = (K_D \cot\alpha)^{1/3}$. Source: (Medina et al., 2012).

| | | | | | Initiation of Destruction (IDe) | | Initiation of Damage (IDa) | |
|---|---|---|---|---|---|---|---|---|
| Section | CAU | $N_{sd}$ | # layers | slope | SF (IDe5%) | SF (IDe50%) | SF (IDa5%) | SF (IDa50%) |
| Trunk | Cube | 2.08 | 2 | 3/2 | 1.05 | 1.35 | 0.67 | 0.86 |
| | Cubipod 2 | 3.48 | 2 | 3/2 | 1.09 | 1.40 | 0.82 | 0.99 |
| | Cubipod 1 | 2.62 | 1 | 3/2 | 1.31 | 1.64 | 1.06 | 1.27 |
| | Accropode | 2.71 | 1 | 4/3 | 1.05 to 1.40 | 1.26 to 1.51 | 0.93 to 1.24 | 1.15 to 1.38 |
| | Xbloc | 2.77 | 1 | 4/3 | 1.17 | 1.68 | 1.17 | 1.32 |
| Roundhead | Cube | 1.96 | 2 | 3/2 | 1.17 | 1.40 | 0.88 | 1.13 |
| | Cubipod 2 | 2.19 | 2 | 3/2 | 1.19 | 1.36 | 0.99 | 1.18 |

For double-layer armours the safety factors to IDa are close to or below 1.0, meaning the design wave height is near the start of damage. This is acceptable because double-layer armours have a gradual failure with a large margin between IDa and IDe. For single-layer armours, the safety factors to IDa are well above 1.0 because single-layer armours fail more suddenly, requiring a larger margin between the design condition and IDe (Medina et al., 2012).

The Cubipod Manual quantifies armour damage using the equivalent dimensionless damage $D_e$, derived from the Virtual Net (VN) method (Gómez-Martín and Medina, 2014). The VN method measures volumetric porosity changes in the armour layer by projecting a virtual net over the slope surface, capturing unit settlement and compaction as well as displacement. As a result, $D_e$ rises as soon as the layer begins to compact, before any unit is visually displaced. Like $N_{od}$, $D_e$ expresses damage as an equivalent number of units extracted per unit strip width, but it also folds in the settlement and compaction of the layer (the heterogeneous-packing contribution), so it does not equal a simple count of extracted units. For single-layer Cubipods, initiation of damage is defined within the band $1.0 < D_e < 2.0$, taken as $D_e \approx 1.6$ (Medina and Gómez-Martín, 2016). This value represents the state at which the first units are extracted near the water line together with measurable settlement and porosity increase in the most active strip, rather than $1.6$ units physically removed.

The present study uses $N_{od}$ rather than $D_e$. $N_{od}$ counts only visually extracted units per unit strip width and does not capture settlement. This makes $N_{od}$ directly comparable with the stability curves of Van der Meer (1988) and the design criteria in the Rock Manual (Rock Manual, 2007), which serve as the primary reference for comparison in this study. Because $N_{od}$ does not detect the early compaction phase, it responds later than $D_e$: by the time $N_{od}$ registers damage, the armour has already deteriorated further. For this study, where the results must be comparable with the broader armour stability literature, $N_{od}$ is the appropriate metric.

## 2.4. Stability influence factors

Beyond the armour unit itself, several features of the cross-section influence the stability of the armour layer. This section reviews the influence of slope angle, core permeability, water depth, crest height, and foreshore.

### 2.4.1. Slope angle

A steeper slope increases the downslope gravity component on the armour units:

$$W_{\parallel} = W \sin\alpha, \qquad W_{\perp} = W \cos\alpha \tag{2.4}$$

A gentler slope reduces $W_{\parallel}$ relative to $W_{\perp}$, which increases the frictional resistance between the units and the slope surface. However, the slope also controls the wave breaking type, characterised by the Iribarren number (Battjes, 1974):

$$\xi_{m-1,0} = \frac{\tan\alpha}{\sqrt{s_{m-1,0}}} \tag{2.5}$$

where $s_{m-1,0} = H_{m0}/L_{m-1,0}$ is the wave steepness. Low $\xi$ (gentle slopes, short waves) produces plunging breakers with high impact forces. High $\xi$ (steep slopes, long waves) produces surging breakers with lower impacts (Figure 2.3). On a gentler slope these effects act in opposite directions. The smaller downslope gravity component increases the friction holding the units on the slope, which is stabilising. The shift towards plunging breakers increases the wave impact, which is destabilising. For interlocking units a third effect is added: a gentler slope reduces the interlocking between units, which is destabilising. Which effect dominates depends on the unit type, the slope and the waves, so the net change in stability cannot be read from the slope angle alone.

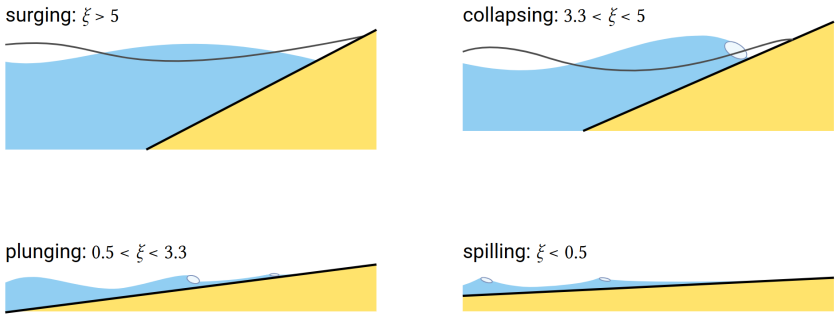


**Figure 2.3:** Breaker type classification as function of Iribarren number. Source: adapted from (Bosboom and Stive, 2023).

Van der Meer (1988) accounted for this by using separate stability formulas for plunging and surging conditions. The Hudson formula (Equation (2.3)) captures slope angle only through $\cot\alpha$, implying a monotonic increase in stability for gentler slopes. This does not account for the change in breaker regime (Van der Meer, 1988).

For single-layer concrete armour units that rely on interlocking, the slope dependence is different. The Cubipod Manual and the Xbloc guidelines both state that the $(\cot\alpha)^{1/3}$ scaling of Hudson's formula does not hold for single-layer interlocking units, and that on flatter slopes the unit weight should not be reduced by this factor (Medina and Gómez-Martín, 2016; Delta Marine Consultants, 2024). The Rock Manual makes the same point from the other side: it notes that stability does not increase on slopes gentler than 1:2 for these units ((Rock Manual, 2007), Table 5.35, note 8).

This statement is made for interlocking units in general. The Cubipod Manual, however, describes the Cubipod itself as a massive unit that gains its stability mainly from friction rather than from interlocking, and it does not state whether Hudson scaling applies to Cubipods specifically. The Manual is therefore silent on this exact point, which leaves a gap that this thesis fills with its own reasoning.

The present thesis treats the Cubipod as a substantially interlocking unit. It does not interlock through slender hooked legs like Xbloc or Accropode, but through its bulky body and protruding faces: under wave load the units are pushed against their neighbours and press harder against one another, so

the layer holds together as a whole rather than resisting the wave force unit by unit. Two distinct contact mechanisms are involved and should not be confused: the friction between a unit and the slope surface beneath it, and the friction and pressing between neighbouring units (the interlocking). A post-test observation supports the interlocking reading. After the double-layer test, when the top layer had already been removed and only the bottom layer remained, lifting one bottom-layer unit by hand raised a cluster of about thirty neighbouring units with it, while at a looser packing the same pull moved no neighbours (described in detail in chapter 6). The Cubipod therefore sits between cubes, which derive stability mainly from gravity and friction, and slender interlocking units such as Xbloc and Accropode, which derive it mainly from interlocking. Because the Cubipod interlocks substantially, the no-Hudson-scaling reasoning for interlocking units is taken to apply to it, while the absence of slender legs means its interlocking is weaker than that of Xbloc or Accropode.

The current Xbloc design guidelines go one step further than the Manual: rather than treating slope-independence as a neutral observation, they apply an explicit weight penalty for slopes outside the recommended range, with a correction factor of $1.25$ on the armour weight for slopes milder than $\cot\alpha = 1.5$ and $1.5$ for slopes milder than $\cot\alpha = 2$, on the grounds that on a mild slope the interlocking of the armour units is less effective and stability is reduced (Delta Marine Consultants, 2024). These and the other local phenomena the Xbloc guidelines quantify are summarised in table 2.2. As the only published quantification for an interlocking concrete armour unit, the Xbloc penalty is used here as an indicative upper-bound reference for Cubipod, not as direct evidence for the unit. The slope penalty should apply to Cubipods at least partially, but no equivalent quantitative correction has been published. Experimental confirmation for cubes is provided by van Buchem (2009), who tested single-layer cubes on $\cot\alpha = 1.5$ and $\cot\alpha = 2.0$ and reported that the steeper slope was more stable. The cubes on the gentler slope showed less along-slope compaction, weaker friction-based interlocking and therefore relied more on the underlayer for stability. van Buchem (2009) also attributes part of the lower stability on the gentler slope to the breaker regime: the milder slope produces plunging breakers with a higher impact load. This runs against the classical expectation, based on the gravity argument of Van der Meer (1988), that cubes and Cubipods become more stable on gentler slopes. The same opposing result is found for Cubipods in the present study and is interpreted further in section 6.1.1. No experimental stability data is *published* for any concrete armour unit on slopes flatter than $\cot\alpha = 2$. The Xbloc slope correction implies that such data exists in-house at the supplier, but it is not available in the open literature.

**Table 2.2:** Correction factors on the armour unit weight for local phenomena that affect the required unit size, as defined in the Xbloc design guidelines. Source: (Delta Marine Consultants, 2024), Table 5-3.

| Phenomenon | Effect on armour stability | Xbloc | XblocPlus |
|---|---|---|---|
| Frequent occurrence of near-design wave height during the lifetime | Rocking of units, which occurs for a small percentage of units during the design event, can become frequent over the design life. Rocking should be carefully assessed in physical model tests. | 1.25 | n.a. (rocking not observed in tests) |
| Steep foreshore | Concentrates wave energy and increases impact forces on the armour layer. | 1.1 (1:30 to 1:20)<br>1.25 (1:20 to 1:15)<br>1.5 (1:15 to 1:10)<br>2.0 (steeper than 1:10) | same as Xbloc |
| Low-crested structure | Units on the crest and high on the slope lack overburden from above-lying rows, so water line interlocking is weaker, and the crest area sustains direct wave impacts. | 1.5 for $R_c/H_s < 1$<br>2.0 for $R_c/H_s < 0.5$ | 1.25 for $R_c/H_s < 1$<br>1.5 for $R_c/H_s < 0.5$ |
| Large water depth | In deep water $H_{\max}/H_s$ reaches $1.8$–$2.0$ versus $1.2$–$1.4$ nearshore, so the larger spectral tail drives higher armour loads. Rocking should be carefully assessed. | 1.5 for $h > 2.5\,H_s$<br>2.0 for $h > 3.5\,H_s$ | n.a. (validated by deep-water tests for $N_s > 2.5$) |
| Low core permeability | High pressures build up in the armour layer and outward forces on the units increase. | 1.5 for low permeability<br>2.0 for impermeable core | 1.25 low<br>1.5 impermeable |
| Mild armour slope ($\cot\alpha > 1.5$) | Interlocking is less effective on milder slopes, so stability is reduced. | 1.25 for slope milder than $\cot\alpha = 1.5$<br>1.5 for slope milder than $\cot\alpha = 2$ | n.a. (no decrease observed in tests) |

### 2.4.2. Impermeable cores

On a permeable breakwater, part of the wave energy enters the core as flow and is dissipated by turbulence inside the structure. On an impermeable core this mechanism is absent: all wave energy must be dissipated on the slope surface. This increases wave runup and rundown velocities and results in larger hydraulic loads on the armour units (Rock Manual, 2007).

For rock armour, Van der Meer (1988) quantified this effect through the notional permeability parameter $P$ (Figure 2.4). An impermeable core with a thin underlayer corresponds to $P = 0.1$, while a standard rubble mound with a permeable core has $P = 0.4$ to $0.5$. In his stability formulas for rock, reducing $P$ from 0.5 to 0.1 lowers the stability number $N_s$ by roughly 30 to 40% for the same damage level (Van der Meer, 1988).

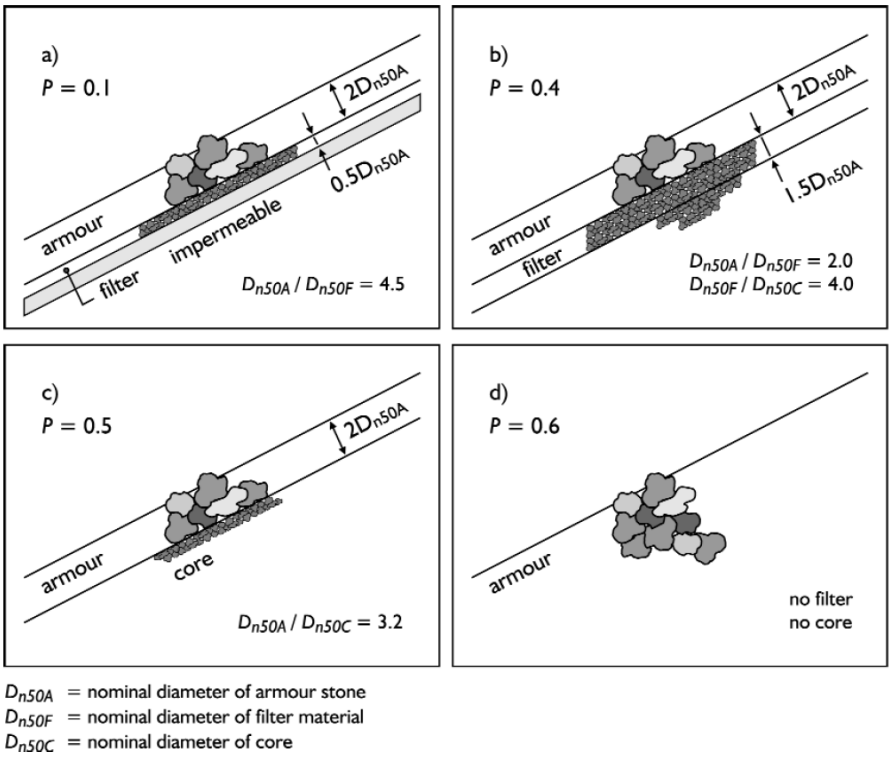


**Figure 2.4:** Notional permeability parameter $P$ for different breakwater cross-sections, defined for rock armour stability formulas. Source: (Van der Meer, 1988), reproduced in (Rock Manual, 2007).

The notional permeability parameter $P$ is defined for rock armour and does not directly apply to concrete armour units. However, Reedijk et al. (2008) investigated the effect of core permeability on the stability of several armour types and quantified the required increase in $D_{n50}$ when going from a permeable to an impermeable core. Using the Van der Meer formulas for rock ($P = 0.6 \rightarrow 0.1$), the required $D_{n50}$ increases by 38–190% depending on the wave conditions. Van Gent et al. (2003) found a 59% increase for rock under the same permeability change. For Accropode units, Burcharth et al. (1998) reported a 46% increase when reducing $P$ from 0.4 to 0.2. Most relevant to the present study, Reedijk et al. (2008) found that single-layer concrete cubes on the IJmuiden breakwater cross-section ($P' = 0$, no filter layer) require a 78% larger $D_n$ compared to a conventional rubble mound with a permeable core ($P = 0.4$). This confirms that core permeability is a significant parameter for concrete armour units, even though it is not included in $K_D$-based design methods.

All published Cubipod stability tests have been performed with permeable cores (Medina and Gómez-Martín, 2016). The effect of an impermeable core on Cubipod stability has not been investigated.

Díaz-Carrasco et al. (2020) give a further reason why the slope angle or Iribarren number alone is not enough on impermeable slopes. From dimensional analysis and model tests on impermeable slopes ($\cot\alpha = 2$, 3 and 10), they show that the way wave energy splits into reflection, transmission and dissipation depends on the product $(h/L)(H_I/L)$ together with the slope angle, not on the Iribarren number on its own. The same Iribarren value can give different breaker types and different energy splits. This is a known limit of the surf-similarity parameter, and it supports the view that Hudson-style scaling cannot describe armour on impermeable cores across different slopes.

Table 2.3 summarises the available stability data for concrete armour units and rock, organised by slope and core permeability. The table makes the literature gap visible: no experimental stability data exists for any concrete armour unit on slopes flatter than $\cot\alpha = 2$ in combination with an impermeable core, and only limited data exists for the impermeable case on $\cot\alpha = 2$.

**Table 2.3:** Reported stability values $H_s/D_n$ for concrete armour units and rock, by slope and core permeability. Values use $\Delta = 1.4$ for concrete and $\Delta = 1.65$ for rock and are not directly applicable to other densities. The present thesis values use $\Delta = 1.30$ for Cubipods and $\Delta = 1.24$ for cubes. Values for permeable cores are design or experimental ranges from the cited sources. Shaded cells mark the impermeable-core configurations tested in this thesis. They are left empty here and filled in the results chapter (table 6.1), where the present measurements and the matched cube comparison of Ruijter (2026) are reported together with their damage-level conventions. The Ruijter cube data on the $\cot\alpha = 2$ impermeable cross-section are laboratory values without a safety factor and are therefore not listed alongside the design-basis values in this table. Empty cells indicate no published data. $s_{op} = 0.04$ assumed.

| Unit type | Core | $\cot\alpha = 1.5$ | $\cot\alpha = 2$ | $\cot\alpha = 3$ | Source |
|---|---|---|---|---|---|
| Rock | permeable ($P = 0.5$) | 1.44[g] | 1.66[g] | 2.04[g] | (Van Gent et al., 2003; Rock Manual, 2007) |
| Rock | impermeable ($P = 0.1$) | 1.08[g] | 1.25[g] | 1.53[g] | (Van Gent et al., 2003; Rock Manual, 2007) |
| Cubes (1 layer) | permeable | 2.2–2.3 | 2.2–2.3 | — | (Van Gent et al., 2000) |
| Cubes (1 layer) | impermeable | — | — | — | chapter 5 |
| Cubipod (1 layer) | permeable | 2.62[a] | 2.62[b] | 2.62[b] | (Medina and Gómez-Martín, 2016) |
| Cubipod (1 layer) | impermeable | — | — | — | chapter 5 |
| Cubipod (2 layer) | permeable | 3.48[a] | 3.48[b] | 3.48[b] | (Medina et al., 2012) |
| Xbloc (1 layer) | permeable | 2.8 | 2.60[e] | 2.45[e] | (Delta Marine Consultants, 2024) |
| Xbloc (1 layer) | impermeable | 2.22[f] | 2.06[e,f] | 1.94[e,f] | (Delta Marine Consultants, 2024) |
| Tetrapod (2 layer) | permeable | 2.3 | 2.5 | 2.9 | (Rock Manual, 2007) |

[a] Cubipod Manual $K_D = 12$ (single layer) and $K_D = 28$ (double layer) via Hudson. [b] Manual claim of no Hudson scaling beyond $\cot\alpha = 1.5$. [e] Xbloc Manual slope correction. [f] Xbloc Manual impermeable-core correction. [g] Rock from the Van Gent et al. (2003) plunging-wave formula. The footnote letters match those of table 6.1. How each value is obtained is set out in section 2.4.3.

### 2.4.3. Derivation of the literature stability values

The values in table 2.3 come from different sources and conventions, which are set out here so the comparison is transparent.

The Cubipod values are the Cubipod Manual design values: $K_D = 12$ for the single layer and $K_D = 28$ for the double layer, converted to $N_s$ through Hudson's relation at $\cot\alpha = 1.5$. The Manual states that this stability does not scale with slope for these units, so the same value is listed across slopes.

The Xbloc values are derived from the Xbloc Manual permeable design value at $\cot\alpha = 1.5$ ($N_s = 2.8$) by applying the Manual weight-correction factors, $N_s = 2.8/(\text{factor})^{1/3}$. The slope correction is $1.25$ for slopes milder than $\cot\alpha = 1.5$ and $1.5$ for slopes milder than $\cot\alpha = 2$, and the impermeable-core correction is a factor $2$ on the weight. The permeable rows apply only the slope factor. The impermeable rows apply the core factor and the slope factor together (so $\cot\alpha = 1.5$ uses $2$, $\cot\alpha = 2$ uses $2 \times 1.25$, and $\cot\alpha = 3$ uses $2 \times 1.5$). The Xbloc Manual itself recommends applying only the single highest factor for an initial estimate, which for an impermeable structure is the core factor of $2$ and gives $N_s = 2.22$ on every slope. The combined values are listed here as an indicative reference, because the present tests show a real slope effect that the single-factor rule does not capture (see section 6.1.5).

The single-layer cube values are for the regularly placed type ($n_v \approx 0.25$, one face flat on the underlayer), matching the present C1 series and (Ruijter, 2026). The $\cot\alpha = 1.5$ value (Van Gent et al., 2000) is taken via Rock Manual (2007) Table 5.35, whose note 8 adds that stability does not increase on slopes gentler than 1:2. Randomly placed double-layer cube values are omitted because that placement convention is not comparable with the single-layer regularly placed cubes tested here. The impermeable-core cube data (Reedijk et al., 2008; Ruijter, 2026) are reported in chapter 5.

The rock values are computed from the Van Gent et al. (2003) stability formula for plunging waves ((Rock Manual, 2007) Eq. 5.139) at the $5\,\%$ characteristic coefficient $c_{pl} = \mu - 1.64\sigma = 7.25$ (with $\mu = 8.4$, $\sigma = 0.7$), using start of damage $S_d = 2$, $N = 1000$ waves, $s_{m-1,0} = 0.04$, and the deep-water Rayleigh distribution $H_{2\%}/H_s = 1.4$. This gives a deterministic design value comparable to the Cubipod $N_{sd}$ obtained from the Medina (2012) safety factors.

### 2.4.4. Water depth

The relative water depth at the toe of a breakwater controls the maximum wave height that can reach the armour layer. In nearshore conditions the foreshore limits the largest waves in the spectrum to roughly $H_{\max}/H_s \approx 1.2$–$1.4$. In deep water no such limitation applies and the ratio rises to $1.8$–$2.0$ (Delta Marine Consultants, 2024). Because the largest waves in the spectrum drive the dominant armour loads, a deep-water cross-section experiences a higher peak hydraulic load at a given $H_s$ than a shallow-water cross-section.

The Xbloc design guidelines (Delta Marine Consultants, 2024) apply an increasing weight penalty for deep water, up to $2.0$ for $h > 3.5\,H_s$ (table 2.2), and flag that rocking should be carefully assessed in deep water. The reason is that in deep water the highest waves in the sea state are not limited by the water depth, so a larger fraction of big waves reaches the structure and these drive the strongest rocking impacts. No equivalent quantitative correction is published for Cubipods. The present test programme operates near $h \approx 3.5\,H_s$ at design conditions and therefore corresponds to the deep-water regime in which Xbloc applies its largest correction. Because deep water gives the highest waves for a given $H_s$, testing in this regime is conservative. IJmuiden also has relatively deep water at the structure, so the present results are representative for it rather than optimistic. This is relevant for both the stability interpretation and the rocking analysis in chapter 5.

### 2.4.5. Crest height

The armour rows placed above the still water line provide an overburden load on the underlying rows: their self-weight presses the water line units together and against the slope, increasing the contact forces between neighbouring units and thereby their interlocking. This stabilising contribution scales with the relative freeboard $R_c/H_s$. For low-crested structures the overburden is reduced and the water line units rely more on self-interlocking and gravity alone, which lowers their stability. The Xbloc design guidelines (Delta Marine Consultants, 2024) apply a weight penalty for low-crested structures, up to $2.0$ for $R_c/H_s < 0.5$ (table 2.2).

The IJmuiden Southern Breakwater is low-crested at design conditions, whereas the present model includes a higher relative freeboard to keep the armour fully covered across the wave-height range. The crest height affects the armour in more than one way. The higher lab crest carries more overburden above the water line than the prototype, which presses the upper rows down and may bias the measured stability of those rows upward. The high crest also lets almost no water overtop, so all run-up water has to drain back down over the armour face, adding a downrush load that a low-crested, overtopping structure partly avoids. On a low-crested structure the upper rows near the crest also become more exposed and more vulnerable. These competing effects are revisited in the discussion of limitations (section 6.5).

### 2.4.6. Foreshore

The slope of the foreshore in front of the breakwater controls wave shoaling and the type of breaker that reaches the armour layer. On a steep foreshore the water deepens quickly towards the structure, so the waves shoal over a short distance and lose little energy before they break on the armour. This gives larger and more impulsive waves at the toe than a long, gentle foreshore, where the waves break and lose energy further out. A steep foreshore therefore increases the loads on the armour. The Xbloc design guidelines (Delta Marine Consultants, 2024) apply an increasing weight penalty for steeper foreshores, from $1.1$ at $1{:}30$ to $2.0$ for slopes steeper than $1{:}10$ (table 2.2).

The present test programme uses a horizontal seabed (foreshore correction factor $1.0$), consistent with the deep-water idealisation adopted in the model setup (section 1.5). The IJmuiden prototype is fronted by a mild foreshore that does not trigger a penalty under this scheme, so this factor is not a concern for the prototype extrapolation but is reported here for completeness.

## 2.5. Cubipod armour units

Cubipods are massive concrete armour units designed to combine the structural strength of cubes with higher hydraulic stability (Medina and Gómez-Martín, 2016). Their geometry increases the friction and contact between neighbouring units, so they interlock through their bulky body rather than through slender interlocking elements.

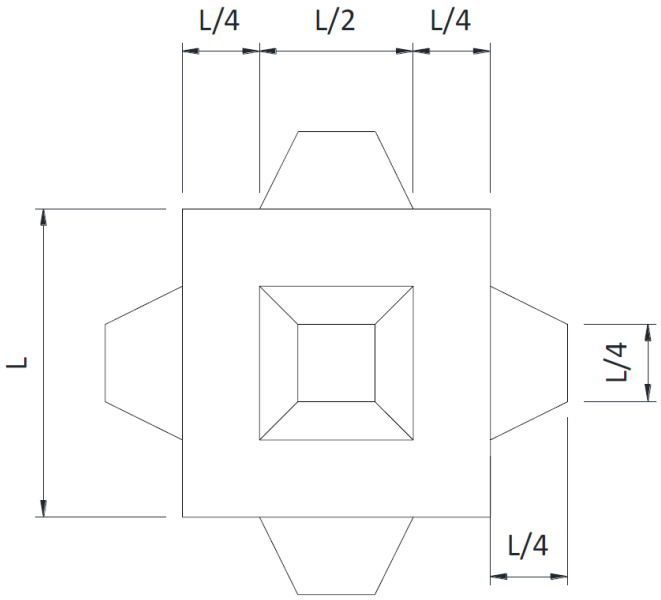


**Figure 2.5:** Cubipod geometry and principal dimensions. Source: (Medina and Gómez-Martín, 2016).

Cubipods can be placed in single-layer or double-layer configurations. Cubes, by comparison, are typically placed in double-layer configurations and have lower hydraulic stability: on a 1:1.5 slope, the design stability number for double-layer Cubipods ($N_{sd} = 3.48$) is much higher than for cubes ($N_{sd} = 2.08$) (Medina et al., 2012). For single-layer Cubipods on a 1:1.5 slope, $N_{sd} = 2.62$ (Medina and Gómez-Martín, 2016).

Placement method and porosity affect stability. Cubipods are placed following a diamond-type placement grid, where each unit in a row is positioned between two units of the row below. The grid is defined by two parameters measured on a horizontal plane: $a$, the distance between centres of adjacent units in the same row, and $b$, the horizontal distance between consecutive rows (Medina and Gómez-Martín, 2016). Figure 2.6 shows a conventional grid (left) and a progressive grid (right). In the progressive grid, the row spacing decreases towards the top of the slope to compensate for downward settlement due to compaction during placement. Pardo et al. (2014) used realistic placement tests with small-scale crawler cranes and pressure clamps to determine the optimum grids for Cubipods and showed that porosity control is important for achieving the design hydraulic performance.

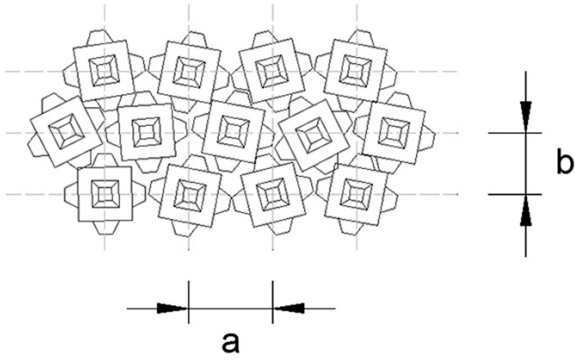


**(a)** Conventional placement grid.

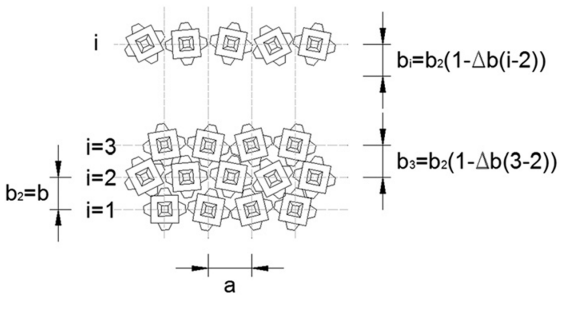


**(b)** Progressive placement grid.

**Figure 2.6:** Cubipod placement grids. The conventional grid (left) uses fixed row spacing $b$. The progressive grid (right) uses decreasing row spacing toward the crest to account for wave-driven settlement during crane construction. Source: (Medina and Gómez-Martín, 2016).

## 2.6. Rocking and motion sensors

Armour units under wave attack can undergo rocking: rotational oscillations around contact points with neighbouring units. When a rocking unit impacts a neighbour, the impact velocity determines whether structural damage can occur. For interlocking single-layer units such as Xbloc and Accropode, rocking-induced breakage is a known failure mechanism (Hofland et al., 2023). For massive units such as cubes and Cubipods, breakage is less of a concern, but rocking still indicates incipient instability before units are displaced.

Rocking has traditionally been assessed by visual observation, counting the percentage of moving units during a test. This is subjective and difficult around the water line (Hofland et al., 2023). Hofland et al. (2023) developed an alternative method using low-cost MEMS-based inertial measurement units (IMUs) embedded inside armour units. The sensors measure the angular velocity $\omega$ in three axes, from which the absolute rotation rate is computed:

$$|\omega| = \sqrt{\omega_x^2 + \omega_y^2 + \omega_z^2} \tag{2.6}$$

The sensor logs data to an SD card only when the rotation rate exceeds a threshold, so each recorded signal corresponds to a rocking event. From the recorded angular velocity, the rocking impact velocity (the rotational velocity just before the unit strikes a neighbour) can be determined. This requires a much lower sampling frequency than measuring the acceleration during the short-duration impact itself (Hofland et al., 2023). A typical recorded event shows an uprush peak, a downrush peak, and a bounce-back (Figure 2.7).

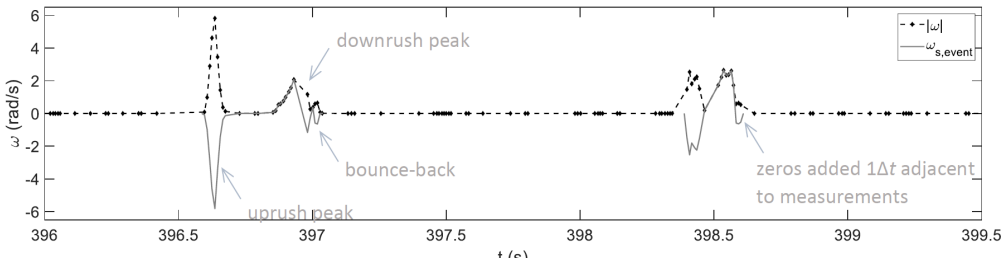


**Figure 2.7:** Typical angular velocity signal of a rocking event, showing uprush peak, downrush peak, and bounce-back. Dashed line: absolute rotation rate $|\omega|$. Solid line: automatically derived rocking event signal $\omega_s$. Source: (Hofland et al., 2023).

Following Hofland et al. (2023), the absolute rotation rate is given a sign so that the two phases of a rocking cycle can be separated. The signed rocking signal is:

$$\omega_s = |\omega| \operatorname{sign}(\omega_j) \tag{2.7}$$

where $\omega_j$ is the angular-velocity component with the largest variance, that is, the dominant rocking axis with the highest signal-to-noise ratio, so that the uprush rotation and the following downrush rotation appear as two peaks of opposite sign. Because gravity acts downslope, the upward rocking occurs later in the uprush and the downward rocking early in the downrush, so the first peak of a closely spaced pair is taken as the uprush. A complete rocking event comprises one uprush peak and one downrush peak and is counted as a single event. Equivalently, the number of detected peaks is divided by two. This convention is adopted in the present thesis, so that one event corresponds to one wave-driven rocking cycle rather than to an individual impact, which keeps the event count comparable to a per wave rocking rate.

This method provides objective, quantitative data on the number and intensity of rocking events per unit, which is more sensitive than visual observation or displacement-based damage numbers ($N_{od}$). The same method is adopted in the present thesis to measure the rocking response of Cubipod armour units.

## 2.7. Physical modelling and scaling

Physical model tests of breakwaters require geometric, kinematic, and dynamic similarity between the model and the prototype. Here prototype means the full-scale structure, the standard term in hydraulic

engineering for the real, built-size breakwater (as opposed to the scaled-down flume model). Gravity and inertia are the dominant forces in wave-structure interaction, so Froude scaling is applied (Rock Manual, 2007):

$$Fr = \frac{u}{\sqrt{gL}} \tag{2.8}$$

With a geometric scale factor $n_L = L_p/L_m$, all other quantities follow from Froude similarity (Table 2.4).

**Table 2.4:** Scale factors according to Froude scaling.

| Variable | Unit | Scale factor |
|---|---|---|
| Length | $L$ | $n_L$ |
| Area | $L^2$ | $n_L^2$ |
| Volume | $L^3$ | $n_L^3$ |
| Time | $T$ | $n_L^{0.5}$ |
| Velocity | $L/T$ | $n_L^{0.5}$ |
| Mass | $M$ | $n_L^3$ |

Viscous and surface tension forces are not scaled but must remain negligible. Flow through the armour layer must be turbulent, which is checked with the Reynolds number (Rock Manual, 2007):

$$Re = \frac{\sqrt{gH_{m0}} \cdot D_n}{\nu} > 3 \times 10^4 \tag{2.9}$$

The Rock Manual states this stability-Reynolds criterion with the median nominal rock-armour diameter $D_{n50}$, because it was derived for quarry-stone armour. For the uniform concrete units used here the criterion is applied with the Cubipod nominal diameter $D_n$, which is the equivalent armour length scale. For a uniform armour the two coincide ($D_{n50} = D_n$). Surface tension effects (Weber number) can be neglected when the water depth is greater than 5 cm, the significant wave height is greater than 5 cm, and the wave steepness is realistic (Rock Manual, 2007).

The stability number must be the same in model and prototype:

$$\left(\frac{H_{m0}}{\Delta\, D_n}\right)_m = \left(\frac{H_{m0}}{\Delta\, D_n}\right)_p \tag{2.10}$$

Because model tests typically use fresh water instead of salt water, the relative density $\Delta$ can differ between model and prototype. This is compensated by adjusting the unit size or density so that the stability numbers match.

## 2.8. Previous Cubipod research

Table 2.5 summarises the existing experimental research on Cubipod armour units. The majority of studies cover steep slopes (1:1.5) with permeable cores. The Cubipod Manual (Medina and Gómez-Martín, 2016) includes data for slopes up to 1:2. Only Corredor et al. (2012) tested a 1:2 slope in a 3D configuration.

## 2.9. Research gap

The literature reviewed in the preceding sections shows three combined gaps relevant to the IJmuiden Southern Breakwater configuration:

1. No experimental stability data exists for any single-layer concrete armour unit on slopes flatter than $\cot\alpha = 2$. The few values listed for flatter slopes in table 2.3 are design-rule figures for double-layer units on permeable cores, not measurements. The Cubipod Manual (Medina and Gómez-Martín, 2016) and the Xbloc design guidelines (Delta Marine Consultants, 2024) restrict their recommended slope range to $\cot\alpha = 4/3$ to $3/2$ and either state that flatter slopes do not yield additional stability for interlocking units or apply explicit weight penalties for them. These sources, together with the Rock Manual (Rock Manual, 2007), all state that gentler slopes add

**Table 2.5:** Summary of Cubipod experimental investigations.

| Subject | Tested slopes | Variables / measurement | Ref. |
|---|---|---|---|
| 2D hydraulic stability (trunk) | | | |
| Trunk stability benchmarks | 1:1.5 | $K_D$, $N_s$, $N_{od}$ damage curve, HeP via virtual net | (Gómez-Martín and Medina, 2009; Medina et al., 2012; Gómez-Martín and Medina, 2008; Medina and Gómez-Martín, 2016) |
| Gentle slope benchmark | 1:2.0 | San Andrés case study, 1/40 scale 3D test | (Corredor et al., 2012) |
| Depth-limited breaking | 1:1.5 | Horizontal foreshore ($m = 0$), regular waves | (Medina and Gómez-Martín, 2016; Gómez-Martín and Medina, 2008) |
| 3D hydraulic stability (roundhead) | | | |
| Standard roundhead tests | 1:1.5 | Sectorial damage ($90°$ to $135°$), laser profiling | (Lomonaco et al., 2010) |
| Short-crested wave attack | 1:1.5, 1:2.0 | Directionality effects, JONSWAP spectrum | (Burcharth et al., 2011; Sande et al., 2016) |
| Placement, porosity, and randomness | | | |
| Placement grids | 1:1.5, 1:2.0 | Placement grids ($G_x, G_y$), porosity | (Pardo et al., 2014; Medina et al., 2010a; Pardo et al., 2010) |
| Randomness quantification | N/A | Armour randomness index, laser scanning | (Pardo et al., 2012; Molines et al., 2014) |
| Hydraulic performance and overtopping | | | |
| Roughness factors | 1:1.5 | Roughness factor $\gamma_f$, CLASH database | (Molines et al., 2012; Medina and Gómez-Martín, 2016) |
| Crown wall stability | 1:1.5 | Horizontal and uplift forces, pressure sensors | (Molines and Medina, 2011) |
| Structural integrity | | | |
| Impact strength | N/A | Prototype drop tests (16 tonne), mass loss | (Medina et al., 2010b) |
| **This thesis** | **1:2, 1:3** | $N_{od}$ curves, rocking, impermeable core | **—** |

no stability for such units, but whether the Hudson slope correction $(\cot\alpha)^{1/3}$ actually holds, fails or reverses on an impermeable core has not been tested experimentally.

2. The effect of an impermeable core on Cubipod stability has not been investigated. Reedijk et al. (2008) quantified the impermeable-core penalty for cubes on the IJmuiden cross-section ($+78\%\ D_n$, equivalent to a $\sim 44\%$ reduction in $H_s/D_n$), Ruijter (2026) provided cube data on an impermeable cross-section at $\cot\alpha = 2$, but no equivalent dataset exists for Cubipods.
3. The combined effect of these two factors, a gentle slope on an impermeable core, falls outside the design range of all major single-layer concrete armour systems.

This thesis fills this combined gap by generating $N_{od}$-based stability curves for single-layer and double-layer Cubipods, and for cubes as a comparison case, on 1:2 and 1:3 slopes with an impermeable core.

# 3

# Research method

The research questions are answered through physical model tests in the 2D wave flume of the Hydraulic Engineering Laboratory at TU Delft. This chapter describes the model setup, test configurations, and test procedure. The instruments and measurement methods are described in chapter 4.

## 3.1. Purpose

This study determines the hydraulic stability of single-layer and double-layer Cubipod armour units on gentle slopes ($1{:}2$, $1{:}3$) with an impermeable core. Existing Cubipod stability data covers slopes up to $1{:}2$ only, and all of it with a permeable core (Medina and Gómez-Martín, 2016). The tests quantify the stability number $N_s$ at initiation of damage (IDa) and initiation of destruction (IDe), and the damage progression $N_{od}$ as a function of $N_s$, slope angle, layer configuration, and underlayer thickness ($0.5$ and $1 \times D_n$).

## 3.2. Parameters

All governing dimensional and dimensionless parameters are listed in table 3.1.

**Table 3.1:** Dimensional and dimensionless parameters. Values for $H_{m0,\text{inc}}$, $T_{m-1,0}$, $s_{m-1,0}$, $N_s$, $\xi$, $Re$ and $R_c/H_{m0,\text{inc}}$ are realised ranges measured at the structure toe (section B.5); the Iribarren and stability values are given per slope ($\cot\alpha = 2$ / $\cot\alpha = 3$). Throughout this thesis $D_n$ refers to the nominal diameter of the top-layer armour unit.

| Dimensional | | | | Dimensionless | | |
|---|---|---|---|---|---|---|
| Parameter | Symbol | Value | Unit | Parameter | Definition | Range |
| Sign. wave height | $H_{m0,\text{inc}}$ | 0.07–0.20 | m | Stability no. | $H_{m0,\text{inc}}/\Delta D_n$ | 1.7–4.6 |
| Spectral period | $T_{m-1,0}$ | 1.15–1.90 | s | Iribarren no. | $\tan\alpha/\sqrt{s_{m-1,0}}$ | 1.77 / 2.70 |
| Water depth | $h$ | 0.60 / 0.65 | m | Wave steepness | $s_{m-1,0}$ | 0.032–0.037 |
| Cubipod $D_n$ | $D_n$ | 0.0324 | m | Reynolds no. | $\sqrt{gH_{m0,\text{inc}}}\cdot D_n/\nu$ | 2.7 to $4.5\times10^4$ |
| Cube $D_n$ | $D_n$ | 0.031 | m | Rel. density | $(\rho_c-\rho_w)/\rho_w$ | 1.30 / 1.24 |
| Cubipod density | $\rho_c$ | 2300 | kg/m$^3$ | Damage no. | $N_d/(B/D_n)$ | 0–destr. |
| Cube density | $\rho_c$ | 2240 | kg/m$^3$ | Rel. freeboard | $R_c/H_{m0,\text{inc}}$ | 1.0–3.6 |
| Slope | $\cot\alpha$ | 2, 3 | – | | | |
| Waves per step | $N_w$ | ∼1000–1040 | – | Run duration | – | 24–35 min |
| Flume width | $B$ | 0.79 | m | | | |

## 3.3. Damage thresholds

The damage number $N_{od}$, the equivalent dimensionless damage $D_e$ from the Virtual Net method, and the reasons for using $N_{od}$ rather than $D_e$ are defined generically in section 2.3. This section gives the threshold values used in the present experiments and the reason for each choice:

- **IDa (initiation of damage):** $\boldsymbol{N_{od} > 0}$, taken as the first wave-height step at which at least one

extracted unit is detected on the post-step photograph. With $B/D_n \approx 23.5$ the smallest resolvable increment is one extracted unit ($N_{od} \approx 0.04$), which sets the practical detection limit.

- **IDe,s (initiation of destruction), single-layer:** $\boldsymbol{N_{od} = 0.2}$, about five extracted units for the present model width. This is the single-layer destruction threshold of the Rock Manual (Rock Manual, 2007) and is also used by Ruijter (2026) for cube tests on the same impermeable cross-section. It is chosen here so the present results are directly comparable with both.
- **IDe,d (initiation of destruction), double-layer:** $\boldsymbol{N_{od} = 2.0}$, counted over the double-layer armour as a whole, so extractions from either layer are included, ten times the single-layer value because the upper, sacrificial layer can erode while the lower layer stays in place as a reserve that keeps the core protected. This follows the double-layer convention of (Van der Meer, 1988) and the Rock Manual (Rock Manual, 2007).

Because the wave height is increased in steps, a threshold is never observed exactly. It is only known that it falls somewhere between the last step without the damage state and the first step with it. The stability number $N_s$ reported for IDa and IDe is therefore taken as the average of those two bracketing steps. This avoids overstating the stability that using the higher step alone would cause. The same approach is applied to the cube data of Ruijter (2026) so the two datasets are comparable.

The pre-test stability prediction used to set the wave-height range and unit size, and the Hudson-based IDa/IDe estimate it implied, are documented in section B.2.

## 3.4. Scale effects and unit selection

The model is Froude-scaled (see section 2.7). The tests are not built to one fixed prototype scale. They measure the stability of the armour as a dimensionless stability number $N_s$, which holds at any scale. The model unit size was therefore chosen for sound flow conditions in the flume (see below), not to match a particular prototype size.

A scale can still be quoted to give a sense of the size involved. The flume reaches a maximum wave height of $H_{m0,\text{model}} = 0.22\,\text{m}$. If that largest test wave is set equal to the IJmuiden design wave ($H_{s,\text{proto}} \approx 7.5\,\text{m}$), the scale factor is $n_L \approx 34$ and the model Cubipod ($D_n = 3.24\,\text{cm}$) corresponds to a prototype unit of about $1.1\,\text{m}$. This $1.1\,\text{m}$ is only a reference tied to the most extreme test, not the design unit size. The design condition is well below the most extreme test, so the actual prototype unit sized for it (with a safety margin) is larger. That prototype size is derived from the measured stability in section 6.4.1.

Three Cubipod sizes were available for model testing: $D_n = 2.43$ cm, $2.95$ cm, and $3.24$ cm. The largest unit ($D_n = 3.24$ cm, $\rho = 2300$ kg/m$^3$) was selected to minimise viscous scale effects. The Rock Manual (Rock Manual, 2007) requires $Re = \sqrt{gH_{m0}} \cdot D_n/\nu > 3 \times 10^4$ for turbulent flow around armour units. As table 3.2 shows, only the 3.24 cm units satisfy this criterion across the stability-critical wave height range. The 2.43 cm units fall well below the threshold.

**Table 3.2:** Reynolds numbers for the three available Cubipod sizes at representative wave heights.

| $H_{m0}$ [m] | $Re$ ($D_n$=2.43 cm) | $Re$ ($D_n$=2.95 cm) | $Re$ ($D_n$=3.24 cm) | Assessment |
|---|---|---|---|---|
| 0.10 | 24,100 | 29,200 | 32,100 | Only 3.24 cm $> 3 \times 10^4$ |
| 0.15 | 29,500 | 35,700 | 39,300 | 2.95 and 3.24 cm sufficient |
| 0.22 | 35,700 | 43,400 | 47,600 | All above threshold |

Additional scale-effect mitigation:

- Impermeable core: there is no porous flow through the core, so scale effects associated with permeable core flow do not apply. The configuration corresponds to $P = 0.1$ in the Van der Meer permeability classification.
- Surface tension: negligible ($H_{m0,min} = 5$ cm $\gg$ 2 cm threshold).
- Flume width: $B/D_n \approx 23$ units across the width, exceeding the minimum of 15 to avoid sidewall effects.

The model armour units, the comparison cubes, and the underlayer stones are shown together at scale in Figure 3.1.


**Figure 3.1:** Model materials at scale. From left to right: 3D-printed Cubipod replacement unit with internal cavity for the embedded rocking sensor (orange), SATO resin Cubipod (white) used as the standard armour unit ($D_n = 3.24$ cm, $\rho_s = 2300$ kg/m$^3$), concrete cube (yellow, $D_n = 3.1$ cm) used in the group C comparison tests, and quarry stones from the underlayer filter grading. A tape measure is included for scale. The central cube of the Cubipod has an edge length of approximately $30.5$ mm, almost equal to the $31$ mm edge of the comparison cube.

## 3.5. Model geometry

The model is constructed in the TU Delft 2D wave flume (width $B = 0.79$ m, wall height 1.005 m). A flat foreshore extends from the wave paddle to the structure toe. Two slopes are tested with different geometry, summarised in table 3.3.

**Table 3.3:** As-built geometry per slope configuration. All elevations $z$ are measured from the flume floor. $h$ is the still water depth over the flume floor and $h_{\text{toe}}$ the water depth above the toe. The wooden plank that supports the armour and underlayer extends to $z_{\text{plank}}$. The armour and underlayer themselves are placed up to $z_{\text{armour}}$, which sets the effective crest of the model and the freeboard. The parameters are defined in figures 3.2 and 3.3.

| Parameter | $\cot\alpha = 2$ | $\cot\alpha = 3$ |
|---|---|---|
| Water depth $h$ | 0.60 m | 0.65 m |
| Toe elevation $z_{\text{toe}}$ | 0.30 m | 0.40 m |
| Wooden plank crest $z_{\text{plank}}$ | 0.92 m | 1.10 m |
| Armour crest $z_{\text{armour}}$ | 0.92 m | 0.85 m |
| Water depth at toe $h_{\text{toe}}$ | 0.30 m | 0.25 m |
| Freeboard $R_c = z_{\text{armour}} - h$ | 0.32 m | 0.20 m |
| Slope length (armoured face) | $\sim$1.39 m | $\sim$1.43 m |

The as-built cross-section for the two slopes is shown in figures 3.2 and 3.3, which define the geometry parameters of table 3.3 on the model cross-section.

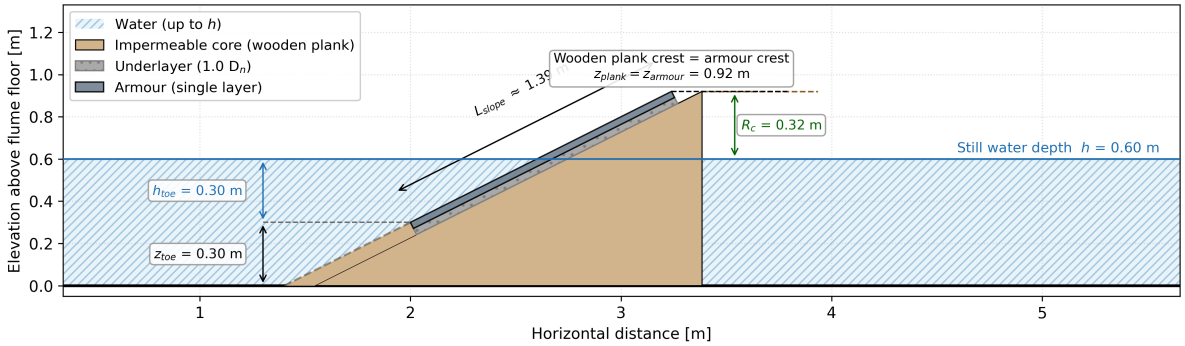


**Figure 3.2:** As-built model cross-section for the $1{:}2$ slope, defining the geometry parameters listed in table 3.3. All elevations $z$ are measured from the flume floor. $h$ is the still water depth and $h_{\text{toe}}$ the water depth above the toe. The impermeable wooden plank rises to the plank crest $z_{\text{plank}}$, while the single armour layer and the underlayer reach the armour crest $z_{\text{armour}}$. On this slope the plank crest and the armour crest coincide at 0.92 m.

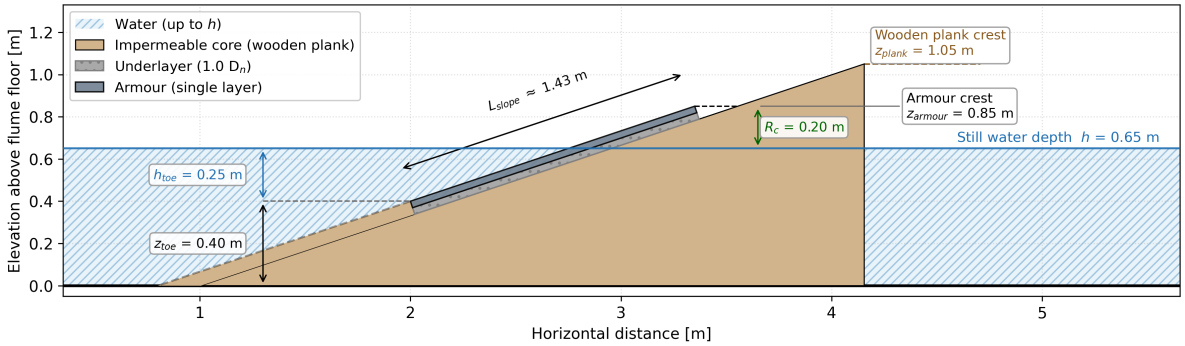


**Figure 3.3:** As-built model cross-section for the $1{:}3$ slope, defining the geometry parameters listed in table 3.3. All elevations $z$ are measured from the flume floor. $h$ is the still water depth and $h_{\text{toe}}$ the water depth above the toe. The impermeable wooden plank rises to the plank crest $z_{\text{plank}} = 1.10$ m, above the armour crest $z_{\text{armour}} = 0.85$ m to which the armour layer and the underlayer are placed.

The $1{:}2$ slope uses the same toe elevation and water depth as Ruijter (2026). On the $1{:}3$ slope the toe was raised to 0.40 m and the water depth to 0.65 m to keep the number of armour rows manageable: a constant vertical armour rise on the gentler slope would otherwise require roughly 60 rows instead of the 41 used in the actual setup. The wooden support plank still extends to 1.10 m, but the armour and underlayer are placed only up to 0.85 m so that the row count and the compaction effects associated with very long slopes remain comparable to the $1{:}2$ case. The full setup-evolution rationale is given in section A.1.1. Figure 3.4 shows a side view of the as-built $1{:}3$ slope with $t_f = 1.0\,D_n$ underlayer in place.

**Figure 3.4:** Side view of the as-built model with $\cot\alpha = 3$ slope and $t_f = 1.0\,D_n$ quarry-stone underlayer, photographed through the glass sidewall of the flume.

All structural components are listed in table 3.4. The underlayer thickness is varied as a test parameter: $0.5$ and $1 \times D_n$.

**Table 3.4:** Material dimensions, properties, and quantities. $D_n$ is the nominal diameter of the armour (top-layer) unit. The cube dimensions and density and the underlayer rock density are taken from (Ruijter, 2026).

| Component | Material | $D_n$ / thickness | $\rho$ [kg/m$^3$] | Quantity |
|---|---|---|---|---|
| Cubipod armour (1-layer) | Resin | $D_n = 32.4$ mm | 2300 | ∼2000 (total) |
| Cubipod armour (2-layer) | Resin | $2D_n = 64.8$ mm | 2300 | |
| Cube armour (C1) | Concrete | $D_n = 31$ mm | 2240 | 874 per test (46 × 19) |
| Underlayer | Rock | $D_{n50} = 11.3$ mm | 2660 | 21 / 42 L per test |
| Core | Wood | impermeable | – | – |

The underlayer material is natural rock with $\rho_r \approx 2660$ kg/m$^3$, $D_{n50} = 11.30$ mm, and a narrow grading $D_{n85}/D_{n15} = 1.31$ (figure 3.5). This is the same material used in Ruijter (2026), from which the density is taken and where the grading was verified to satisfy Rock Manual filter criteria for concrete armour units (Rock Manual, 2007). The full derivation is given there. The grading is equally valid for the present Cubipod units ($M_a \approx 78$ g): the median underlayer stone weighs about $3.8$ g, which is close to $M_a/20$ and therefore falls just inside the Cubipod Manual underlayer range of $M_a/10$ to $M_a/20$ (Medina and Gómez-Martín, 2016).

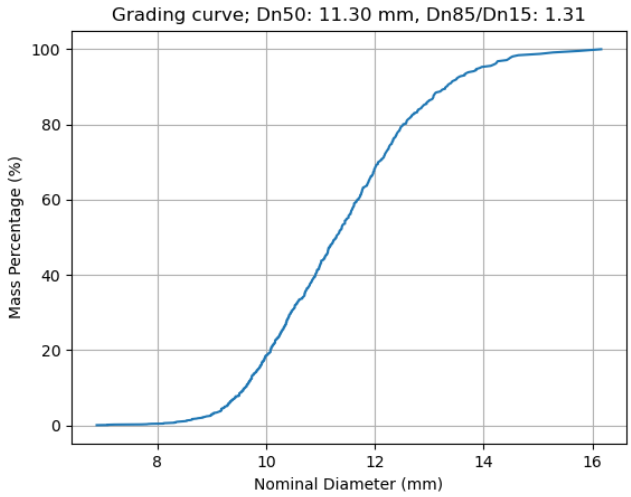


**Figure 3.5:** Grading curve of the underlayer material ($D_{n50} = 11.30$ mm, $D_{n85}/D_{n15} = 1.31$, $\rho_r \approx 2660$ kg/m$^3$). From (Ruijter, 2026).

The crest of the $1{:}2$ slope is at $z_{\text{armour}} = 0.92$ m, giving a freeboard $R_c = 0.32$ m above the still water level. On the $1{:}3$ slope the armour crest is at $z_{\text{armour}} = 0.85$ m ($R_c = 0.20$ m). Both armour crests sit below the flume wall ($z_{\text{wall}} = 1.005$ m), so the armour layer is fully contained within the wall height.

## 3.6. Armour rows

The gentle slopes produce long slope faces relative to the unit size. For the $1{:}2$ slope the armoured face is approximately 1.39 m long, giving 40 to 41 rows of Cubipods. For the $1{:}3$ slope the as-built face length is approximately 1.43 m, giving 41 rows. The toe elevation and armour crest on the $1{:}3$ setup were chosen specifically to keep the row count comparable to the $1{:}2$ case (section A.1.1). Without this adjustment a constant vertical armour rise would require roughly 60 rows on the gentler slope. Both values exceed the 15 to 25 rows typical of steep-slope ($1{:}1.5$) model tests recently reported in the literature, but the difference does not increase with slope angle as it would for a constant vertical rise.

A potential concern with many rows is progressive sliding of the armour mass as a body, driven by the accumulated self-weight of the units along the slope. This is a separate concern from the interlocking that resists removal of individual units: it is about the whole layer sliding down the slope. Two factors mitigate it on the present model. First, on a $1{:}3$ slope the gravity component normal to the slope is large relative to the downslope component ($\cos\alpha / \sin\alpha = 3$), so the units press onto the slope surface and are held there by friction more than they lean on the rows below. This resistance to whole-layer sliding grows on gentler slopes, so progressive sliding is less critical here than on the steeper $1{:}1.5$ slopes where most existing data originates. It does not mean the armour is more stable overall on the gentler slope: the interlocking that resists removal of individual units is weaker there, which is the dominant effect on stability (section 2.4.1). Second, the prototype IJmuiden breakwater is relatively low-crested and has a higher toe elevation than the model, so the actual number of rows in the full-scale structure will be smaller than in the present model. Whether the extra rows add stability is not straightforward. They add overburden that can press the water-line units together and aid compaction, but the rows high above the water line stay outside the damage zone and may not contribute to interlocking there. This trade-off, and what it means for a low-crested structure, is taken up in section 7.3. Compaction observations during the test programme are reported in section 5.1.1.

## 3.7. Armour placement procedure

Cubipods are placed in a diamond pattern defined by two spacings (see figure 3.6): $a$, the centre-to-centre distance within a row (parallel to the crest), and $b_{\text{slope}}$, the centre-to-centre distance between rows measured along the slope surface. The Cubipod Manual (Medina and Gómez-Martín, 2016) defines

the between-row spacing horizontally as $b_{\text{horiz}} = b_{\text{slope}} \cos\alpha$. The Cubipod Manual recommends a target as-built porosity of 40 to 43 % for single-layer armour.

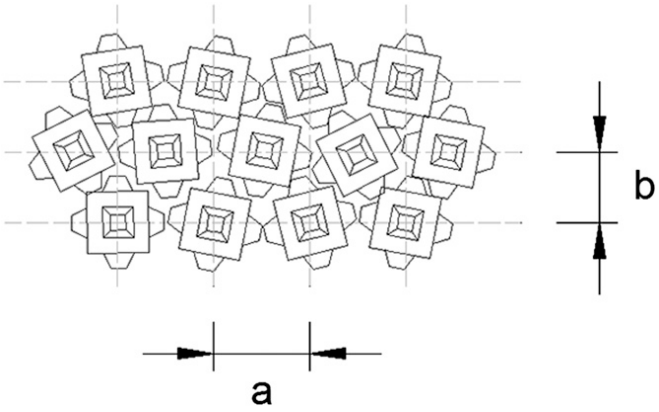


**Figure 3.6:** Diamond Cubipod placement grid with within-row spacing $a$ and between-row spacing $b$. Adapted from (Pardo et al., 2014).

The slope porosity is defined as the unit cross-section relative to the grid cell area, and can be written in two equivalent forms:

$$n_v \equiv 1 - \frac{D_n^2}{a\, b_{\text{slope}}} = 1 - \frac{1}{(a/D_n)\,(b_{\text{slope}}/D_n)} \tag{3.1}$$

The first form is the definition, the cross-sectional area $D_n^2$ of a unit relative to the grid-cell area $a\, b_{\text{slope}}$. The second is the algebraically identical form used in the Cubipod Manual (Medina and Gómez-Martín, 2016). Porosity is reported as a percentage ($n_v \times 100\,\%$).

The manufacturer-advised grid for the present setup ($a \approx 49.7$ mm, $b_{\text{slope}} \approx 37$ mm, target porosity approximately 42 %, at the upper bound of the Manual range) was tried first, in test A1_R2. With this between-row spacing adjacent rows did not make contact, so the armour could not transfer load between rows. The underlayer failed during the compaction run and the test was terminated.

From test A1_R3 onwards, the placement was modified in two respects. The within-row count was set at 15 and 16 units alternating per row, giving a constant within-row spacing of $a = 49.7$ mm. Each row was placed flush against the row below, with the front face of every unit physically touching the units of the preceding row. Under this procedure the between-row spacing $b_{\text{slope}}$ is not a controlled design parameter but emerges from the placement geometry. The measured range across all valid tests is $b_{\text{slope}} = 34$ to 36 mm. The as-built porosity ranges from 40.0 % to 40.5 % across the A1, A2, A3, and A4 configurations (table 3.5), at the low end of the Manual's recommended 40 to 43 % range and matching the 40.5 % porosity used in the Manual's published stability figures. The as-built grid parameters per configuration are listed in table 3.5. The full derivation and the trial-grid history are given in section A.3. Both the manufacturer-advised grid and the adopted grid were discussed and agreed with the manufacturer.

**Table 3.5:** As-built Cubipod placement grid parameters per configuration. The within-row count is the standard 15/16 alternating pattern except for the double layer (B1), where 16 units per row were used. The Manual reference row uses the crane-placement values from (Medina and Gómez-Martín, 2016) on a cot$\alpha = 1.5$ slope.

| Configuration | Slope | Units | $a$ [mm] | $\bar{b}_{\text{slope}}$ [mm] | $\bar{P}$ [%] |
|---|---|---|---|---|---|
| Single layer (A1, A2) | 1:2 | 15/16 alt. | 49.7 | 35.5 | 40.5 |
| Single layer (A3, A4) | 1:3 | 15/16 alt. | 49.7 | 35.1 | 40.0 |
| Double layer (B1) | 1:3 | 16 | 50.0 | 33.5 | 37.4 |
| Manual (crane) | 1:1.5 | n.a. | 51.5 | 39.5 | 40.5 |

Units are placed by hand from the toe upward, row by row, each unit positioned in the valley between two units of the row below. Single-layer units are placed with random rotation around the vertical

axis. Double-layer second-layer units sit in the valleys of the first layer. After placement the porosity is determined from the total unit count over the measured slope area. The Cubipod Manual reports a single-layer trunk porosity of $40\,\%$ to $43\,\%$ with the recommended grid, and a recommended packing density of $p = 41\,\%$ (Medina and Gómez-Martín, 2016). After a first placement at the manufacturer-advised porosity of about $42\,\%$ failed, a denser target of $39\,\%$ to $41\,\%$ was aimed for.

The placement procedure and the resulting armour layer are shown in Figure 3.7. The measurement stick used to enforce the within-row spacing $a$ is visible in the first panel. The orange units are the instrumented Cubipod replacements with embedded rocking sensors (see section 4.2).

**(a)** Placement in progress **(b)** Partial coverage with instrumented units **(c)** Completed slope before testing

**Figure 3.7:** Cubipod armour placement on the model slope. Orange units are the 3D-printed instrumented Cubipod replacements with embedded rocking sensors. The measurement stick used to enforce the within-row spacing $a$ is shown lying on the slope in the first panel.

## 3.8. Sidewall confinement

At the flume walls the units have no neighbours on the wall side, so they interlock less than the inner units. Without support they would fall out first, not because of the waves but because of the missing neighbours. To prevent this, a steel chain was placed against both glass walls, in contact with the wall-side faces of the units from toe to crest (figure 3.8). The chain takes the place of the missing neighbours and gives the edge units a sideways push. The chain used was one that was available in the lab. Its weight per metre was not matched to the actual load a neighbour unit would give, so the support is probably a bit heavier than needed. Units that move behind the chain are still counted as damage. The chain only stops the wall units from being the first to fail. It does not stop damage.

**Figure 3.8:** Steel chain placed against the flume wall, on top of the Cubipod units.

## 3.9. Test matrix

The following terms are used consistently throughout this thesis:

- *Configuration*: a combination of unit type, slope and underlayer thickness (for example A1: single-layer Cubipod, 1:2, $0.5\,D_n$).
- *Repetition* (or run): one complete test of a configuration, built from scratch and labelled R1, R2, and so on (for example A1_R3).
- *Step*: one wave-height level within a repetition. The wave height is raised step by step until failure or flume capacity.

- *Group*: a set of configurations of the same unit type (A: single-layer Cubipod, B: double-layer Cubipod, C: single-layer cube).

All configurations actually performed are summarised in table 3.6. Group A (single-layer Cubipod) forms the core programme with four valid repetitions per configuration. Group B is a double-layer Cubipod test on cot$\alpha = 3$ added at the end of the programme, and group C is a single-layer cube comparison on cot$\alpha = 3$. The full per test log including dates, completed wave steps, and final $N_{od}$ is given in section B.1.

**Table 3.6:** Test matrix as performed. Reps refers to valid repetitions used in the analysis. Runs discarded due to operational issues are listed in the footnote.

| Grp | ID | Slope | Layers | Unit | $t_f/D_n$ | Reps |
|---|---|---|---|---|---|---|
| A | A1 | 1:2 | 1 | Cubipod | 0.5 | 4 valid* |
| | A2 | 1:2 | 1 | Cubipod | 1.0 | 4 valid |
| | A3 | 1:3 | 1 | Cubipod | 0.5 | 4 valid |
| | A4 | 1:3 | 1 | Cubipod | 1.0 | 4 valid |
| B | B1 | 1:3 | 2 | Cubipod | 0.5 | 1 valid |
| C | C1 | 1:3 | 1 | Cube | 1.0 | 3 valid |
| | | | | Valid repetitions used in the analysis | | 20 |
| | | | | Total runs performed | | 24 |

* In addition to the 4 valid A1 repetitions, the A1 configuration was run 4 more times: one run ended in complete armour failure, one in underlayer failure during compaction, and two were preliminary trial sessions (A1_trial_wed, A1_trial_thu). These 4 runs are excluded from the analysis, which is why 24 runs were performed but only 20 are used.

## 3.10. Wave conditions and sequence

All tests use irregular waves with a JONSWAP spectrum ($\gamma = 3.3$) with a fixed spectral steepness $s_{m-1,0} = H_{m0}/L_{m-1,0} = 0.040$, defined on the spectral period $T_{m-1,0}$. No current was applied in the flume. This steepness roughly corresponds to the design wave steepness at IJmuiden. The parallel cube study (Ruijter, 2026) fixed the steepness instead on the peak period, $s_{0p} = 0.040$. Because $T_p \approx 1.1\,T_{m-1,0}$, fixing $s_{m-1,0} = 0.040$ gives a slightly longer peak period and therefore a lower peak-period steepness than $s_{0p} = 0.040$ (about $20\,\%$ lower). The two programmes are therefore comparable but not identical in wave steepness, which is discussed further in section B.5. The period $T_{m-1,0}$ therefore increases with wave height. The realized values average $1.16$ s in the compaction run and $1.90$ s at step 7 (table 3.7). Because $s_{m-1,0}$ is constant, the Iribarren number is also constant: $\xi_{m-1,0} = \tan\alpha/\sqrt{s_{m-1,0}} = 2.50$ (1:2 slope) and $1.67$ (1:3 slope). The realized incident steepness is somewhat below this target (campaign mean $s_{m-1,0} \approx 0.034$), because the incident height at the structure is lower than the machine setting and depth-induced breaking occurs seaward of the structure at the highest steps. The per step breakdown is given in section B.5. The still water depth is $h = 0.60$ m for the $1{:}2$ slope and $h = 0.65$ m for the $1{:}3$ slope (see table 3.3). The wave paddle is operated with active reflection compensation (ARC), which absorbs reflected waves returning from the structure and prevents them from re-reflecting off the paddle. This is essential in the present tests because the impermeable core produces high reflection coefficients ($K_r$), and without ARC the wave field would be contaminated by re-reflections.

Each test step ran for about $1000$ waves, following Ruijter (2026) and the cube stability analysis of Van der Meer (1988). In practice the wavemaker was run for a fixed time per step, chosen so that about $1000$ waves were generated. The realised step durations were $24$ to $35$ minutes, giving roughly $1000$ to $1040$ waves per step. Each repetition starts with a shorter compaction run (about $500$ to $600$ waves) at a target $H_{m0}$ of 8 cm to settle the armour, followed by 7 test steps with the target $H_{m0}$ raised from 10 cm to 22 cm in increments of 2 cm. These are the send-out (machine) values. The corresponding measured incident wave heights, periods and stability numbers per step are listed in table 3.7.

### 3.10.1. Wave field realisations

All tests use a single JONSWAP wave field realisation (seed 1) at every wave-height step. Repetitions within a configuration and tests across configurations therefore experience identical paddle command signals at each step, so differences in measured incident $H_{m0,\text{inc}}$ and in damage between tests reflect structural response and placement variability rather than differences in wave loading. The seed convention is documented in section B.3.

**Table 3.7:** Wave-height test sequence. The send-out columns are the machine (target) values, set at a fixed steepness $s_{m-1,0} = 0.040$. The incident columns are the mean measured values across all valid repetitions per step at the structure toe, and the stability analysis throughout this thesis uses these realized incident values. $N_s = H_{m0,\text{inc}}/(\Delta D_n)$ is listed for both armour types, with the Cubipod constants ($\Delta = 1.30$, $D_n = 3.24$ cm) and the cube constants ($\Delta = 1.24$, $D_n = 3.1$ cm). The target steepness gives $\xi_{m-1,0} = 2.50$ on the 1:2 slope and $1.67$ on the 1:3 slope. Per slope measured values, peak periods, and reflection coefficients are listed in section B.5.

| | $H_{m0}$ [cm] | | $T_{m-1,0}$ [s] | | | |
|---|---|---|---|---|---|---|
| Step | send-out | inc | send-out | inc | $N_s$ Cubipod | $N_s$ cube |
| 0 (comp.) | 8.0 | 7.2 | 1.13 | 1.16 | 1.71 | 1.87 |
| 1 | 10.0 | 9.1 | 1.27 | 1.30 | 2.16 | 2.37 |
| 2 | 12.0 | 11.0 | 1.39 | 1.42 | 2.61 | 2.86 |
| 3 | 14.0 | 12.9 | 1.50 | 1.52 | 3.06 | 3.36 |
| 4 | 16.0 | 14.7 | 1.60 | 1.63 | 3.49 | 3.82 |
| 5[a] | 18.0 | 17.1 | 1.70 | 1.73 | 4.06 | 4.45 |
| 6[a] | 20.0 | 18.9 | 1.79 | 1.82 | 4.49 | 4.92 |
| 7[a] | 22.0 | 19.5 | 1.88 | 1.90 | 4.63 | 5.07 |

[a] Steps 5–7 were reached only in the double-layer test B1 ($\cot\alpha = 3$). By those steps the top layer of the two layers had already failed, and testing continued only to observe when the remaining bottom layer would fail. The listed realized values are from that test. Cubes (C1, $\cot\alpha = 3$) reached step 2 before failure, so the cube $N_s$ at higher steps is the nominal programme value rather than a tested condition.

A repetition is stopped when failure occurs or the flume capacity is reached.

## 3.11. Data analysis

### 3.11.1. Stability analysis

After each wave-height step, the number of extracted Cubipod units is counted by eye, through direct inspection of the armour layer in the flume. Photographs are taken at each step from a fixed camera position for documentation and later verification. A unit is counted as damage only when it is extracted from the armour layer, that is, lifted or rolled out of its place so that it no longer forms part of the layer. Units that settle or shift along the slope while remaining in the layer are not counted. The damage number is computed as:

$$N_{od} = \frac{N_{\text{ext}}}{B/D_n} \tag{3.2}$$

where $B = 0.79$ m is the flume width, giving $B/D_n \approx 23.5$. The minimum detectable damage corresponds to one extracted unit: $N_{od,min} \approx 0.04$. For each configuration, damage curves ($N_{od}$ versus $N_s$) are plotted and the stability numbers at IDa and IDe are determined. The results are compared against the pre-test prediction (section B.2) and the existing data for $1{:}1.5$ slopes (Medina and Gómez-Martín, 2016).

### 3.11.2. Rocking analysis

The angular velocity signals from the embedded rocking sensors are processed to identify individual rocking events. For each instrumented unit the rocking intensity, quantified by the number of rocking events (and the event rate per 1000 waves) and by the peak angular velocity $|\omega|_{\text{max}}$ per event, is expressed as a function of $N_s$ for each test configuration. This provides an objective measure of incipient instability that is more sensitive than displacement-based damage numbers. The sensor hardware and measurement procedure are described in chapter 4.

# 4

# Instruments and measurements

This chapter describes the instruments used during the physical model tests. An overview is given in table 4.1. Specifications are listed in table 4.2.

**Table 4.1:** Overview of instruments and measurements.

| Instrument | Qty | Purpose | Location |
|---|---|---|---|
| Resistance-type wave gauge (GHM) | 3 | Measure free-surface elevation, derive incident wave height via reflection analysis | Flume, seaward of structure |
| Rocking sensor (TinyZero + IMU) | 5 | Record rocking motion of individual Cubipod units | Embedded in selected Cubipods around SWL |
| HD camera (GoPro Hero 7 Black) | 1 | Record armour displacement for $N_{od}$ documentation | Above the flume, fixed top-view position |

**Table 4.2:** Instrument specifications.

| Instrument | Range | Resolution | Sample rate |
|---|---|---|---|
| Wave gauge (GHM) | 0–0.85 m water column | $\sim$0.1 mm (12-bit ADC) | 100 Hz |
| Rocking sensor (gyroscope) | $\pm$2000 °/s | 0.06 °/s (16-bit) | 100 Hz |
| Rocking sensor (accelerometer) | $\pm$16 g | 1 mg (14-bit) | 100 Hz |
| GoPro Hero 7 Black | 4K / 1080p | – | 30–60 fps |

The three measurement systems run independently and did not interfere with one another: the wave gauges feed the central DASYLab acquisition system, each rocking sensor logs to its own microSD card, and the camera records separately. Figure 4.1 shows the overall flume layout with the wave gauges, the model structure, and the top-view camera.

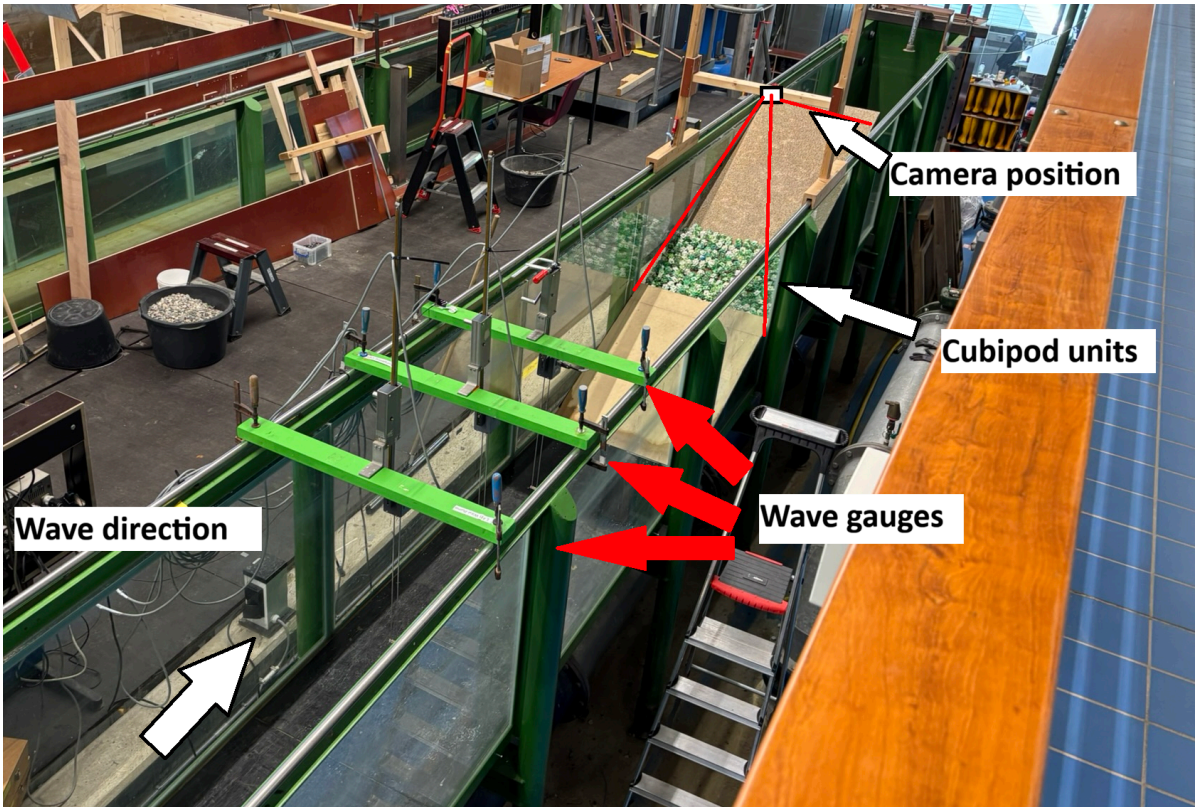


**Figure 4.1:** Annotated overview of the TU Delft 2D wave flume showing the wave-gauge array seaward of the structure, the model breakwater (right), and the position of the top-view camera.

## 4.1. Wave height measurement

Three resistance-type wave gauges are positioned seaward of the structure in a linear array (figure 4.2). The gauges are sampled at 100 Hz using a DASYLab V13 data acquisition system. Each gauge was calibrated against still-water depth at the start of the campaign and re-calibrated once on 02-04-2026 after a wiring change that swapped two DASYLab channels. All three gauges give a linear-fit scale factor within $0.5\,\%$ of each other at $R^2 > 0.9999$. The calibration procedure, calibration lines, and fit parameters are reported in section B.4.

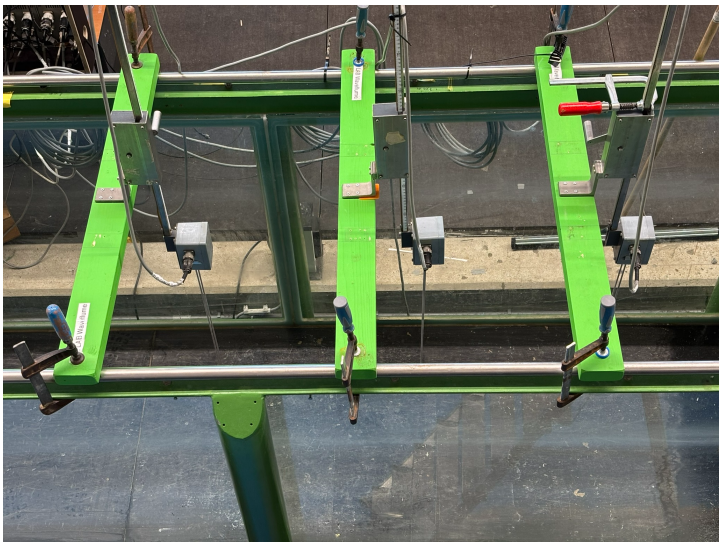

**Figure 4.2:** The three resistance-type wave gauges in the flume, mounted seaward of the structure.

### 4.1.1. Wave gauge spacing

The spacing was fixed a priori using the condition number optimisation of Wenneker and Hofland (2014) (method MF(3a)). The condition number $C$ measures how strongly small gauge errors are amplified when the incident and reflected waves are separated. A lower $C$ means a more robust separation, and Wenneker and Hofland (2014) require $C < 6$. Because the wave period varies across steps, $C$ is evaluated at the shortest design period (the compaction step), which gives the shortest wavelength and is therefore the most demanding condition for wave separation. Table 4.3 shows $C$ for three candidate spacings at the still-water depth. At longer periods (larger $L$) $C$ is lower and the spacing performs better still.

**Table 4.3:** Condition number $C$ for three gauge spacing options at the $1{:}2$ still-water depth $h = 0.60$ m, evaluated at the shortest design period $T_{m-1,0} = 1.27$ s (compaction step, $s_{m-1,0} = 0.040$). At the deeper $1{:}3$ depth ($h = 0.65$ m) the condition number is marginally higher but stays well below the limit. Gauges numbered 1–3 from offshore. All three satisfy $C < 6$. The selected spacing is $x_{12} = 60$ cm, $x_{23} = 50$ cm.

| $x_{12}$ / $x_{23}$ [cm] | $C$ at $h = 0.60$ m |
|---|---|
| 40 / 30 | 2.02 |
| 50 / 40 | 1.52 |
| 60 / 50 | 1.20 |

All three options satisfy $C \ll 6$. The 60/50 spacing has the lowest $C$ and is therefore selected: $x_{12} = 0.60$ m, $x_{23} = 0.50$ m (gauges numbered 1–3 from offshore). The innermost gauge (gauge 3) is placed 1.5 m seaward of the structure toe. At the dominant test period $T_{m-1,0} \approx 1.8$ s this corresponds to $\approx 0.4\,L$ ($L \approx 3.83$ m at $h = 0.60$ m), within the recommended range of $0.3$–$0.5\,L$ offshore from the slope (Wenneker and Hofland, 2014). The three gauges are thus located at 2.6 m, 2.0 m, and 1.5 m from the toe.

### 4.1.2. Incident wave analysis

The three-gauge array enables separation of incident and reflected waves using the method of (Mansard and Funke, 1980) (referred to as “Decomp15” in the Waterlab). From the incident wave signal, spectral parameters $H_{m0}$, $T_{m-1,0}$, and $T_p$ are obtained via spectral analysis. Zero-crossing analysis provides $H_{1/3}$, $H_{max}$, and wave-by-wave statistics. The reflection coefficient $K_r$ is determined per test, allowing verification of the transfer from generator command to incident wave height at the structure toe.

The gauge positions relative to the wave board are shown in the cross-section drawing of figure A.1.

## 4.2. Rocking measurement

Rocking of individual armour units is measured with small sensors embedded in selected Cubipods, following (Hofland et al., 2023). The essentials are listed below. Full construction, mass and moment-of-inertia calibration, per unit specifications, time synchronisation and firmware are documented in chapter C and section C.3.

- *Sensor unit.* A 3D-printed resin shell houses a TinyCircuits stack (SAMD21 microcontroller, 9-axis IMU, microSD card) and a LiPo battery. The IMU logs angular velocity and acceleration in three axes at 100 Hz to the card, so no cables interfere with movement. Lead ballast matches the moment of inertia of a concrete Cubipod, keeping the dynamic response representative.
- *Layout.* Five instrumented units sit in one horizontal row around still water level, where rocking is strongest. Some early tests used fewer. The per test count is reported in chapter C.
- *Pre-test check.* Each sensor is activated, time-stamped, and checked at rest: the rotation rate $|\omega|$ sits at its at-rest level ($\lesssim 2$ °/s) and the total acceleration $|a|$ within about $\pm 3\,\%$ of $1\,g$, both below the firmware event thresholds ($|\omega| > 0.05$ rad/s, $|a| > 1.05\,g$).
- *Event definition.* After testing the cards are read out and aligned with the wave-gauge record via the start of waves marker. One event combines the uprush and downrush rotation of a single

wave (section 2.6). Per event the peak angular velocity $|\omega|_{\max}$ and rotation amplitude $\Delta\theta$ are extracted.

- *Reported intensity.* Per step: the event rate per $1000$ waves, and the upper-tail statistics $|\omega|_{5\%}$, $|\omega|_{1\%}$ and $|\omega|_{\max}$ of the per event peak angular velocities.
- *Accuracy.* The gyroscope resolves $0.06\,°$/s with a noise floor of about $0.14\,°$/s root mean square (RMS) at 100 Hz, far below the rocking velocities of interest ($10$ to $100\,°$/s). Each sensor logs to its own card, so there is no electrical crosstalk between units.
- *Timing.* The on-board crystal drifts $200$ to $1190$ ppm relative to the DASYLab clock[1]. This is removed in post-processing by an affine fit between switch-plus-shake anchors at the start and end of each session, keeping the wave-to-rocking alignment within one wave period (section C.4). The firmware buffers samples in RAM and writes the card in batches during quiet periods, so the 100 Hz cadence holds even while the card is busy. No firmware-side data loss occurred in the campaign (section C.3).

## 4.3. Damage assessment

Armour damage is quantified using the dimensionless damage number $N_{od}$. The Cubipod Manual quantifies armour damage using $D_e$, the equivalent dimensionless damage based on the Virtual Net method (Medina and Gómez-Martín, 2016). The present study uses $N_{od}$ instead, for two reasons: (1) $N_{od}$ is assessed by direct visual counting in the flume, which is practical and reproducible in the present setup, and (2) it allows direct comparison with earlier TU Delft experiments on the same flume, including cube armour tests (Ruijter, 2026). The damage levels are defined as in section 3.3: IDa at the first extracted unit ($N_{od} \approx 0.04$ for $B/D_n \approx 23.5$), and IDe at $N_{od} = 0.2$ for single-layer armour or $N_{od} = 2.0$ for double-layer armour. The assessment procedure is:

1. Before the first test of a series, a reference photograph of the armour slope is taken from a fixed top-view camera position above the flume.
2. After every wave-height step, the slope is photographed again. These photographs are kept for documentation and later verification.
3. Extracted units, that is units removed from the armour layer, are counted by eye in the flume after each step. The top-view photographs are used afterwards to verify and correct the counts.
4. $N_{od}$ is computed as $N_{od} = N_{\text{ext}}/(B/D_n)$, where $B = 0.79$ m.

The GoPro Hero 7 Black camera is mounted on a wooden frame above the flume, giving a top view of the armour slope. The minimum detectable damage corresponds to one extracted unit: $N_{od} = 1/(B/D_n) = 1/23.5 \approx 0.04$.

### 4.3.1. Photogrammetric reconstruction (B1)

For the double-layer test B1_R1, a photogrammetric reconstruction of the armour slope was performed in addition to the standard top-view photographs. The method was used only for this single test and is described in full in chapter F. The resulting displacement maps are presented in section 5.2.6.

## 4.4. Run-up and overtopping

Run-up and overtopping are not measured in this study. The initial design used a freeboard large enough to prevent overtopping under all test conditions, but this would have required many more armour rows on the gentler 1:3 slope (section 3.6). The freeboard was therefore reduced so that the row count remained comparable to the 1:2 setup, at the cost of accepting some overtopping under the largest waves. Average waves stay below the crest. Only the exceptional waves in the tail of the spectrum reach it. Overtopping events were noted in the logbook during testing.

[1] Crystal drift is the slow deviation of the sensor's quartz-clock rate from true time. A drift of one part per million (ppm) is about one millisecond per $1000$ s. The DASYLab clock is the time base of the wave-gauge acquisition system (section 4.1). The per sensor drift values and the correction method are given in section C.4.

# 5

# Results

This chapter reports the experimental results. It covers the qualitative observations, the hydraulic stability, the failure mechanisms and the reflection coefficients. The measured stability is then turned into design values in section 5.5, the closing section. The interpretation follows in chapter 6.

## 5.1. General observations

Figure 5.1 illustrates the visual progression of a representative test (A4_R2) from initial placement to IDe. The panels track the armour around the still water level after each wave-height step, capturing early compaction and subsequent damage onset.

### 5.1.1. Compaction and settlement behaviour

Settlement appeared in two phases, during the initial compaction run and during the subsequent wave-height steps. The qualitative observations from the test logbook are compiled per configuration in table 5.1. Every Cubipod configuration exhibited armour compaction, but the rate varied with the slope angle and the layer count.

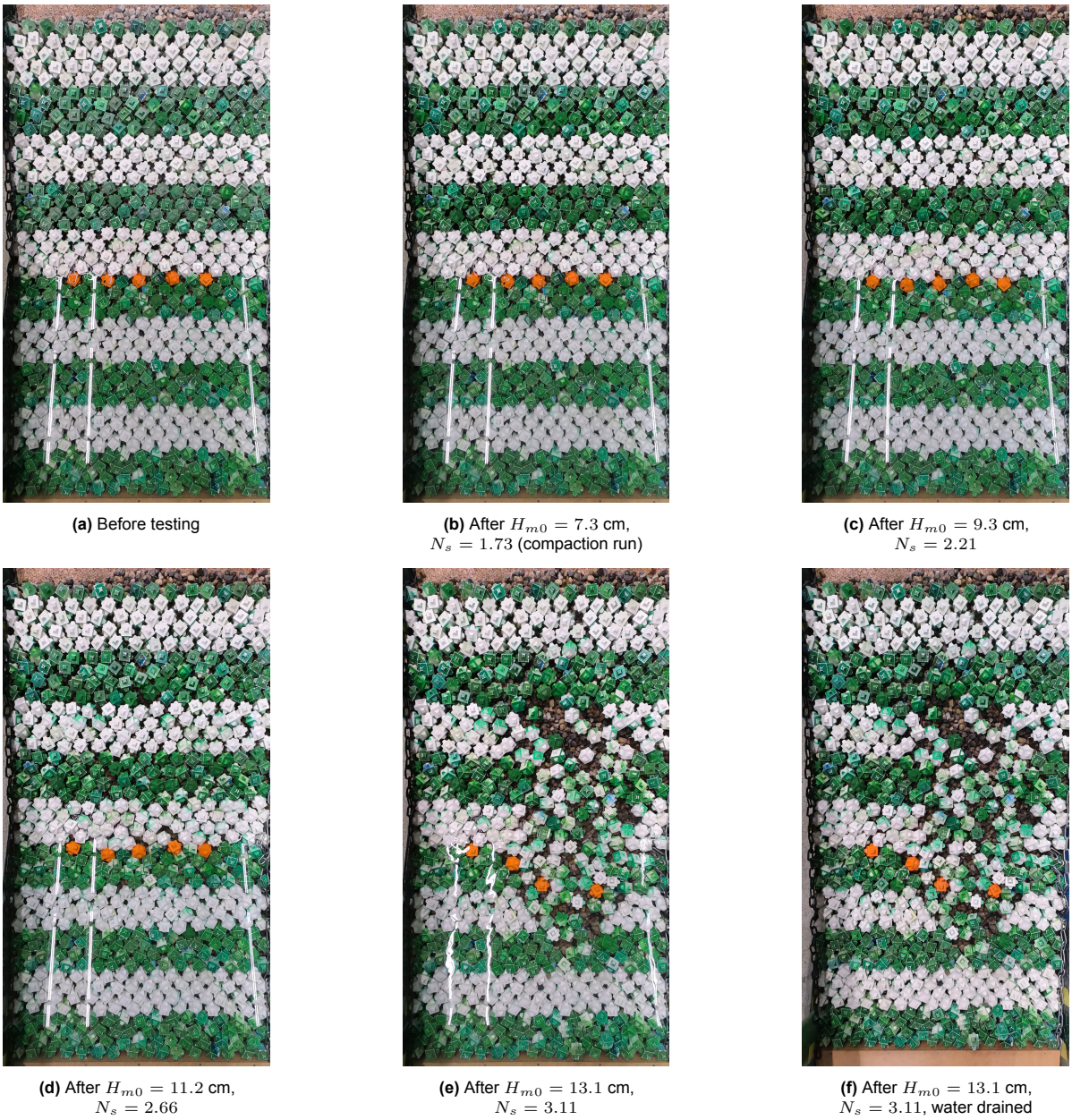

**(a)** Before testing

**(b)** After $H_{m0} = 7.3$ cm, $N_s = 1.73$ (compaction run)

**(c)** After $H_{m0} = 9.3$ cm, $N_s = 2.21$

**(d)** After $H_{m0} = 11.2$ cm, $N_s = 2.66$

**(e)** After $H_{m0} = 13.1$ cm, $N_s = 3.11$

**(f)** After $H_{m0} = 13.1$ cm, $N_s = 3.11$, water drained

**Figure 5.1:** Top-view photographic progression of test A4_R2 (Cubipod, $\cot\alpha = 3$, $t_f = 1.0\,D_n$). Photos taken at still water level after each step. The final panel was taken with the flume drained. Wave heights are the measured incident $H_{m0}$. The sequence runs from initial placement to rapid failure at $H_{m0} = 13.1$ cm.

**Table 5.1:** Qualitative compaction observations per configuration. The compaction-step column records behaviour during step 0 ($H_{m0,\text{target}} = 8$ cm). The middle column records progression during the later wave-height steps. The final column reports the crest behaviour.

| Configuration | Reps | Compaction during step 0 | Progression on later steps | Top-row gap |
|---|---|---|---|---|
| Cubipod, 1:2, single (A1, A2) | 8 | • Top layer moved visibly on every run.<br>• Whole areas compacted at once and shifted downslope, while units beyond the run-up limit stayed put, opening gaps just above it.<br>• The $0.5\,D_n$ underlayer compacted and slid, the $1.0\,D_n$ underlayer did not, so compaction was faster and more complete on $0.5\,D_n$. | • The compaction zone moved upslope as run-up increased, compacting the newly reached zone but less than around still water level.<br>• The armour reached a fully compacted state. | Persistent, below $1\,D_n$ in early A1 reps |
| Cubipod, 1:3, single (A3, A4) | 8 | • Downslope shift visible but less pronounced than on 1:2, and slightly thickness-dependent.<br>• On the $1.0\,D_n$ underlayer some units rocked loosely at step 0 rather than settling collectively. | • Continued slowly but never reached a fully compacted state.<br>• Gaps remained between units until failure. | Minor |
| Cubipod, 1:3, double (B1) | 1 | • Top layer settled slightly.<br>• Bottom layer did not move measurably. | Bottom-layer compaction visible from step 3 onwards, more pronounced from step 5. | None |
| Cube, 1:3, single (C1) | 3 | No settling observed. | No settling observed prior to rapid failure. | None |

The observations in table 5.1 reveal three patterns in how the armour packs together.

First, the slope sets the compaction rate. The single-layer Cubipod slopes settled during the compaction run, but less on the 1:3 slope than on the 1:2 slope. This follows the slope-angle reasoning of section 2.4.1: the along-slope gravity component $W_{\parallel} = W \sin\alpha$ is about $30\,\%$ smaller on $\cot\alpha = 3$ ($\sin\alpha = 0.316$) than on $\cot\alpha = 2$ ($\sin\alpha = 0.447$), so the waves push the units together more slowly on the gentler slope. Compaction on the 1:3 slope is slower rather than absent, and a longer compaction run might have reached the same end state.

Second, the geometry changes differently above and below still water level during the later wave-height steps. Below the water line the waves pushed the units together and tightened the packing. In the most tightly placed repetition (A3_R4, $n_v = 0.386$) the rocking below the water line was visibly reduced just before IDe, showing that the units interlocked more as they compacted. Above the water line the run-up tilted units that the down-flow did not reseat, so the gaps there widened over the steps and a band of wider spacing moved up the slope.

Third, the layer count and the unit type set the settlement capacity. The clearest bulk compaction occurred in the double-layer test (B1), although it developed more slowly than in any single-layer Cubipod on the same slope because the top layer absorbed most of the wave loading. There the bottom-layer porosity dropped from about $40\,\%$ as placed to $37\,\%$ after the test, and the slope length contracted from $143$ cm as placed, to $137.5$ cm before the final step, to $136$ cm after it. No single-layer 1:3 repetition showed a comparable bulk reduction. The cube series (C1), by contrast, did not compact at all before failure, because the regular face-to-face placement left no room to settle. Randomly placed cubes might still have compacted, so it is the regular placement, not the slope, that prevented compaction here. The interpretation of the settlement behaviour is developed in section 6.2.

## 5.2. Hydraulic stability analysis

This section presents the measured stability of the Cubipod configurations as $N_s$ at the two damage thresholds (IDa, IDe) and as $N_{od}$–$N_s$ damage curves. It works through the damage curves per slope, underlayer thickness and unit type. The per slope summary and the derived design values $N_{sd}$ are collected in table 5.2, in the closing section section 5.5. The full individual damage curves are reported in chapter G.

The two damage thresholds used here are defined in section 3.3: IDa, the first extracted unit ($N_{od} \approx 0.04$ for the present model width), and IDe at $N_{od} = 0.2$ for single-layer and $N_{od} = 2.0$ for the double-layer armour as a whole, counting extractions from both layers. Stability is reported through the stability number $N_s = H_{m0}/(\Delta\, D_n)$. The design value $N_{sd}$ follows from the safety-factor method in section 5.5.

On the 1:2 slope the measured IDe lies at $N_s \approx 3.2$ to $3.35$ across the repetitions, with a pooled mean of $3.21$ over the two underlayer thicknesses. The IDa values lie typically $0.4$ to $0.5$ in $N_s$ below IDe. This is the lab baseline against which the 1:3 measurements are compared. The per repetition results and the reasons individual runs were stopped are given in chapter G.

The measured 1:2 IDe ($N_s \approx 3.2$) lies above the Cubipod Manual permeable design value of $2.62$ but below the Manual INHA single-layer lab IDe mean of $4.00$ (open diamonds in figure 5.12). The Manual design value $2.62$ is itself a safety-factor reduction of the Manual permeable lab data (Medina et al., 2012), so it cannot be compared directly to a lab mean of the present study. The design versus design comparison is developed in section 6.1.5.

### 5.2.1. Slope angle

This subsection compares the 1:2 and 1:3 slopes and addresses sub-question 1. Figure 5.2 overlays the individual $N_{od}$–$N_s$ curves from the 1:2 slope (blue) and the 1:3 slope (orange), separated by underlayer thickness.

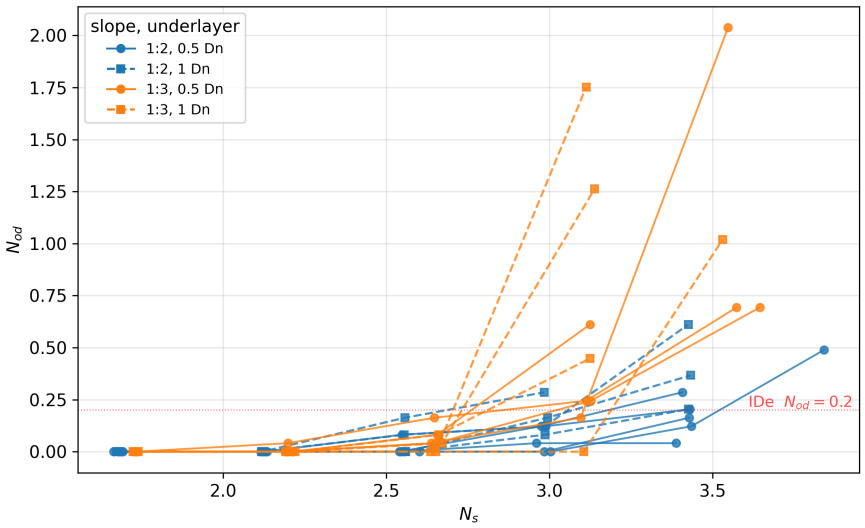


**Figure 5.2:** $N_{od}$ as a function of $N_s$ for all Cubipod tests, grouped by slope and underlayer thickness. Blue: 1:2 slope. Orange: 1:3 slope. Circles with solid line: $t_f = 0.5\, D_n$. Squares with dashed line: $t_f = 1.0\, D_n$. Each line represents one test repetition.

Although the two slopes reach IDe at comparable stability numbers, the damage number on the 1:3 slope rises much more sharply once the first units are extracted. The orange ($\cot\alpha = 3$) and blue ($\cot\alpha = 2$) curves overlap within a single narrow $N_s$ band across both underlayer thicknesses, and in several repetitions the 1:3 slope reaches IDe at the same $N_s$ as the 1:2 slope or slightly below it. In pooled mean IDe values the 1:3 slope gives $N_s = 3.00$ (A3 and A4 combined) against $N_s = 3.21$ on the 1:2 slope (A1 and A2 combined), about $6\,\%$ lower in $N_s$. The gentler slope is therefore not more stable, and if anything it is marginally less stable. The cube tests on the same 1:3 slope and underlayer (series C1) show the same direction, so the effect is not specific to Cubipods.

On the 1:3 slope the armour also failed earlier and faster, with consistently higher final $N_{od}$ values and more units rocking simultaneously in the step before IDe. These observations are described in section 5.3 and interpreted in chapter 6.

### 5.2.2. Underlayer thickness

This subsection addresses the underlayer-thickness part of sub-question 3. The effect of underlayer thickness ($t_f = 0.5\,D_n$ versus $t_f = 1.0\,D_n$) is shown per slope in figure 5.3: the $1{:}2$ slope on the left panel (a) and the $1{:}3$ slope on the right panel (b). Each line represents one test repetition. All as-built porosities are shown, and the placement porosity effect is treated separately in section 5.2.3.

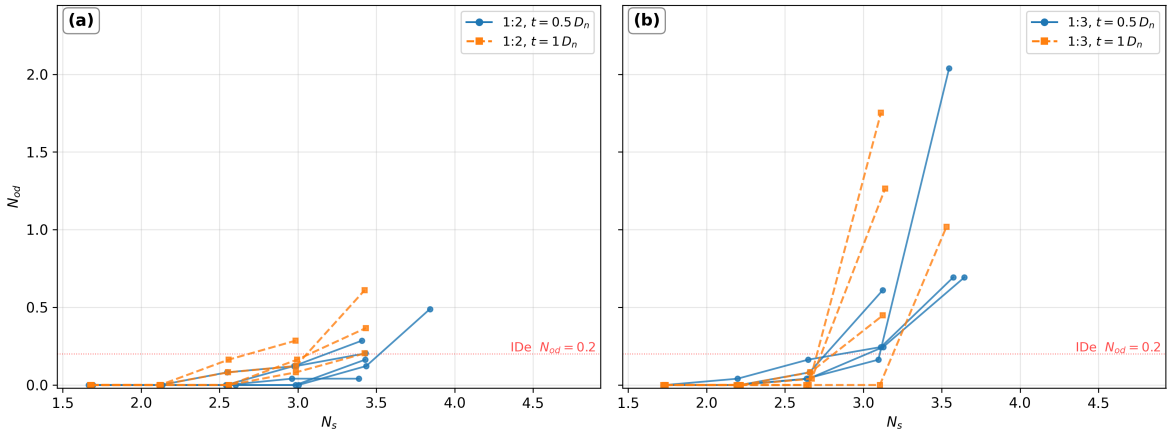


**Figure 5.3:** Underlayer thickness comparison on the Cubipod slopes. (a) $\cot\alpha = 2$ (A1 with $t_f = 0.5\,D_n$, A2 with $t_f = 1.0\,D_n$). (b) $\cot\alpha = 3$ (A3 with $t_f = 0.5\,D_n$, A4 with $t_f = 1.0\,D_n$). Each line is one test repetition. Blue solid lines with circles: $t_f = 0.5\,D_n$. Orange dashed lines with squares: $t_f = 1.0\,D_n$. Porosity range across all repetitions: $38.6$–$42.9\,\%$.

On the $1{:}2$ slope (panel (a) of figure 5.3) the $0.5\,D_n$ underlayer (A1, blue) gives a higher mean IDe ($N_s = 3.35$, $n = 3$ IDe-reaching repetitions) than the $1.0\,D_n$ underlayer (A2, orange, $N_s = 3.10$, $n = 4$), the A2 value being pulled down because one A2 repetition reached IDe at a markedly lower $N_s$ (per configuration means in table G.1). The damage curves of the two series overlap at low $N_s$ and separate only close to IDe. No systematic stability advantage of the thicker filter is apparent.

On the $1{:}3$ slope (panel (b) of figure 5.3) the two thicknesses give the same mean IDe ($N_s = 3.00$ for both A3 and A4), and the damage curves overlap across the full $N_s$ range. The underlayer thickness therefore has no clear effect on stability on this slope. The two series differ only in how IDe develops once it is reached, which is described in section 5.3.

The as-placed porosity also varied across these repetitions ($38.6$ to $42.9\,\%$) and partly overlaps with the thickness comparison. This placement porosity effect is treated separately in section 5.2.3.

### 5.2.3. Placement porosity

The placement-porosity effect identified in the underlayer-thickness comparison is shown directly in figure 5.4, which plots $N_s$ at IDe against the as-placed porosity $n_v = 1 - D_n^2/(a\,b_{\text{slope}})$ derived from the measured centre-to-centre grid spacings. The A1_R2 manufacturer-grid attempt at $n_v = 0.42$ (red cross) failed during the compaction run with no units extracted and is plotted as a high-porosity early-failure anchor at the compaction-step $N_s$. The B1 bottom layer at $n_v = 0.37$ (open star) is included as a top-protected low-porosity reference and is not directly comparable to the single-layer points. Within the narrow as-built single-layer range ($n_v = 38.6$ to $41.5\,\%$) the relation is slope-dependent: the $\cot\alpha = 2$ regression has a significantly negative slope ($R^2 = 0.97$, $p < 0.01$, $n = 7$), while the $\cot\alpha = 3$ regression is weakly positive and not significant ($R^2 = 0.29$, $p = 0.17$, $n = 8$). The mechanism interpretation, including the role of differential downslope settlement and the distinction between as-placed and load-driven porosity, is given in section 6.2.

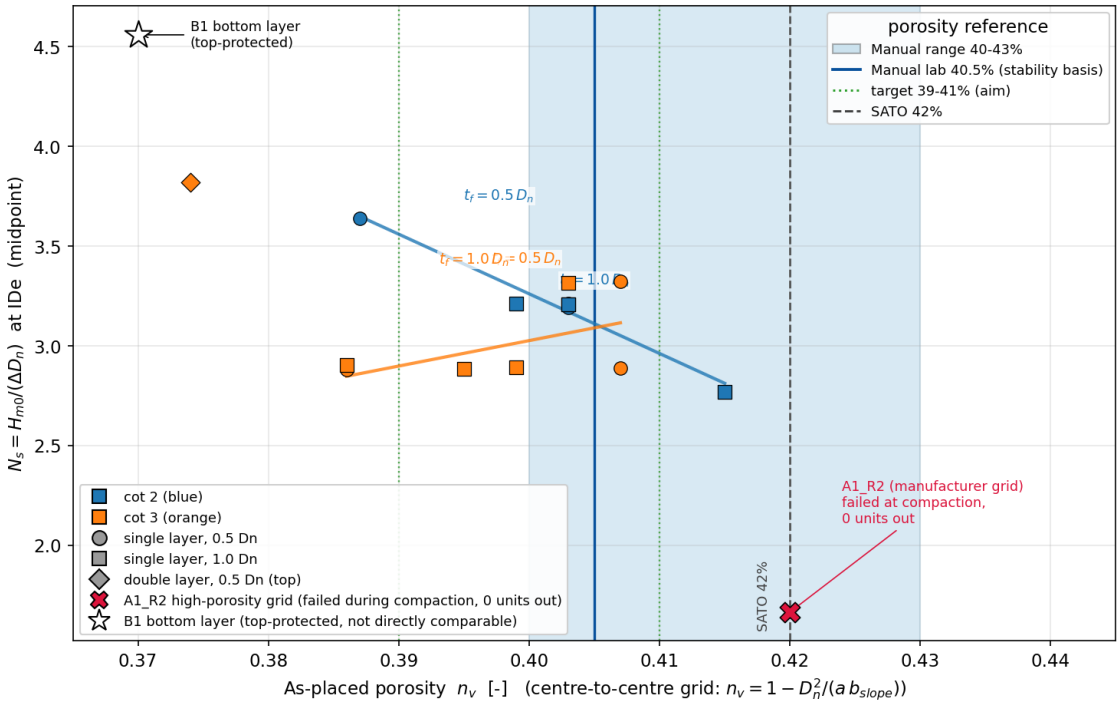


**Figure 5.4:** $N_s$ at IDe against as-placed porosity $n_v = 1 - D_n^2/(a\,b_{\text{slope}})$. Coloured lines: per slope linear regression on the single-layer points (annotated). Two anchors outside the regression: red cross at $n_v = 0.42$ (A1_R2 manufacturer-grid compaction failure, zero extractions). Open star at $n_v = 0.37$ (B1 bottom layer, top-protected). Vertical lines and bands mark the Cubipod Manual lab basis ($40.5\,\%$), the Manual single-layer range ($40$–$43\,\%$), the SATO recommendation ($42\,\%$), and the present aim ($39$–$41\,\%$).

### 5.2.4. Cubipod versus cube

A direct comparison of single-layer Cubipod and single-layer cube armour on an impermeable cross-section isolates the unit-type effect (sub-question 2).

On the 1:2 slope the present Cubipod data (A1 and A2 combined, $n = 9$ IDa, $n = 7$ IDe) are paired with the cube data of (Ruijter, 2026) on the same impermeable cross-section (series S05, S06 and S07, $n = 3$), recomputed at the $N_{od} = 0.2$ single-layer convention used here (table 5.2). The IDe values agree within the test scatter: the Cubipod pooled mean IDe is $N_s = 3.21$ and the cube mean is $N_s \approx 3.1$ (cube constants $\Delta = 1.24$, $D_n = 3.1$ cm). This difference of $0.1$ in $N_s$ is smaller than the test-to-test variation within either unit type, and the IDa values follow the same pattern (Cubipod $N_s \approx 2.6$ to $2.9$, cube $N_s \approx 2.9$). The reduced stability on the impermeable core is therefore shared by both single-layer unit types, not specific to Cubipods.

On the 1:3 slope the cubes (series C1, three repetitions) underwent a rapidly progressive failure within a single step, closely matching the brittle Cubipod behaviour on the same slope. All three repetitions reached IDe at the same wave-height step ($H_{m0,\text{inc}} \approx 11$ cm, step $N_s \approx 2.90$ with cube constants), each removing $28$ to $33$ units at once, with no units extracted at the preceding wave-height step. The cube IDe midpoint ($N_s \approx 2.66$) sits just below the Cubipod value ($N_s = 3.00$). For the cube the IDa and IDe coincided, leaving no reserve between first extraction and destruction. As with the Cubipods, cubes were extracted both during plunging impact and during run-down (two repetitions and one, respectively). Unlike the Cubipods, the regularly placed cubes showed no compaction-run settlement before this abrupt failure (section 5.1.1).

Figure 5.5 compares the two unit types across both slopes, highlighting the absent damage margin for the cube on the gentler slope. The mechanism interpretation and design implications are developed in chapter 6.

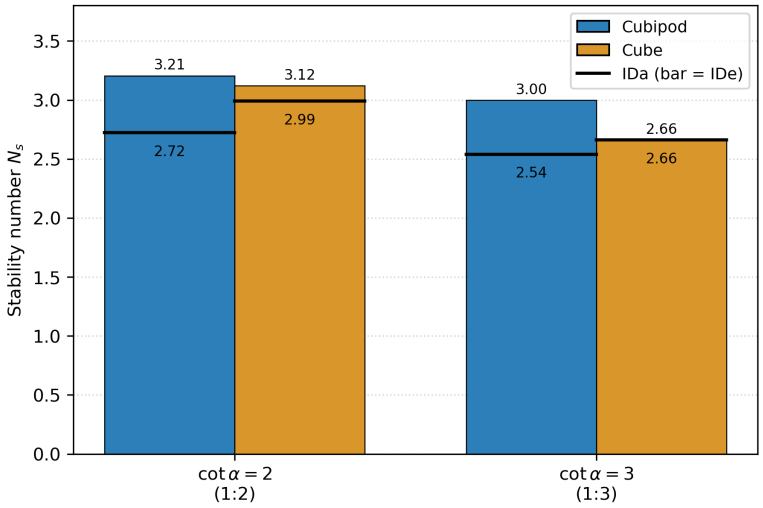


**Figure 5.5:** Single-layer Cubipod versus single-layer cube on the impermeable cross-section, for the 1:2 and 1:3 slopes. Bars: mean $N_s$ at IDe. Black dash: mean $N_s$ at IDa. Cubipod values pool A1+A2 ($\cot\alpha = 2$) and A3+A4 ($\cot\alpha = 3$). Cube values are Ruijter (2026) (S05–S07, $\cot\alpha = 2$) and the present C1 series ($\cot\alpha = 3$). For the cube on the 1:3 slope IDa and IDe coincide.

### 5.2.5. Double-layer configuration

A single double-layer Cubipod test was performed on the 1:3 slope with a $0.5\,D_n$ underlayer (configuration B1, $n = 1$). The armour is built from two stacked Cubipod layers. Throughout this subsection "top layer" means the upper of these two layers, the one exposed to the waves, and "bottom layer" the lower one, the layer resting on the underlayer. Neither term refers to the armour as a whole. The wave-height steps followed the same standard programme as the single-layer tests, from the compaction run to the highest step. A photogrammetric reconstruction of the slope was also made for this test (section 5.2.6).

Damage developed in the top layer first. Counting only the top layer, it reached the single-layer threshold IDe,s ($N_{od} = 0.2$) at a midpoint $N_s \approx 2.89$ ($H_{m0,\text{inc}} \approx 13$ cm). For a double-layer armour the relevant destruction threshold is ten times higher, IDe,d ($N_{od} = 2.0$), because the second layer provides redundancy. The armour reached $N_{od} = 2.0$ through top-layer extractions only, with the bottom layer staying intact. This places the IDe,d midpoint at $N_s \approx 3.82$, well above the single-layer A4 mean of $N_s = 3.00$ on the same slope and underlayer.

By $H_{m0,\text{inc}} = 15.1$ cm ($N_s = 3.58$) the top layer had lost $40$ of its $656$ units ($N_{od,\text{top}} = 1.64$), and many of the remaining top-layer units rocked in place without being removed. Between $H_{m0,\text{inc}} = 15.1$ and $17.1$ cm the toe was repaired by hand: about ten removed units were put back and a steel bar was laid across the toe row, to stop a toe failure from disturbing the rest of the test. This was a manual repair, not self-healing of the armour, and the replaced units are excluded from the later damage counts. After this repair, top-layer removal continued and reached $N_{od,\text{top}} = 20.5$ at $H_{m0,\text{inc}} = 18.9$ cm ($N_s = 4.48$), with heavy overtopping. By then the top-layer units around still water level were already gone, so units sliding down from higher up the slope were removed as soon as they reached the water line. The failure pattern stayed the same throughout, travelling up the slope. Almost the entire top layer had been removed by the final step, $H_{m0,\text{inc}} = 19.5$ cm ($N_s = 4.63$), while the bottom layer was still largely in place.

The double-layer configuration as a whole therefore reached its configuration-appropriate threshold IDe,d ($N_{od} = 2.0$ over both layers) at $N_s \approx 3.82$, an increase of about $0.82$ over the single-layer A4 mean of $3.00$. Failure of the armour as a whole, defined here as loss of the bottom layer after the top layer has been removed, was only approached at the highest tested step ($H_{m0,\text{inc}} = 19.5$ cm, $N_s = 4.63$): at that step 5 bottom-layer units had been removed across the slope width, so the bottom layer reached the single-layer threshold IDe,s ($N_{od} = 0.2$) at a midpoint $N_s \approx 4.56$. This bottom layer was compacted and protected by the top layer throughout build-up, so the $N_s \approx 4.56$ is not a standalone single-layer stability value. Geometric measurement at the end of the test gave a bottom-layer porosity of $37\,\%$,

against the as-placed value of approximately $40\,\%$ used for the single-layer A3 and A4 series. The corresponding slope length contracted from $143$ cm as placed, to $137.5$ cm before the final step, to $136$ cm afterwards, consistent with the porosity reduction.

The result rests on a single repetition. Reproducibility of the bottom-layer behaviour was not assessed within the present programme. The physical interpretation of the top versus bottom layer behaviour is given in section 6.2.

### 5.2.6. Photogrammetric reconstruction (B1)

A photogrammetric reconstruction of the armour slope was carried out for the double-layer test B1_R1 as a three-dimensional damage assessment. The method, pipeline, and alignment quality are described in chapter F.

Two representative displacement maps from the resulting cloud-to-cloud differencing are shown in figure 5.6: the first damage scan at $H_{m0,\text{inc}} = 13.3$ cm and the best aligned scan at $H_{m0,\text{inc}} = 17.1$ cm ($RMS = 1.4$ mm). The full series of six post-step maps is given in figure F.2 of section F.1 and read step by step there, together with the top-view photographic record of the same test.

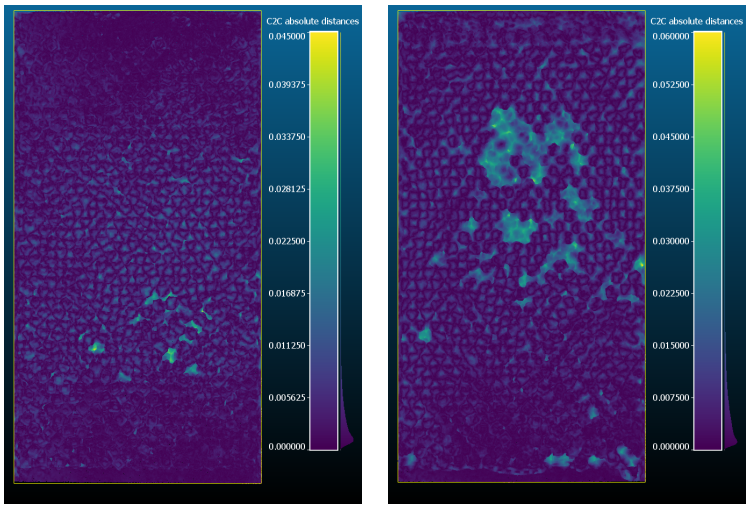


**(a)** $H_{m0,\text{inc}} = 13.3$ cm, $N_s = 3.16$, first localised damage.

**(b)** $H_{m0,\text{inc}} = 17.1$ cm, $N_s = 4.06$, best alignment of the series ($RMS = 1.4$ mm).

**Figure 5.6:** Two representative cloud-to-cloud displacement maps from the B1_R1 photogrammetric reconstruction at incident wave heights $H_{m0,\text{inc}} = 13.3$ and $17.1$ cm. Viridis colour scale, $0$ to $45$ mm. The full set of six post-step maps is shown in figure F.2.

The displacement field develops from a near-uniform low-magnitude pattern at $H_{m0,\text{inc}} = 9.3$ cm (armour-layer compaction rather than damage), through the first localised below-SWL peaks at $H_{m0,\text{inc}} = 13.3$ cm, to a wide high-amplitude band across the mid-slope by $H_{m0,\text{inc}} = 17.1$ cm (best alignment of the series, RMS $1.4$ mm) and near-complete coverage of the armoured face at $H_{m0,\text{inc}} = 18.9$ and $19.5$ cm (read qualitatively only, RMS $\approx 10$ mm). Across the sequence the photogrammetry confirms the photograph-based $N_{od}$ progression and adds the spatial distribution of damage along the slope, which the unit count does not give. It shows the damage developing and moving up the slope, mainly as translation of units rather than rotation, and it also captures movement that does not remove a unit and so contributes zero to the count.

## 5.3. Analysis of failure mechanisms

This section addresses sub-question 4. The failure of the armour followed three stages: units first rock in place, then a wave lifts a unit out of the layer, and the gap then spreads. Units were extracted both during wave run-down and during the run-up and impact of the incoming, plunging wave. Each stage is described below, with the configurations on which it dominated. Settlement is reported in section 5.1.1.

### 5.3.1. Rocking and extraction sequence

At wave-height steps below IDa, individual units around SWL were observed to rotate slightly during run-down and run-up of larger waves, without being extracted. The number of units rocking simultaneously increased with $N_s$ and was systematically larger on the 1:3 slope than on the 1:2 slope at matched $N_s$. Typical visual estimates during the wave-height step preceding IDe on the 1:3 slope ($N_s \approx 2.65$ to $3.12$, incident) reached $5$ to $20$ units simultaneously rocking, against $0$ to $2$ units on the 1:2 slope at the same $N_s$. The rocking signal thus carries an observable pre-IDa precursor of the next damage step.

Rocking and extraction are not the same thing. In test A4_R2 (IDe at $H_{m0,\text{inc}} \approx 13$ cm, midpoint $N_s \approx 2.89$) one unit was seen to rock and then lift out of the slope, while its neighbour kept rocking in the same spot without ever leaving. A unit often rocks for a while, settles back as the surrounding units shift, and only leaves the slope when a wave lifts it clear of its neighbours. Visible rocking therefore did not reliably mean damage. For the sensor record this means the number of rocking events is not a count of extractions. What matters in the signal is how strong the rocking is (the peak angular velocity), not how often it occurs.

On the 1:3 slope the first unit to leave the armour usually sat at a slightly looser spot than its surroundings (locally higher porosity). Once it left, the units below the water line settled a little downslope while the row above stayed in place, so the extracted unit lost the support of the row above and was not replaced. Loose placement spots were therefore the typical starting point of failure, and loss of support by downslope settlement the typical trigger on the 1:3 slope.

### 5.3.2. Adjacent extraction and progressive failure

Once a single unit had been extracted, the two slopes behaved very differently.

On the 1:2 slope the armour healed itself. When a unit was extracted, the units above settled down a little and closed the gap, partly or fully, so the surrounding units stayed interlocked and the layer as a whole stayed stable. Failure therefore spread slowly: one or two neighbouring units left on each side per step and the damage band stayed narrow, about $1$ to $2$ rows around SWL, even at the highest $N_s$ tested. At the end of a 1:2 failure run typically $5$ to $15$ units had been extracted.

On the 1:3 slope there was no such recovery. When a unit was extracted, the units above usually did not settle to fill the gap, so the units around the hole lost their interlock, became unstable and were extracted in turn. This set off a rapidly progressive failure in which the hole grew quickly, removing several tens of units within 200 waves and opening a wide gap of about $5$ to $8$ rows around SWL. The failure run often had to be stopped early to keep the whole armour layer and underlayer from collapsing. The progressive failure shows up as the steep, single-step rise of $N_{od}$ on the 1:3 slope.

The contrast between gradual and rapidly progressive failure is shown in figure 5.7, which plots the mean per step damage increment $\Delta N_{od}$ per slope and underlayer thickness against incident $N_s$: the $\cot\alpha = 3$ curves cross IDe in a single steep step, while the $\cot\alpha = 2$ curves rise gradually over several steps. Beyond IDe the height of the rise depends on when the run was stopped, but its shape is comparable across repetitions.

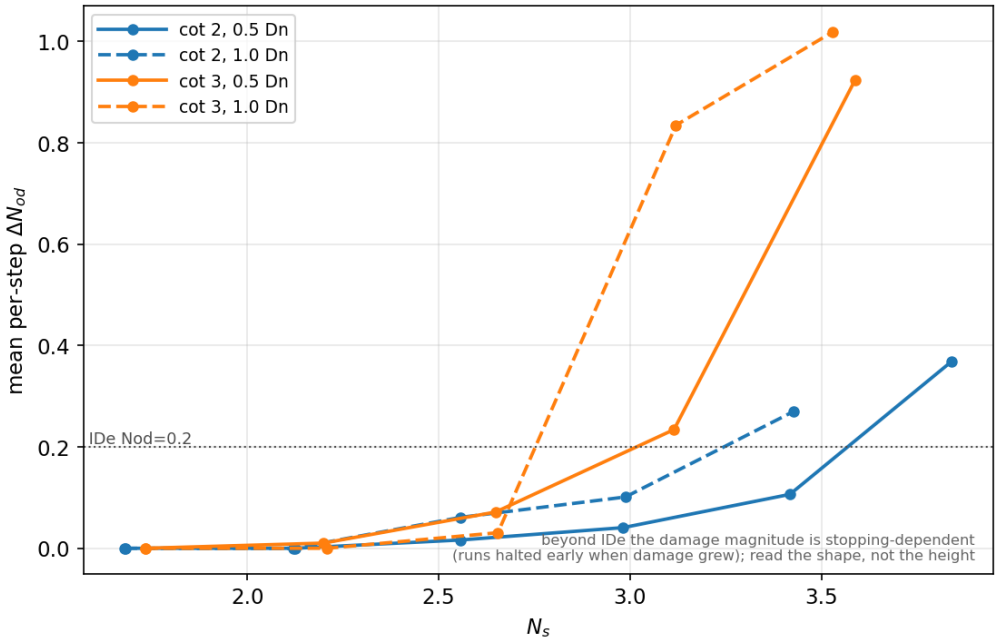


**Figure 5.7:** Mean per step damage increment $\Delta N_{od}$ per slope and underlayer thickness, against incident $N_s$. Dotted horizontal: single-layer IDe threshold $N_{od} = 0.2$. Beyond IDe the absolute height of the rise depends on when each run was stopped. Runs were halted as the extraction rate climbed steeply toward complete armour loss, to keep the layer recoverable and avoid clearing the flume floor.

### 5.3.3. Rocking-sensor results

The five sensors recorded $124\,104$ rocking events across the 13 instrumented runs, after excluding events from the 8 cm compaction step and from moments after a sensor was extracted from the armour. The main result, the rocking intensity per configuration, is presented below. The supporting Xbloc reference comparison, the visual-detection threshold context, the per axis breakdown, and the test-level relation between rocking and damage are in chapter D.

Figure 5.8 shows four rocking metrics per configuration against incoming $N_s$. The clearest contrast is in the intensity metrics, panels (c) and (d): both 1:3 configurations sit far above both 1:2 configurations, with peak angular velocities and rotation amplitudes several times higher at matched $N_s$. The count metrics, panels (a) and (b), are more mixed. The 1:3 $0.5\,D_n$ configuration has the highest event count and rate, but the 1:2 $1.0\,D_n$ configuration also rocks often, above the 1:3 $1.0\,D_n$ configuration on these two panels. The units on the 1:2 slope therefore rock frequently but gently, while the units on the 1:3 slope rock harder. This matches the slope-related stability shortfall in the damage data (section 5.2.1): on the gentler slope the rocking is more violent, which is what the strength of the rocking, rather than its count, captures.

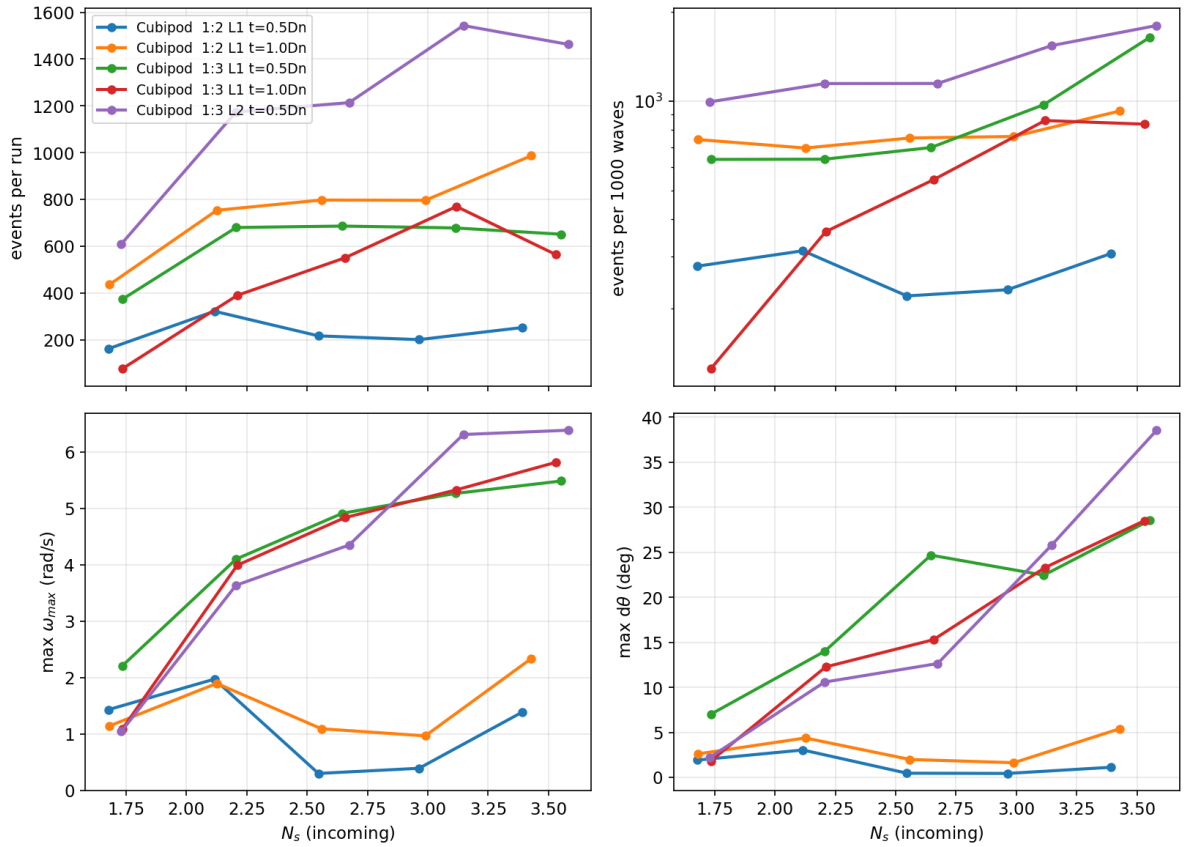


**Figure 5.8:** Per configuration mean of four rocking metrics against incoming $N_s$. Panels: (a) event count per run, (b) event rate per 1000 waves, (c) max peak angular velocity, (d) max rotation amplitude. Panels (a) and (b) differ because the number of waves per run is not constant: each step ran for $1000\,T_p$ (about 1000 to 1040 waves), the compaction run was shorter, and some runs were stopped early at failure, so the rate normalises the raw count by the actual number of waves. The leftmost point of each curve is the 8 cm compaction step.

At the test level, rocking activity tracks measured damage on the 1:3 slope but not on the 1:2 slope, where little damage develops. As in the earlier rocking-sensor work on Xbloc (Hofland et al., 2023), it is a coarse structure-level indicator of armour condition rather than a per unit predictor (figure D.1, section 6.4.2).

## 5.4. Reflection coefficients

Figure 5.9 shows the reflection coefficient $K_r$ measured per wave-height step for each test series, derived from the three-gauge Mansard-Funke separation (chapter 4). The 1:2 Cubipod series (A1, A2) cluster at $K_r \approx 0.30$–$0.45$, while the 1:3 Cubipod series (A3, A4) and the 1:3 cube series (C1) lie distinctly lower at $K_r \approx 0.15$–$0.30$. A dimensionless analysis of these values against the framework of Díaz-Carrasco et al. (2020), including a comparison with the armoured permeable formula of Zanuttigh and Van der Meer (2008) and the cube data of Ruijter (2026), is reported in chapter H.

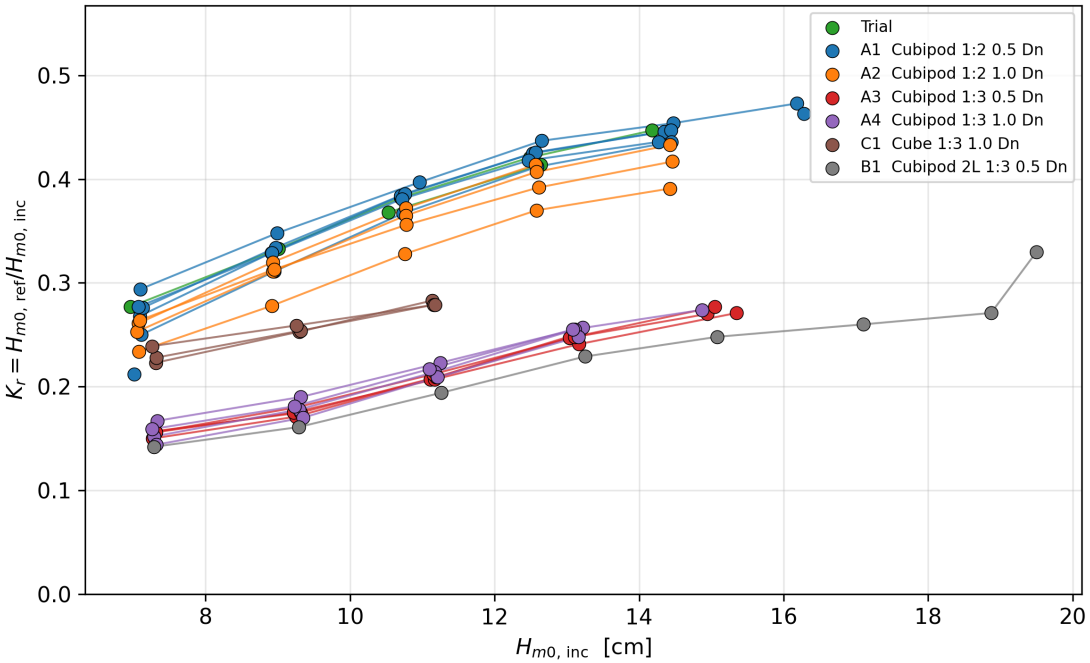


**Figure 5.9:** Reflection coefficient $K_r$ versus incident wave height $H_{m0,\mathrm{inc}}$ for all tests. Colour distinguishes test series (armour unit, slope, and underlayer thickness). Lines connect consecutive wave-height steps within a single test. Open markers denote the initial compaction step.

## 5.5. Safety-factor analysis and design values

The design stability number $N_{sd}$ reported in table 5.2 is derived using the percentile-based safety-factor method of Medina et al. (2012). A safety factor (SF) is applied to bridge the gap between laboratory measurements and a reliable prototype design. The core method is presented below, while supporting tables and a sensitivity analysis are provided in section G.3.

For each test series, the stability number $N_s$ is recorded at both damage thresholds, IDa and IDe (section 3.3). A normal, or Gaussian, distribution is then fitted to these values, described by its mean $\mu$ and standard deviation $\sigma$. The design uses the lower $5\,\%$ value of this distribution, $N_s(5\%) = \mu - 1.645\,\sigma$, which is the value that $95\,\%$ of tests exceed.

Each configuration has only three to five repetitions, too few to estimate the scatter $\sigma$ reliably. A single tightly clustered series could make $\sigma$ look smaller than it is, which would make the characteristic $5\,\%$ value $N_s(5\%)$ too high, as less is then subtracted from the mean. The mean and the scatter are therefore pooled in different ways. The underlayer thickness has no clear effect on the average stability, so the two thicknesses of a slope are combined into one mean per slope. The slope does change the average stability, so the two slopes are kept separate for the mean. The scatter, by contrast, depends on neither thickness nor slope: it comes from the random placement of the units and the random wave order, which is a property of the unit type. The per configuration values in table G.1 support this, showing no clear pattern of $\sigma$ with thickness or slope, only random variation between the small samples. All four single-layer series are therefore pooled into one $\sigma$.

On the 1:2 slope the mean combines A1 ($n = 5$ at IDa, $n = 3$ at IDe) and A2 ($n = 4$, $n = 4$), giving $n = 9$ at IDa and $n = 7$ at IDe. For the standard deviation all four series are pooled ($n = 17$ at IDa, $n = 15$ at IDe). The pooled $\sigma \approx 0.33$ at IDa and $0.22$ at IDe lies within the spread of the individual series ($0.21$ to $0.42$), so pooling does not lower the scatter. What it improves is the reliability of the estimate: the uncertainty of $\sigma$ drops from about $40\,\%$ for a single series of four tests to about $18\,\%$ for the full pool of all four series (section G.3). The scatter itself is small, with a coefficient of variation $\sigma/\mu$ of about $12\,\%$ at IDa and $7\,\%$ at IDe, so the failure point is repeatable. To check whether this amount of scatter is normal, it can be compared with the other single-layer Cubipod dataset. The spread back-calculated

from the safety factors of Medina et al. (2012) is $\sigma \approx 0.33$ at IDa and $0.53$ at IDe, of the same size and, at IDa, almost identical. The present tests therefore scatter by a normal amount for this type of armour, which supports the fitted distributions.

The design stability number $N_{sd}$ is calculated by applying a safety factor to the characteristic $5\,\%$ value of the damage thresholds. Following Medina et al. (2012), the primary design anchor is the destruction threshold IDe, with a required safety factor of $1.31$. However, single-layer interlocking armour fails in a brittle manner. The gap between first damage and full destruction is narrow. The design must therefore also comply with a no-damage requirement. No damage means that the design condition stays at or below the initiation of damage (IDa), defined as the displacement or extraction of the first armour unit. Because a Gaussian distribution never reaches exactly zero, this is a low-probability criterion rather than a strict zero-probability one. Furthermore, a large prototype breakwater contains many more units than a laboratory model, which increases the chance that at least one unit reaches IDa.

To keep a margin against brittle failure, the design is set below IDa following Medina et al. (2012) and the Cubipod Manual (Medina and Gómez-Martín, 2016), using a minimum safety factor on the $5\,\%$ characteristic IDa value. The permeable single-layer Cubipod reference of Medina et al. (2012) uses $\mathrm{SF}(\mathsf{IDa}_{5\%}) = 1.06$. A slightly larger margin of $\mathrm{SF}(\mathsf{IDa}_{5\%}) \geq 1.10$ is applied here, because the present impermeable gentle-slope configuration is more brittle than that permeable reference, so avoiding first damage is given more weight. The final design value $N_{sd}$ is the minimum of these two constraints:

$$N_{sd} = \min\left(\frac{N_s(\mathsf{IDe}_{5\%})}{1.31},\ \frac{N_s(\mathsf{IDa}_{5\%})}{1.10}\right) \tag{5.1}$$

On these slopes the IDa and IDe thresholds lie close together, with a gap of $0.46$ to $0.49$ in $N_s$, about half the $0.97$ of the permeable 1:1.5 reference. Anchoring on IDe alone would therefore give $\mathrm{SF}(\mathsf{IDa}_{5\%}) \leq 1.0$, allowing first damage at the design wave height, so on both slopes it is the safety factor on IDa that sets $N_{sd}$.

A consequence is that the resulting design keeps a comparatively large reserve against full destruction. At the design values the destruction margin is $\mathrm{SF}(\mathsf{IDe}_{5\%}) = 1.43$ on the 1:2 slope and $1.45$ on the 1:3 slope, both clearly above the $1.31$ associated with the permeable single-layer Cubipod by Medina et al. (2012). This difference is intentional and desirable. The narrower the gap between first damage and destruction, the more brittle the response, so the impermeable configuration tested here is deliberately given a larger margin to destruction than the less brittle permeable reference.

Applied to the present impermeable-core measurements, the method gives $N_{sd} = 1.98$ for the 1:2 slope and $N_{sd} = 1.81$ for the 1:3 slope. The percentile schematics are shown for single-layer Cubipod in figure 5.10 and for single-layer cube in figure 5.11. For the cube configurations, the standard deviation pools literature data to improve the estimate due to the sparse sample size. Because cubes fail more abruptly than Cubipods, with the initiation of damage and the initiation of destruction coinciding for the C1 series, a stricter no-damage cap of $\mathrm{SF}(\mathsf{IDa}_{5\%}) = 1.20$ is applied to the cube, against $1.10$ for the Cubipod. This gives cube design values of $N_{sd} = 1.90$ on $\cot\alpha = 2$ and $1.62$ on $\cot\alpha = 3$, which keeps the cube destruction margin comparable to the Cubipod. These values rest on fewer tests than the Cubipod values, with three repetitions on the 1:3 slope and literature data on the 1:2 slope. The prototype-design implications are developed in section 6.1.5.

**Table 5.2:** Summary stability numbers and design values per slope. The $50\,\%$ value is the mean $\mu$ of the per test $N_s$, the $5\,\%$ value is the characteristic $\mu - 1.645\,\sigma$, and $N_{sd}$ is the design value, all derived by the method described above. Per configuration breakdown in tables G.1 and G.2. Cube $N_s$ uses cube constants ($\Delta = 1.24$, $D_n = 3.1$ cm), so comparisons with Cubipod $N_s$ are per damage threshold (lab versus lab).

| | $n$ | | $N_s$ at IDa | | $N_s$ at IDe | | |
|---|---|---|---|---|---|---|---|
| Unit, slope (series) | IDa | IDe | 50% | 5% | 50% | 5% | $N_{sd}$ |
| *Present study* | | | | | | | |
| Cubipod, 1:2 (A1, A2) | 9 | 7 | 2.72 | 2.18 | 3.21 | 2.84 | 1.98 |
| Cubipod, 1:3 (A3, A4) | 8 | 8 | 2.54 | 2.00 | 3.00 | 2.63 | 1.81 |
| Cube, 1:3 (C1) | 3 | 3 | 2.66 | 1.95 | 2.66 | 2.37 | 1.62 |
| Cubipod, 1:3, 2 layers (B1) | — | 1 | — | — | 3.82 | — | — |
| *Ruijter (2026), cubes on $\cot\alpha = 2$ impermeable* | | | | | | | |
| Cube, 1:2 (S05–S07) | 5 | 3 | 2.99 | 2.28 | 3.12 | 2.83 | 1.90 |

A dash means the value is not derived, either because there is only one test ($n = 1$) or, for the double-layer armour, because IDe does not set a design value. For the cube row on $\cot\alpha = 2$ the spread $\sigma$ also uses the additional underlayer thicknesses of (Ruijter, 2026), while the mean uses only the matched $0.5$ and $1.0\,D_n$ data.

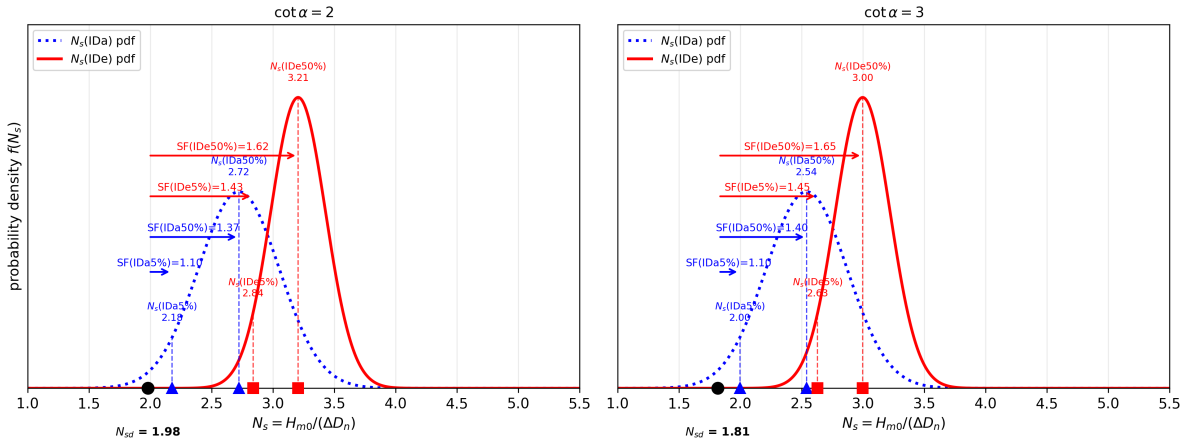


**Figure 5.10:** Percentile-based safety-factor schematic for single-layer Cubipod armour (Medina et al., 2012). Blue triangles mark the IDa characteristic values, red squares the IDe values, with the $5\,\%$ fractile on the left and the $50\,\%$ value on the right of each pair. The black dot is the design value $N_{sd}$ ($1.98$ at $\cot\alpha = 2$, $1.81$ at $\cot\alpha = 3$).

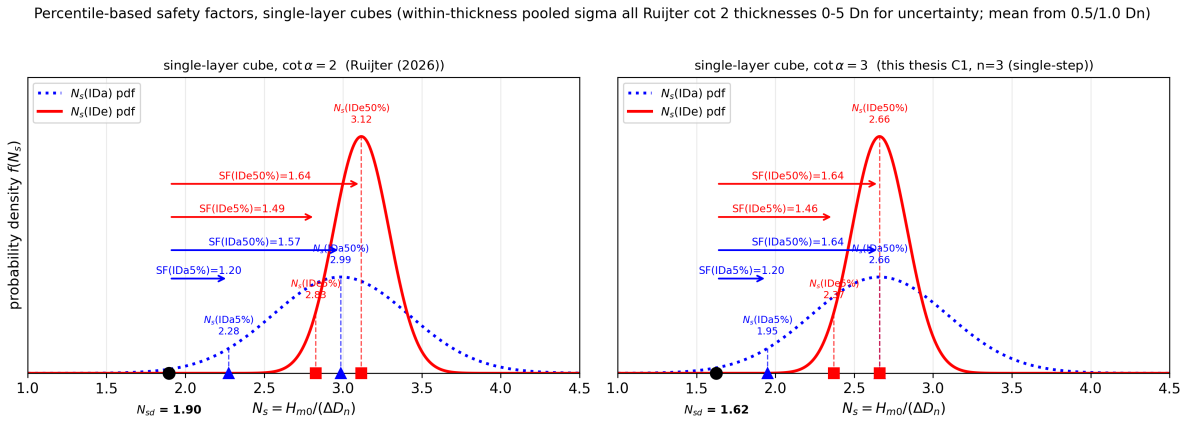


**Figure 5.11:** Percentile-based safety-factor schematic for single-layer cube armour, markers as in figure 5.10. Left: Ruijter (2026) cubes ($\cot\alpha = 2$). Right: present C1 series ($\cot\alpha = 3$, IDa and IDe coincide). Design values $N_{sd} = 1.90$ ($\cot\alpha = 2$) and $1.62$ ($\cot\alpha = 3$), using a stricter cube cap $\mathrm{SF}(\mathrm{IDa}_{5\%}) = 1.20$.

The derived design values are placed next to the Manual references in figure 5.12 (Cubipod) and figure 5.13 (cube), which bring together the measured thresholds, the design values, and the permeable Manual reference at $\cot\alpha = 1.5$.

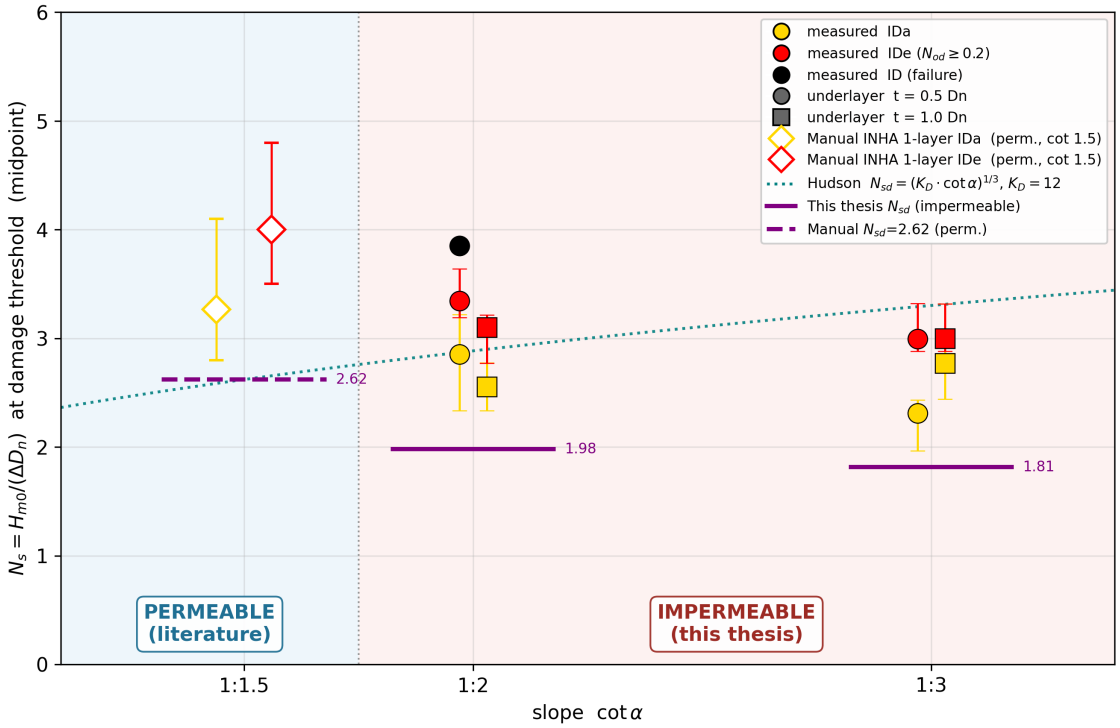


**Figure 5.12:** Measured stability numbers ($N_s$) for single-layer Cubipods at IDa and IDe damage thresholds against slope angle. Vertical bars indicate the full data range (minimum to maximum) across repetitions. Present impermeable-core results ($\cot\alpha = 2, 3$) are compared with permeable reference data at $\cot\alpha = 1.5$ from the Cubipod Manual (Medina et al., 2012). Solid purple lines indicate derived design values ($N_{sd}$), limited by the single-layer no-damage requirement.

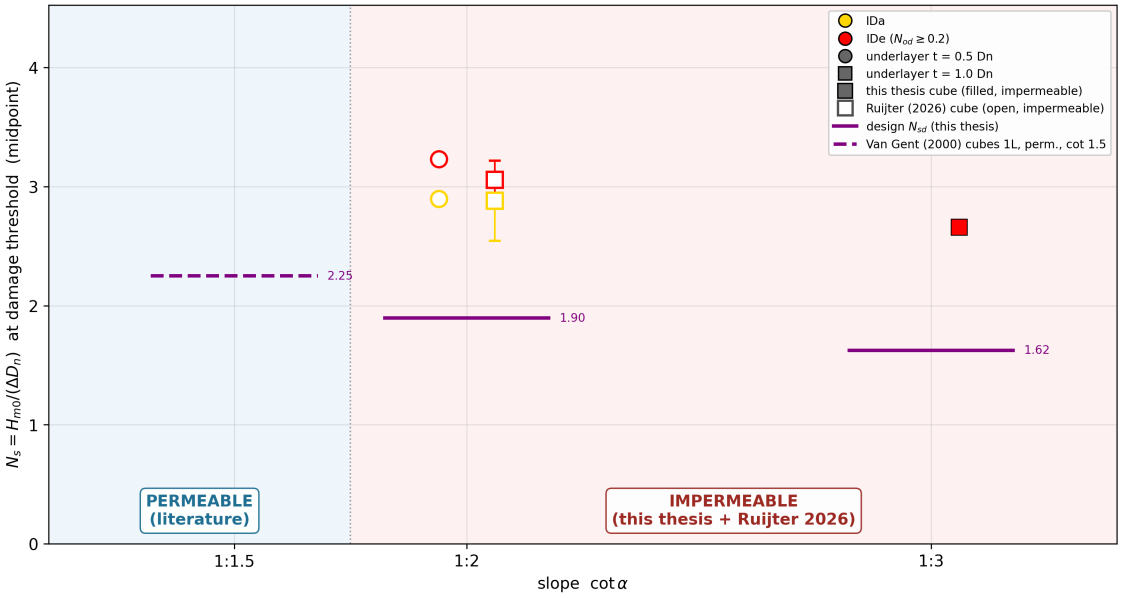


**Figure 5.13:** Single-layer cube stability chart, comparing present results ($\cot\alpha = 3$) with data from Ruijter (2026) ($\cot\alpha = 2$) on impermeable cores, and the permeable reference value ($N_s = 2.25$) from the Rock Manual (Rock Manual, 2007). Solid purple lines indicate derived design values ($N_{sd}$), limited by the single-layer no-damage requirement on both slopes. Layout matches figure 5.12. For C1 the IDa and IDe markers coincide.

# 6

# Discussion

This chapter interprets the experimental results. It compares the measured stability with the literature and the design guidelines. It combines the slope and core effects into one mechanism. It then covers the implications for the IJmuiden prototype, the influence factors, and the model limitations.

## 6.1. Comparison with literature

Table 6.1 compiles the design stability values from the present study with the corresponding design-basis literature values for the same unit type and slope condition. The literature values for rock, cubes, Xbloc and Tetrapod are reproduced from Table 2.3 in chapter 2, where the original sources are cited and the conventions are explained. The permeable Cubipod values are the Cubipod Manual design values ($N_s = 2.62$ for one layer and $3.48$ for two layers). Their derivation is given in the footnotes of Table 2.3. The impermeable-core cells filled by this thesis are reported as design stability numbers $N_{sd}$ derived from the percentile-based safety-factor analysis (table G.2). The matched cube comparison on $\cot\alpha = 2$ uses the same framework applied to the data of Ruijter (2026). Comparing lab ranges with design values would be misleading, so the lab measurements themselves are reported separately in table 5.2.

**Table 6.1:** Design stability values $H_s/D_n$ from literature combined with the present study. Values use $\Delta = 1.4$ for concrete and $\Delta = 1.65$ for rock and are not directly applicable to other densities. The present thesis values use $\Delta = 1.30$ for Cubipods and $\Delta = 1.24$ for cubes. Rows for rock, cubes (permeable), Xbloc and Tetrapod reproduce Table 2.3 of chapter 2. Shaded cells are the impermeable-core configurations tested in this thesis. They are filled here with the design stability number $N_{sd}$ from table G.2, and the matched cube comparison on $\cot\alpha = 2$ uses the same framework applied to the data of Ruijter (2026). Lab values for the present tests are listed separately in table 5.2. Cells marked — indicate no published data and no test in this study.

| Unit type | Core | $\cot\alpha = 1.5$ | $\cot\alpha = 2$ | $\cot\alpha = 3$ |
|---|---|---|---|---|
| Rock | permeable ($P = 0.5$) | 1.44[g] | 1.66[g] | 2.04[g] |
| Rock | impermeable ($P = 0.1$) | 1.08[g] | 1.25[g] | 1.53[g] |
| Cubes (1 layer) | permeable | 2.2–2.3 | 2.2–2.3 | — |
| Cubes (1 layer) | impermeable | — | 1.90[c] | 1.62[c] |
| Cubipod (1 layer) | permeable | 2.62[a] | 2.62[b] | 2.62[b] |
| Cubipod (1 layer) | impermeable | — | 1.98[c] | 1.81[c] |
| Cubipod (2 layer) | permeable | 3.48[a] | 3.48[b] | 3.48[b] |
| Cubipod (2 layer) | impermeable | — | — | —[d] |
| Xbloc (1 layer) | permeable | 2.8 | 2.60[e] | 2.45[e] |
| Xbloc (1 layer) | impermeable | 2.22[f] | 2.06[e,f] | 1.94[e,f] |
| Tetrapod (2 layer) | permeable | 2.3 | 2.5 | 2.9 |

[a] Cubipod Manual: $K_D = 12$ (1 layer) and $K_D = 28$ (2 layer) via Hudson at $\cot\alpha = 1.5$. [b] Manual claim of no Hudson scaling beyond $\cot\alpha = 1.5$. [c] Design value $N_{sd} = \min(N_s(\text{IDe}_{5\%})/1.31,\ N_s(\text{IDa}_{5\%})/1.10)$ from the percentile-based safety-factor analysis (table G.2). Cube $\cot\alpha = 2$ applies the same framework to the data of Ruijter (2026). [d] Only one double-layer Cubipod test was run on the impermeable cot 3 cross-section (B1_R1, $n = 1$), so no design value is derived. The lab top-layer threshold IDe,d ($N_{od} = 2.0$) was reached at $N_s \approx 3.82$ (see section 5.2.5). [e] Xbloc Manual slope correction (1.25× weight for slope milder than 2:3, 1.5× for slope milder than 1:2). [f] Xbloc Manual impermeable-core correction (2× weight). Xbloc values derived as $N_s = 2.8/(\text{factor})^{1/3}$ from the cot 1.5 permeable design value. [g] Rock values computed from Van Gent et al. (2003) stability formula for plunging waves ((Rock Manual, 2007) Eq. 5.139) at the $5\,\%$ characteristic coefficient $c_{pl} = \mu - 1.64\sigma = 7.25$ ($\mu = 8.4$, $\sigma = 0.7$), with $S_d = 2$, $N = 1000$, $s_{m-1,0} = 0.04$, and $H_{2\%}/H_s = 1.4$, giving a deterministic design value comparable to the Cubipod $N_{sd}$ and to the Xbloc Manual design values. The older mean-trend values from (Van der Meer, 1988) are not used in this table.

The measured stability values can be placed in the context of the available literature on concrete armour units. The comparison is organised along the two dominant variables in the present study, slope angle and core permeability, and discussed against the predictions of the Hudson formula (Hudson, 1959), the design manuals for single-layer interlocking units (Medina and Gómez-Martín, 2016; Muttray and Reedijk, 2008), and the experimental work on impermeable cores (Reedijk et al., 2008; Ruijter, 2026).

### 6.1.1. Slope dependence

The traditional Hudson formula predicts $H_s/D_n \propto (\cot\alpha)^{1/3}$, anticipating a $14\,\%$ stability gain when moving from a $\cot\alpha = 2$ to a $\cot\alpha = 3$ slope. The measured stability data contradicts this:

- Deviation from Hudson scaling: The mean IDe values drop from $N_s = 3.21$ ($\cot\alpha = 2$) to $N_s = 3.00$ ($\cot\alpha = 3$). This $6\,\%$ decrease directly contradicts the $14\,\%$ stability gain predicted by the Hudson formula.
- Design manual alignment: The results substantiate existing warnings that interlocking armour does not gain stability on milder slopes (Muttray and Reedijk, 2008). While the Cubipod Manual (Medina and Gómez-Martín, 2016) claims Cubipods are not interlocking units, the observed lack of slope-induced stability gain combined with multi-unit extraction (figure 6.2) demonstrates that interlocking is a critical stability factor for Cubipods.
- Loss of gravity-driven interlocking: Interlocking force relies heavily on the along-slope gravity component ($\propto \sin\alpha$). This component drops by $43\,\%$ moving from $\cot\alpha = 1.5$ to $3$, weakening the interlock on the gentle slope.
- Energy concentration: The 1:3 slope forces plunging impacts ($\xi \approx 1.6$), hitting wider clusters simultaneously compared to the collapsing regime ($\xi \approx 2.5$) on the steeper 1:2 slope. As expected on impermeable slopes (Díaz-Carrasco et al., 2020), single-parameter $\xi$ or $\cot\alpha$ scaling is insufficient to capture this response.

The breaker regime is partly a consequence of the fixed wave steepness. Both slopes were tested at $s_{m-1,0} = 0.04$, which puts the 1:3 slope in the plunging regime and the 1:2 slope in the collapsing

regime. A lower steepness would push both slopes towards surging and could recover part of the stability lost on the 1:3 slope. This would, however, compare the two slopes under different waves rather than under the same loading, so it does not change the conclusion for the design condition tested here. The steepness effect is left as a recommendation for further research (section 7.3).

### 6.1.2. Impermeable core penalty

Cross-comparison with literature requires careful alignment of failure definitions, which differ across sources. The present study uses IDa at first extracted unit and IDe at $N_{od} = 0.2$ for single-layer armour (Rock Manual (Rock Manual, 2007) convention for single-layer cubes, Table 5.35), and $N_{od} = 2.0$ for double-layer armour. The Cubipod Manual uses $D_e \geq 4$ via the Virtual Net method (Medina and Gómez-Martín, 2016), a different physical metric that captures compaction in addition to displacement. The Ruijter (2026) cube data have been recomputed at $N_{od} = 0.2$ to match the present convention. Values quoted from Ruijter elsewhere in this chapter follow that recomputation.

Previous literature documents the impermeable-core penalty primarily for other layer types:

- Cubes: $78\,\%$ increase in $D_{n50}$ ($\sim 44\,\%$ drop in $H_s/D_n$) on the IJmuiden cross-section (Reedijk et al., 2008).
- Rock: $59\,\%$ size increase ($\sim 37\,\%$ drop in $H_s/D_n$) when shifting from standard permeability to an impermeable core (Van Gent et al., 2003).
- Cubes on cot 2 impermeable: $H_s/D_n \approx 2.4$–$3.4$ ranges measured by Ruijter (2026).

Applying the Medina et al. (2012) percentile methodology (table G.2) yields design stability numbers for the impermeable cores ($N_{sd} = 1.98$ and $1.81$) that fall significantly below the Cubipod Manual permeable benchmark ($N_s = 2.62$).

These derived results fall significantly below the standard Cubipod Manual design value $N_s = 2.62$ (last column of table 5.2 in chapter 5). The lab versus lab reduction is smaller than the $\sim 44\,\%$ reported for concrete cubes by Reedijk et al. (2008) for the IJmuiden cross-section, but the absence of a matched permeable-core Cubipod dataset at $\cot\alpha = 2$ or $\cot\alpha = 3$ prevents a definitive quantification of the impermeable-core penalty in isolation. Possible contributing factors include the higher Cubipod armour porosity and the geometry of the protrusions, which may shift dissipation from the core to the armour layer itself. Direct testing on permeable cores at $\cot\alpha = 2$ and $\cot\alpha = 3$ is therefore recommended as further research, to isolate the impermeable-core penalty from the slope-angle effect (chapter 7).

The present Cubipod single-layer impermeable measurements (IDa midpoint $N_s = 1.97$–$3.22$ across cot 2 and cot 3) and the cube single-layer impermeable measurement on cot 3 ($N_s = 2.66$, midpoint of measured $H_{m0,\text{inc}}$ with cube constants, $n = 3$) are compiled with the literature in Table 6.1 of chapter 5. For impermeable cores on cot 2 and cot 3 the cube and Cubipod single layer behave similarly in IDa terms, and both fall below the Manual permeable values for the same slopes. The double-layer test B1_R1 reached IDe,d ($N_{od} = 2.0$ in the top layer) at $N_s \approx 3.82$. The bottom layer subsequently reached IDe,s at $N_s \approx 4.56$. Mechanism interpretation of the double-layer result is given in section 6.2. The bottom-layer $N_s \approx 4.56$ is not a standalone single-layer stability result.

### 6.1.3. Cubipod versus cube

Sub-question 2 asks whether the impermeable-core stability shortfall observed for Cubipods is unit-specific. The matched comparison between the present Cubipod data on the 1:2 impermeable cross-section (A1 and A2, $n = 7$ IDe) and the cube data of (Ruijter, 2026) on the same cross-section (S05–S07, $n = 3$), reported in section 5.2.4, shows that Cubipod and cube IDe values agree within the test scatter on this slope (Cubipod pooled mean $N_s = 3.21$, cube mean $N_s \approx 3.1$ with cube constants $\Delta = 1.24$, $D_n = 3.1$ cm). The same direction of underlayer effect is recovered in both datasets ($0.5\,D_n$ marginally above $1.0\,D_n$). The dominant stability-reducing factor on the impermeable core is therefore not specific to Cubipods, and a combined slope and core correction equivalent to the one derived in section 6.1.5 applies to both single-layer unit types on an impermeable cross-section. The same direction of shortfall is observed in the present cube test on the 1:3 impermeable slope (C1, mean IDe $N_s = 2.66$ with cube constants), although the smaller sample ($n = 3$) and the slope-offset relative to Ruijter prevent a quantitative cot 3 cross-comparison. Two points support reading the close cot 2 agreement as a packing rather than a unit-type effect. The cube armour is placed at a lower porosity

($n_v \approx 0.25$) than the Cubipod ($n_v \approx 0.40$), which raises its resistance to the first displacements: the cube IDa on $\cot\alpha = 2$ sits about $6\,\%$ above the Cubipod IDa, while the IDe values agree within the test scatter. The small realized-steepness difference between the two studies ($s_{op} \approx 0.030$ here against $0.035$ in (Ruijter, 2026)) does not contribute, because Cubipod stability is essentially steepness-independent over this range (Medina and Gómez-Martín, 2016).

To clarify the differences and similarities between cubes and Cubipods, table 6.2 lists the derived design stability values. The single-layer cube data are analysed using the same Medina et al. (2012) method as the Cubipod, applying the same no-damage requirement (figure 5.13).

**Table 6.2:** Derived design stability values ($N_{sd}$) for Cubipod and cube on impermeable cores, split by slope.

| Unit type | $\cot\alpha = 2$ | $\cot\alpha = 3$ |
|---|---|---|
| Cubipod (this study) | 1.98 | 1.81 |
| Cube (C1 & Ruijter) | 1.90 | 1.62 |

The design formulation for cubes follows several steps:

- Data conversion: Ruijter's failure points are converted to the $N_{od} = 0.2$ convention, taking the $N_s$ at IDe as the average of the two bracketing wave-height steps (section 3.3).
- Scatter pooling: $\sigma_{\text{IDe}} = 0.18$ and $\sigma_{\text{IDa}} = 0.43$ are pooled within thickness across the five Ruijter $\cot\alpha = 2$ series ($0$ to $5.0\,D_n$) and reused for $\cot\alpha = 3$. The C1 mean enters the cot 3 design value, but C1 itself does not enter the $\sigma$ pool because its three repetitions reached IDa and IDe in the same wave-height step, giving $\sigma = 0$ within the series.
- Slope $\cot\alpha = 2$: using relevant thicknesses ($0.5$ and $1.0\,D_n$), the means are $\mu_{\text{IDa}} = 2.99$ and $\mu_{\text{IDe}} = 3.12$, comparable to the Cubipod at the lab level. Because cubes fail more abruptly (the initiation of damage and the initiation of destruction coincide for the C1 series), a stricter no-damage cap is applied to the cube, $\mathrm{SF}(\text{IDa}_{5\%}) = 1.20$ against $1.10$ for the Cubipod. This sets $N_{sd} = 1.90$, just below the Cubipod ($1.98$). The cube IDa mean is itself inflated by a single high outlier in Ruijter's $0.5\,D_n$ data ($N_s = 3.73$), so with more cube tests the cube value would likely fall further. With so few cube tests this should be read as indicative only.
- Slope $\cot\alpha = 3$: based on the C1 test, $\mu_{\text{IDa}} = \mu_{\text{IDe}} = 2.66$, below the Cubipod ($\mu_{\text{IDe}} = 3.00$). With the same stricter cap the requirement sets $N_{sd} = 1.62$, below the Cubipod ($1.81$), consistent with cubes being both less stable at the lab level and more brittle.

Overall, the severe impermeable-core stability reduction is similar for both units, irrespective of the slope.

### 6.1.4. Reflection coefficients

The reflection coefficients $K_r$ measured at the wave gauges quantify how much wave energy is returned by the structure rather than absorbed in the armour and core ($K_r^2$ is the reflected energy fraction, and $1 - K_r^2$ is the share dissipated by or transmitted into the structure). For both slopes $K_r$ sits between the smooth-impermeable reference of Díaz-Carrasco et al. (2020) and the armoured-permeable reference of Zanuttigh and Van der Meer (2008). This fits the present cross-section: the armour layer adds dissipation compared with a smooth slope, while the impermeable core removes the dissipation that a permeable rubble mound would provide. The implied fraction of incident energy reaching the armour is therefore larger than for a comparable permeable-core configuration, consistent with the impermeable-core penalty discussed above. The full $K_r^2$ comparison is given in Appendix H.

### 6.1.5. Comparison with design guidelines

The back-calculated Hudson coefficient $K_D$ is not slope-invariant for the present single-layer interlocking tests, which confirms that $(\cot\alpha)^{1/3}$ scaling does not apply on these slopes (section 2.3). The back-calculated values and the breakdown are reported in section G.2. Stability is therefore expressed and translated into a design value through the stability number $N_s$, not through $K_D$. Table 6.3 translates the laboratory measurements into design values derived via the Medina et al. (2012) percentile

method, limited by the single-layer no-damage requirement (section 5.5).

**Table 6.3:** Design stability number $N_{sd}$ for single-layer interlocking armour on an impermeable cross-section: present study versus design-guideline conventions. The present values follow the Medina et al. (2012) percentile method limited by the single-layer no-damage requirement (section 5.5). Two Xbloc-derived rows are shown: the strict Xbloc Manual rule, which applies only the single highest weight correction (the impermeable-core factor of $2$) and therefore gives the same value on every slope, and a combined estimate that also applies the mild-slope weight factor.

| Design basis | $\cot\alpha = 2$ | $\cot\alpha = 3$ |
|---|---|---|
| This study (Cubipod, impermeable) | 1.98 | 1.81 |
| Cubipod Manual (permeable) | 2.62 | 2.62 |
| Xbloc Manual (impermeable, highest factor) | 2.22 | 2.22 |
| Xbloc Manual (impermeable, factors combined) | 2.06 | 1.94 |

The derived design values ($N_{sd} = 1.98$ and $1.81$) sit well below the permeable Cubipod Manual design value ($N_s = 2.62$). The difference captures the combined penalty of flattening the slope and introducing the impermeable core. Because the impermeable surface accelerates early unit extractions, it is the safety factor on IDa ($\mathrm{SF}(\mathrm{IDa}_{5\%}) \geq 1.10$) that sets $N_{sd}$ on both slopes, not the IDe margin.

This combined penalty can be checked against the Xbloc Manual, which provides explicit weight multipliers for single destabilising phenomena (Muttray and Reedijk, 2008). For an impermeable structure the Manual applies only the single highest factor, the core factor of $2$, which gives a slope-independent $N_{sd} = 2.22$ and therefore shows no slope effect. The present data show that the 1:3 slope is genuinely less stable than the 1:1.5 slope, so a slope-independent value is optimistic for the gentler slope. Applying the mild-slope factor on top of the core factor gives $2.06$ on $\cot\alpha = 2$ and $1.94$ on $\cot\alpha = 3$. This combined estimate is not a Manual-sanctioned product, but it brackets the test-derived design values from above.

Figure 6.1 places the present safety-factor-derived design values and the Cubipod Manual permeable design value of $N_s = 2.62$ on a single stability chart, showing the contrast between the impermeable cross-section tested here and the permeable design basis.

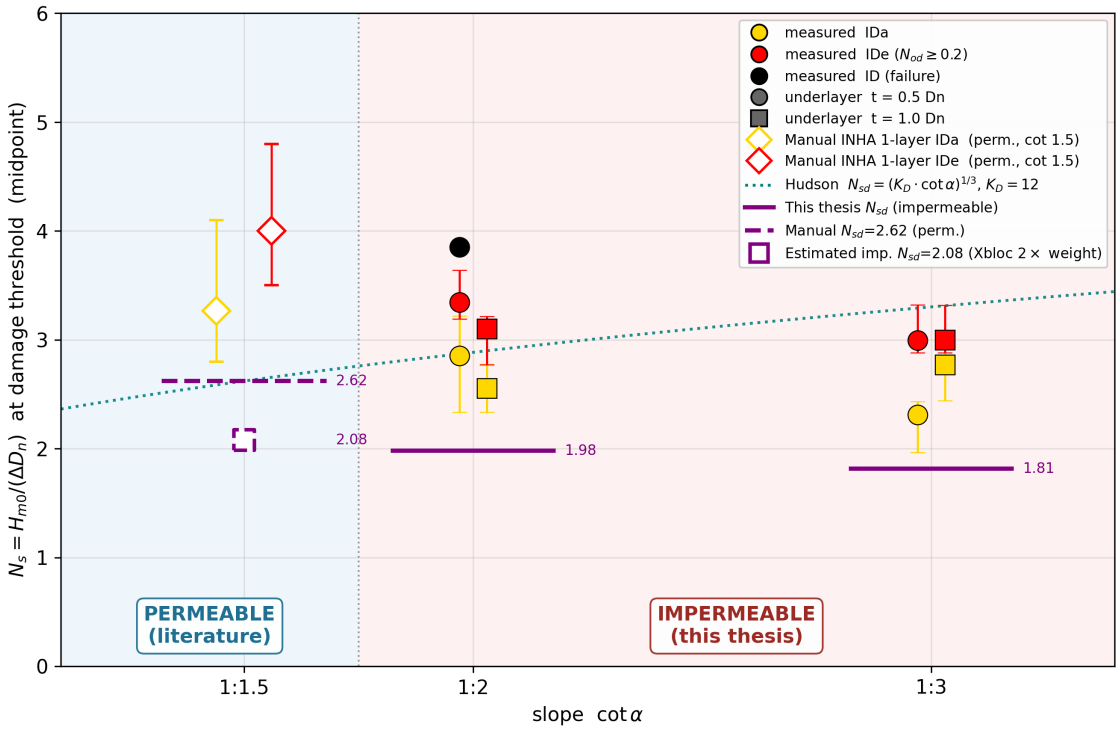


**Figure 6.1:** Design versus design comparison of the present impermeable core measurements with the permeable Cubipod Manual reference, with the stability-number axis starting at zero. Purple solid segments: present SF-derived design values ($N_{sd} = 1.98$ at $\cot\alpha = 2$ and $N_{sd} = 1.81$ at $\cot\alpha = 3$, from the within-config Gaussian method of section 6.1.5). Purple dashed segment: Cubipod Manual permeable design value $N_{sd} = 2.62$ at $\cot\alpha = 1.5$. The open square at $\cot\alpha = 1.5$ is an estimated impermeable design value, obtained by dividing the Manual permeable value by $2^{1/3} \approx 1.26$ (the Xbloc weight-factor correction for an impermeable core). It is uncertain because the factor is calibrated on Xbloc rather than Cubipod and is shown for visual context only. Background shading separates the permeable literature region from the impermeable region tested in this thesis.

The Manual stability calibration assumes a placement porosity of $n_v \approx 40.5\,\%$. The present tests achieved a mean $n_v = 40.1\,\%$ across the range $39$ to $41\,\%$ by hand placement on a dry slope, and one earlier test at the supplier-recommended $n_v = 42\,\%$ failed at the lowest tested wave height and was excluded. Achieving the lab-scale density in prototype placement with a crane in water is unlikely, so the derived values probably overestimate the stability of a prototype slope at the same wave conditions, most so on the 1:3 slope where interlocking is most porosity-sensitive (see table 6.6). The per repetition scatter of $N_s$ at IDe against placement porosity is shown in figure 5.4 (section 5.2.3), and the opposite-sign within-band slopes on the two slopes are reconciled by the re-arrangement modes of section 6.2. A second consequence of the higher Cubipod placement porosity ($n_v \approx 40\,\%$ against $\approx 25\,\%$ for cubes) is that more wave energy is dissipated within the armour layer itself, through turbulent flow around the protrusions. On an impermeable core the underlayer cannot add dissipation by passing water through to the core and serves mainly as geometric support, consistent with the thinner $0.5\,D_n$ underlayer being at least as stable as the thicker $1.0\,D_n$ underlayer (A1 over A2 on $\cot\alpha = 2$, A3 and A4 comparable on $\cot\alpha = 3$).

The Manual design value $N_s = 2.62$ therefore cannot be transferred to the present configuration. The recommended design value for single-layer Cubipod on a 1:3 impermeable slope is $N_{sd} = 1.81$, bracketed from above by the Xbloc-derived combined estimate of $1.94$ for the same slope and core (table 6.3). The prototype-placement porosity bias acts as an additional reserve below this value rather than an adjustment to it, provided strict placement specifications are enforced (chapter 7).

## 6.2. Combined slope and core effects

The gentle-slope and impermeable-core effects discussed separately in section 6.1 act on the same armour layer. The question for this synthesis is which physical mechanism dominates the response

observed in the present data.

The observations point to three mechanisms operating in parallel, summarised in table 6.4: vertical settling of units into the underlayer, lateral wave-induced compaction that tightens the packing and builds inter-unit interlock, and energy dissipation in the underlayer, where a thicker filter was expected to absorb more wave energy and improve stability.

**Table 6.4:** The three armour re-arrangement mechanisms inferred from the present tests. Lateral wave compaction acts in two modes, described in the text below.

| Mechanism | Effect | Scales with | Dominant where |
|---|---|---|---|
| Settling into the underlayer | destabilising | underlayer thickness | both slopes, stronger with a thicker filter |
| Lateral wave compaction | stabilising | along-slope gravity ($\sin\alpha$) | strong on 1:2, weak on 1:3 |
| Energy dissipation in the underlayer | stabilising (expected) | underlayer thickness | a thicker filter was expected to absorb more wave energy and raise stability, but this was not seen in the data |

Two distinct re-arrangement modes underlie lateral wave compaction. On the 1:2 slope (predominantly collapsing breakers, $\xi \approx 2.5$), the larger along-slope gravity component ($\sin\alpha = 0.45$) drives a collective re-arrangement of groups of units. A displaced unit is reseated by neighbouring units that move with it, allowing the layer to re-stabilize before interlocking is lost.

On the 1:3 slope (plunging breakers, $\xi \approx 1.6$), the reduced gravity component ($\sin\alpha = 0.32$) and localized impacts displace individual units rather than groups. A displaced unit loses the support of the units above, which fail to slide down, leading to immediate extraction without replacement. The as-placed packing density is therefore more critical on the gentler slope, because subsequent waves do not close loose spots placed during construction.

For the underlayer thickness effect, Cubipods on the $0.5\,D_n$ filter (A1) are closer to the hard core plank. The plank enforces a more even placement of the units on the steeper slope compared to the thicker $1.0\,D_n$ filter (A2). Additionally, the $0.5\,D_n$ Cubipods settled faster because the thin underlayer itself also settled. This accelerated compaction led to greater interlocking and apparently higher stability. A1 was more stable than A2 on the $1{:}2$ slope. However, even though the armour layer in A1 exhibited higher stability, the underlayer was failing by sliding over the smooth surface of the impermeable core. This underlayer sliding was clearly visible in A1, substantially reduced in A2, and completely undetected on the milder profiles (A3, A4, B1, C1). In a prototype structure, the core roughness would be significantly greater, so this rapid settlement and sliding of the underlayer would likely not occur. Therefore, the increased stability associated with the $0.5\,D_n$ underlayer is a laboratory effect. In reality, a $0.5\,D_n$ underlayer is not more stable than a $1.0\,D_n$ configuration. Nevertheless, the pronounced sliding in A1 demonstrates that an impermeable core introduces a destabilisation risk on steeper profiles if sufficient friction is not provided.

Whether double-layer armour on gentle slopes is inherently brittle remains a subject of discussion, with contrasting views in the literature regarding its self-healing capacity. The double-layer test B1_R1 provides direct support for the lateral wave compaction mechanism. The top layer reaches the destruction threshold at $N_s$ similar to the single-layer A-series, while the bottom layer reaches its own single-layer threshold IDe,s only at $N_s \approx 4.56$ (section 5.2.6). The post-test bottom-layer porosity of $37\,\%$, against $\sim 40\,\%$ as placed for A3 and A4, demonstrates wave-induced compaction occurring while the top layer absorbs the impact. The double layer is therefore not intrinsically more stable per unit. It is the configuration that permits lateral wave compaction to develop before the bottom layer is exposed to its design load.

After the test, pulling by hand on a single Cubipod in the cleared bottom layer moved a cluster of about thirty neighbouring units at several locations: roughly fifteen rose with the pulled unit and another fifteen or so shifted along through the inter-unit contact network. Figure 6.2 sketches the two regimes.

A thicker filter would, in principle, dissipate more of the plunging impact energy in the granular bed

and shield the armour. The data do not support this. On the 1:3 slope, A4 ($1.0\,D_n$) and A3 ($0.5\,D_n$) reach the same pooled mean IDe ($N_s = 3.00$), so any dissipation benefit is below the test scatter. The mechanism is therefore listed as a discussion point, not a confirmed design factor.

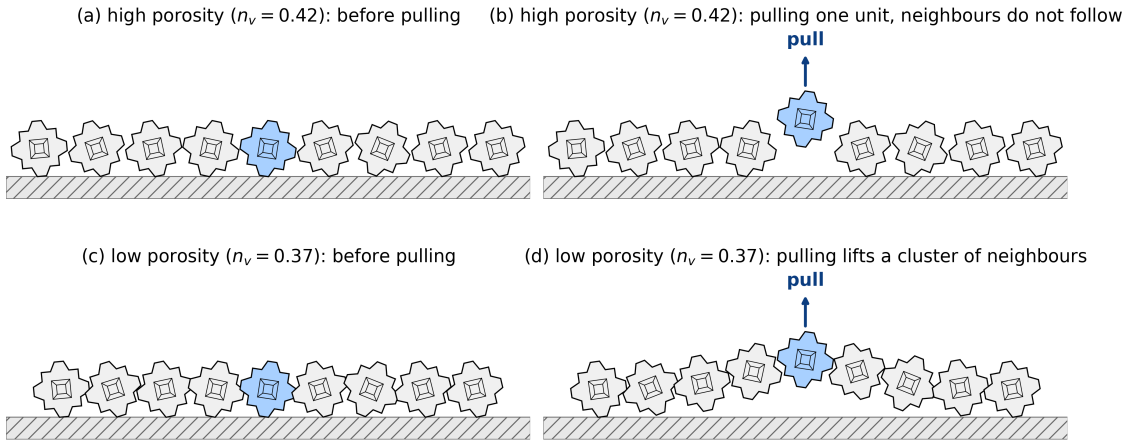


**Figure 6.2:** Schematic of the interlocking effect observed after the B1_R1 test. Top row: high porosity ($n_v = 0.42$). Bottom row: low porosity ($n_v = 0.37$). Left: at rest. Right: centre unit (light blue) pulled vertically. At high porosity only the pulled unit lifts (b). At low porosity it lifts a cluster of neighbours (d). The two-dimensional cross-section underestimates the real effect, because in three dimensions each Cubipod contacts its neighbours over its full surface. Lift magnitudes are illustrative.

Whether thicker filters eventually improve stability cannot be answered with only two thickness points. This is taken up as a recommendation for further research (chapter 7).

## 6.3. Placement grid geometry

The standard placement grid adopted for the campaign (section 3.7, section A.3) is close to the Cubipod Manual grid (Medina and Gómez-Martín, 2016) in the within-row spacing $a$, but reaches the same porosity with a slightly tighter row spacing. The standard grid uses $a/D_n = 1.53$, just below the Manual crane-placement value of $a/D_n = 1.59$, while the along-slope row spacing is $b_{\text{slope}}/D_n \approx 1.06$ to $1.11$, against the Manual $1.22$. The result is a grid that is, if anything, slightly more elongated than the Manual grid ($a/b_{\text{slope}} \approx 1.40$ against $1.30$), not more square.

This is the grid used in all reported A, B and C tests. An earlier trial grid with a smaller $a$ ($a/D_n \approx 1.44$, tests A1_trial and A1_R1) was abandoned before the main campaign, so it does not enter the stability results. The effect of the small remaining grid difference on hydraulic stability is not documented in the literature. Because the standard grid is close to the Manual grid in $a$, the comparison of the present stability numbers with published $1{:}1.5$ slope data using the Manual grid is not strongly affected by grid geometry, and the slope angle and core permeability are the dominant differences.

## 6.4. Practical implications for IJmuiden

The lab core consists of a smooth plywood plank, whereas the IJmuiden cross-section uses an asphalt surface with surface roughness and local irregularities. The smoother lab core allowed more underlayer sliding than the IJmuiden asphalt is likely to permit, particularly on the 1:2 slope where gravity drives sliding (table 6.6). The 1:2 lab measurements are therefore conservative in this respect.

The IJmuiden roundhead is locally as gentle as 1:4. The present trunk-only 1:3 tests are the closest available benchmark, but extrapolation from a 2D trunk geometry to a 3D roundhead is not warranted because oblique wave attack, diffraction and 3D packing transitions are not captured in the present setup. Dedicated 3D basin testing is required for the roundhead and is recommended as further research (chapter 7).

The existing IJmuiden armour of concrete cubes has repeatedly failed in design-storm conditions. The present Cubipod measurements on the same 1:3 impermeable cross-section show a single-layer IDe near $N_s = 3.0$ and an IDa as low as $1.97$ in one repetition (A3_R1). A Cubipod-based replacement

design at IJmuiden is therefore feasible provided that the placement specification holds porosity at $n_v \leq 41\,\%$ and the design $N_s$ is set in the conservative range identified in section 6.1.5. Without both constraints the lab-measured stability cannot be transferred to the prototype with confidence.

### 6.4.1. Prototype Cubipod size

For IJmuiden's ULS design wave $H_{m0,\text{design}} = 7.5$ m and a single-layer Cubipod armour on the 1:3 impermeable slope with a $0.5\,D_n$ underlayer (configuration A3), the prototype size follows from $D_n = H_{m0,\text{design}}/(\Delta \cdot N_{s,\text{design}})$ with $\Delta = 1.24$ for Cubipod concrete in seawater ($\rho_s = 2300$ kg/m$^3$):

- Cubipod Manual permeable design ($N_s = 2.62$): $D_n = 2.31$ m, $m = 28$ tonnes.
- Present impermeable design ($N_s = 1.81$): $D_n = 3.34$ m, $m = 86$ tonnes.

Applying the Manual permeable value directly to the IJmuiden impermeable cross-section therefore under-sizes the unit by a factor of $\sim 2.7$ in mass. While the concrete volume per individual unit increases by nearly $200\,\%$, the total required number of units decreases for a larger $D_n$. Consequently, the total concrete material volume for the entire armour layer increases by about $45\,\%$. The same direction and approximately the same magnitude of correction was reported by Reedijk et al. (2008) for cubes on this cross-section (a $5.6$-fold mass increase required for the impermeable core).

### 6.4.2. Rocking effects

Rocking-induced fatigue is not expected to be a limiting factor for Cubipods on these slopes, as a first-order structural integrity check yields no breakage over a 100-year design life (see chapter E for method and assumptions). Furthermore, in line with the earlier rocking-sensor work on Xbloc (Hofland et al., 2023), per unit rocking does not identify individual unit extraction, while aggregate rocking activity does track the overall damage rate on the $1{:}3$ slope (section D.1), serving as a structure-level indicator rather than a per unit alarm.

Rocking of different armour types can be compared by velocity, but not by stress. The stress also depends on the unit mass, shape, and concrete strength, which differ per type (Hofland et al., 2023). The rocking velocity is written in the Froude-scaled form $\omega^* = |\omega|_{\text{peak}}/\sqrt{g/D_n}$, which does not depend on model scale. It can be compared with the Xbloc design fit for the standard $1{:}1.5$ slope (Hofland et al., 2023) (figure D.2). At the same stability number, the single-layer Cubipod on the $1{:}3$ slope rocks about $1.2$ to $1.8$ times faster than the Xbloc fit. On the $1{:}2$ slope it rocks slower, at about half or less. Rocking increases strongly from the $1{:}2$ to the $1{:}3$ Cubipod slope. The cubic Cubipod shape interlocks less than the hooked legs of the Xbloc, which drives the harder rocking on the gentle $1{:}3$ slope. This does not mean a higher risk of breakage. The solid cube body of the Cubipod is much stronger than the slender Xbloc legs, and the structural check finds no rocking fatigue failure over the design life (chapter E).

## 6.5. Influence factors for IJmuiden

The present programme isolated five design factors (placement porosity, underlayer thickness, slope angle, plunging breaker regime, unit type) plus a single-test comparison of single versus double layer. Within the tested Cubipod porosity range ($n_v = 38$ to $43\,\%$), lower porosity gave higher stability on $\cot\alpha = 2$ (A1 above A2). The same direction was less clear on $\cot\alpha = 3$ (A3 $\approx$ A4), where the more rapid single-step failures and the $n = 4$ samples per cell partially mask the gradient. Ruijter (2026) reports a different porosity trend for cubes, but over a much lower porosity range ($n_v \approx 5$ to $25\,\%$, denser placement) that does not overlap with the Cubipod range tested here. Regularly placed cubes have a geometric porosity ceiling of approximately $35\,\%$: above that the inter-row gap exceeds what allows a cube to rest on the units below, and the placement degenerates from regular to random or rotated. Cubes at the Cubipod $\sim 40\,\%$ porosity would therefore not survive testing. The relevant porosity range is unit-specific, and the two trends are not directly comparable.

The translation of these observations to the IJmuiden prototype is summarised in table 6.5. The dominant uncertainty is the prototype placement porosity, which is likely above the lab range because placement with a crane in water is less precise than hand placement on a dry slope. This biases the lab values upward relative to the prototype. The compaction-history bias (table 6.6) acts in the opposite direction and adds margin. The design recommendation section in chapter 7 weighs these biases against each other.

**Table 6.5:** Influence factors tested in this study: observed effect in the lab, expected effect on the IJmuiden prototype, and design recommendation. The bias direction (lab over- or under-estimating prototype stability) per factor is given in table 6.6.

| Factor | Effect in lab | Expected on IJmuiden prototype | Recommendation |
|---|---|---|---|
| Placement porosity (Cubipod, $n_v = 38$–$43\,\%$) | Lower porosity gave higher stability on $\cot\alpha = 2$ (A1 above A2), less clear on $\cot\alpha = 3$ (A3 $\approx$ A4) | Placement with a crane in water likely yields higher porosity than the lab, and lab values probably over-estimate prototype stability | Hard upper limit $n_v \leq 41\,\%$ in the placement specification |
| Underlayer thickness | $\cot\alpha = 2$: $0.5\,D_n$ above $1.0\,D_n$ (A1 above A2), $\cot\alpha = 3$: comparable (A3 $\approx$ A4) | Effect expected to persist, and thinner filter also saves material | $0.5\,D_n$ as default for impermeable Cubipod configurations |
| Slope angle (Hudson breakdown) | $\cot\alpha = 3$ gave no stability gain over $\cot\alpha = 2$, pooled mean IDe $N_s = 3.0$ versus $3.2$ | Same effect at prototype scale (Hudson scaling does not hold for single-layer interlocking units) | Apply slope correction in the style of the Xbloc Manual. Design $N_{sd} = 1.81$ on $\cot\alpha = 3$ (section 6.1.5) |
| Plunging breaker regime on $\cot\alpha = 3$ | Wider damage clusters and rapid single-step failures, against gradual damage progression on $\cot\alpha = 2$ | Plunging regime active at IJmuiden design $H_s$ on the 1:3 trunk ($\xi \approx 1.6$), and same failure character expected | Use the IDa minimum (not the IDe mean) as the design reference on $\cot\alpha = 3$ |
| Unit type (Cubipod vs cube) | On $\cot\alpha = 3$ Cubipod IDe ($N_s = 3.0$) and cube IDe ($N_s = 2.66$) are within scatter, but Cubipod is placed at $n_v \approx 40\,\%$ against $\sim 25\,\%$ for cubes, so it covers more armour area with less concrete. The B1 pull demonstration (section 6.2) shows Cubipod transferring load to a cluster of neighbours, indicating a more self-healing layer response | Same direction at prototype scale: comparable stability with lower Cubipod concrete volume, plus more graceful damage progression between IDa and IDe | Cubipod preferred over cubes on $\cot\alpha = 3$ for IJmuiden: comparable stability, lower concrete volume, and more self-healing layer response |
| Layer count (single vs double) | B1 top layer fails at $N_s$ comparable to single-layer A4. Bottom layer survives $N_s \approx 4.56$ thanks to wave-induced compaction during top-layer build-up | Same effect, and double layer provides structural redundancy rather than a higher design $N_s$ for the intact armour | Prefer a single layer of larger units over a double layer of smaller units. Both can meet ULS, but the single layer is simpler to place |

## 6.6. Model limitations

The laboratory configuration differs from a built prototype breakwater in several respects. Table 6.6 summarises the relevant factors with the expected direction of bias on the measured stability. The dominant items are the compaction history (which the lab underestimates), the placement porosity (which the lab overestimates), and the underlayer sliding on the smooth core (which the lab underestimates only on the 1:2 slope). These should be covered explicitly in the design recommendation (chapter 7).

**Table 6.6:** Factors affecting the transfer of lab stability measurements to a built prototype. Direction column: *over* = lab overestimates prototype stability, *under* = lab underestimates, *mixed* = both directions present, *?* = uncertain.

| Factor | Dir. | Mechanism and slope sensitivity |
|---|---|---|
| *Stability-mechanism scaling* | | |

*continued on next page*

*(Table 6.6 continued)*

| Factor | Dir. | Mechanism and slope sensitivity |
|---|---|---|
| Compaction history | under | Lab compaction was a single short run of about 500 to 600 waves at $H_{m0} = 8$ cm. The prototype instead accumulates many seasons of storms before it ever sees the design storm, so it experiences far more wave cycles than the lab, which should compact it more and raise its stability (lab is a lower bound). Two points temper this. First, most of the compaction seen in the lab occurred at high wave heights, near or above the design $N_s$, whereas the pre-design storms in the field are all smaller than the design storm and so compact the armour less per event. The prototype gain is therefore a balance between many small storms (more cycles) and their smaller size (less compaction each), and is smaller than a simple "seasons of waves" argument suggests. Second, the effect is strongest on the 1:3 slope where gravity-driven compaction during placement is weak. The double-layer test bottom-layer porosity ($37\%$ after vs $\sim 40\%$ as-placed) and its survival to $N_s \approx 4.56$ show that wave-induced compaction does occur and does add stability. |
| Placement porosity | over | Lab placement was by hand on a dry slope ($n_v = 40.1\%$ mean, close to Manual $40.5\%$). Prototype placement with a crane in water is less precise and typically yields higher porosity, which reduces interlocking. The effect is more pronounced on the 1:3 slope where interlocking is the dominant stability mechanism. The supplier-recommended $42\%$ porosity was tested once and failed immediately, supporting a hard $n_v \leq 41\%$ specification. |
| Underlayer sliding (S-profile) | under | On the 1:2 slope the underlayer slid along the smooth plywood core, forming an S-profile. This is a failure mode in itself: the armour loses its design geometry without units necessarily being extracted. The IJmuiden asphalt core is rougher and likely does not allow this sliding to develop. The 1:2 lab measurements therefore include a failure mechanism that is probably absent in the prototype. |
| Underlayer thickness sensitivity | ? | The optimum thickness is slope-dependent and not monotonic: $0.5\,D_n$ outperforms $1.0\,D_n$ on cot 2, while $1.0\,D_n$ outperforms $0.5\,D_n$ on cot 3 (small samples). Prototype thickness specifications need to be matched per slope. Extrapolating a single value across slopes is not supported. |
| *Geometry* | | |
| Long slope length (40+ rows) | mixed | The model has 41 rows, while a typical design has $\sim 25$. (1) More units along the slope means more chances per width for any unit to be extracted. This is a small effect because the highest extraction risk is at SWL and that band is similar in both lab and prototype. (2) More rows above SWL press down on the lower rows, increasing self-weight stabilisation of the most damage-prone rows around SWL, stronger on 1:2 where the gravity component is larger. |
| Cross-section height and water level | mixed | The lab has fixed water depth well below the crest, so many rows sit above SWL. The IJmuiden ULS storm has water close to the crest with overtopping, so few rows sit above SWL. This works in two opposite directions. The extra rows above SWL press down on the lower rows and protect the most damage-prone band around SWL, which the prototype lacks (lab favourable). On the other hand the wooden support plank rises above the armour crest, so run-up that passes the armour crest hits the smooth impermeable plank and drains straight back over the armour face, loading it, whereas at IJmuiden part of the water passes over the crest and relieves that load (lab unfavourable). |
| 2D versus 3D geometry | over | Tests simulate the trunk only. The roundhead is subject to oblique wave attack, diffraction, and 3D packing transitions not captured in 2D. The present results should not be applied to the roundhead without dedicated 3D basin tests. |
| Idealised toe | ? | The lab toe is over-designed to prevent toe failure from interfering with armour stability. The prototype toe is itself a design element whose response couples back into armour stability through bedding support. |
| *Wave loading* | | |

*continued on next page*

*(Table 6.6 continued)*

| Factor | Dir. | Mechanism and slope sensitivity |
|---|---|---|
| Storm duration / wave count | over | Each lab step ran for $1000\,T_p$, about 1000 to 1040 waves (the compaction run was shorter). A real design storm produces more design-level waves. Cumulative damage continues to develop with wave count. |
| Wave spectrum shape | ? | The lab used a single-peak JONSWAP spectrum ($\gamma = 3.3$, $s_{0m} = 0.04$). The North Sea has a similar steepness range, but produces multi-peaked spectra combining wind sea and swell. The net effect of multi-peakedness on stability is unclear. |
| Directional spread | under | The flume produces head-on waves with no directional spread. Real wave climates spread energy over angles, reducing peak energy aligned with the structure normal. Lab head-on tests are therefore more demanding. |
| Realized wave steepness | mixed | The target spectral steepness was $s_{m-1,0} = 0.040$, while the realized incident value is about $15\%$ lower ($s_{m-1,0} \approx 0.034$, $T_p$-based $s_{op} \approx 0.030$), because the incident height at the toe is below the machine setting and the highest steps broke seaward of the structure. The Cubipod Manual stability tests span $s_{0p} \approx 0.01$ to $0.06$ and show design stability to be essentially independent of steepness over this range (Medina and Gómez-Martín, 2016), so the shortfall does not bias the reported stability numbers and does not account for the unit-type comparison of section 6.1.3. |
| *Methodology* | | |
| Number of repetitions | ? | Per configuration: A1 $n = 6$, A2–A4 $n = 4$, C1 $n = 3$, B1 $n = 1$. Small samples carry sampling uncertainty on the reported IDa/IDe ranges. |
| Wave-height step resolution | ? | The protocol applies seven $H_{m0}$ steps from $10$ to $22$ cm in $2$ cm increments (plus a separate compaction run at $H_{m0} = 8$ cm), each at $1000$ waves. This is consistent with the Hydralab III recommendation of $3$ to $7$ incremental tests of $500$ to $3000$ waves each, with a statistical-relevance threshold of $> 1000$ waves (Wolters et al., 2010). IDa and IDe are reported as the midpoint between bracketing $2$ cm steps, with a per test resolution of $\Delta N_s \approx 0.24$ (Cubipod constants). The actual failure $H_{m0}$ within each $2$ cm interval is not resolved. Most failures on the 1:3 slope occurred within steps 1 to 3 ($H_{m0} \leq 14$ cm), giving 2 to 3 stability data points per repetition below failure on that slope. |

The columns of units against the flume sidewalls were held by steel chains and could not be extracted, so the free width is about $15$ columns rather than $16$. Correcting for this would raise every reported $N_{od}$ by about $7\%$, and the smallest detectable $N_{od}$ from $0.04$ to $0.043$. The damage thresholds and design values are not affected, because IDa is still the first extracted unit and $N_{od} = 0.2$ is still reached at five extracted units. Only the $N_{od}$ magnitudes shift, not the $N_s$ values at IDa and IDe on which the design is based.

# 7

# Conclusions and recommendations

This chapter presents the conclusions in response to the research questions (section 7.1), the design recommendations for Rijkswaterstaat (section 7.2), and the recommendations for future research (section 7.3). For self-contained reading: $N_s = H_{m0,\text{inc}}/(\Delta\, D_n)$ is the stability number based on the incident wave height at the structure toe. $N_{od}$ is the damage number (extracted units per strip of width $D_n$). IDa is the initiation of damage (first extracted unit) and IDe the initiation of destruction of the armour layer ($N_{od} = 0.2$ for single-layer armour, $N_{od} = 2.0$ for double-layer armour). Because the wave height was raised in steps, the $N_s$ at each threshold is reported as the average of the last step without the damage state and the first step with it.

## 7.1. Conclusions

The main research question is:

> *How do Cubipod armour units perform on gentle slopes (1:2, 1:3) with an impermeable core in terms of hydraulic stability and failure mechanisms?*

The answer follows from four sub-questions, each addressed below, with the main answer at the end.

1. *Slope angle (1:2 vs 1:3).* The 1:3 slope has lower stability than the 1:2 slope. The mean $N_s$ at IDe is $3.21$ on $\cot\alpha = 2$ (A1 and A2 pooled) and $3.00$ on $\cot\alpha = 3$ (A3 and A4 pooled), a $6\,\%$ decrease where the Hudson scaling predicts a $14\,\%$ increase. The stability therefore drops on the gentler slope instead of rising, which shows that the Hudson slope scaling does not hold for these single-layer interlocking units. Translating the laboratory data into design values sets $N_{sd} = 1.98$ on $\cot\alpha = 2$ and $N_{sd} = 1.81$ on $\cot\alpha = 3$. Both values are set by the safety factor on the initiation of damage (IDa). The single-layer design is held below the first unit extraction at the design wave height, rather than allowing a limited amount of damage as for double-layer armour. Both design values lie well below the benchmark Cubipod Manual permeable design value of $N_s = 2.62$.
2. *Cubipod versus cube on the 1:2 reference slope.* Cubipods on $\cot\alpha = 2$ (mean IDe $N_s = 3.21$) and concrete cubes on the same slope and core from (Ruijter, 2026) (mean IDe $N_s \approx 3.1$) give comparable stability at the lab level. Once the greater brittleness of the cube is accounted for through a stricter no-damage margin, the matched-slope design value is slightly lower for the cube ($N_{sd} = 1.98$ for Cubipod versus $1.90$ for cube, see section 6.1.3). The slope-related stability decrease observed in this thesis is therefore not specific to Cubipods. Both unit types respond similarly to the impermeable-core configuration.
3. *Underlayer thickness and settlement.* On the 1:2 slope the thinner $0.5\,D_n$ underlayer gives a slightly higher mean IDe than the $1.0\,D_n$ underlayer ($N_s = 3.35$ for A1 against $3.10$ for A2, the difference driven by one low repetition in A2, with the medians coinciding at $3.21$). On the 1:3 slope the two thicknesses give comparable mean IDe (both $N_s = 3.00$). The effect interacts with placement porosity: when comparison is restricted to the $39$–$41\,\%$ porosity band, the gap narrows on both slopes. Settlement during the compaction run was more pronounced on $\cot\alpha = 2$ than

on $\cot\alpha = 3$ because of the larger along-slope gravity component. The double-layer test (B1) showed a bottom-layer porosity reduction (i.e. porosity of the lowest of the two Cubipod layers) from approximately $40\,\%$ as placed to $37\,\%$ after the test, demonstrating wave-induced compaction occurring while the top layer absorbed the impact.

4. *Failure mechanisms.* On the 1:3 impermeable slope, damage progresses rapidly. Once initiated, tens of units are extracted within a single wave-height step, opening a breach 5 to 8 rows wide around the still water level. Units are extracted during both the plunging impact and the downrush of the same wave. This differs qualitatively from the gradual damage progression observed on steeper permeable rubble-mound structures, where damage propagates by adjacent extraction of one or two units per step. The embedded rocking sensors were used on both slopes. Their activity rose with the measured damage on the 1:3 slope (Spearman $\rho = 0.58$ to $0.69$), but showed no such relation on the 1:2 slope, where little damage developed. As in the earlier rocking-sensor work on Xbloc (Hofland et al., 2023), the signal shows the overall condition of the armour, but cannot tell which individual unit will be extracted.

Bringing the four answers together: on gentle slopes with an impermeable core, single-layer Cubipod armour performs worse than the conventional design rules predict, not better. The stability does not rise on the milder slope as Hudson scaling assumes, because the interlocking that Cubipods rely on weakens as the slope flattens. The failure mode also changes. Instead of losing a few units at a time, the armour on the 1:3 slope collapses quickly within a single wave-height step once the first units are extracted. These two effects together place the design stability number well below the Cubipod Manual permeable benchmark. Cubipods remain a feasible choice for the IJmuiden reconstruction, but only with a corrected, lower design stability number ($N_{sd} = 1.8$) and a strict placement-porosity limit ($n_v \leq 41\,\%$) to keep the interlocking effective. The specific design recommendations follow in section 7.2.

## 7.2. Design recommendations

For a Cubipod-based replacement of the IJmuiden Southern Breakwater on the 1:3 impermeable cross-section, the present results support the recommendations below. The primary sources of bias between laboratory and prototype are the compaction history (the lab underestimates prototype stability because the prototype is compacted after a series of pre-design storms) and the placement porosity. For Cubipods the lab overestimates prototype stability because hand placement on a dry slope typically yields a lower porosity than crane placement in water. For single-layer cubes the porosity gap is smaller and the prototype porosity can match the lab value. These are summarised in table 6.6 and per factor in table 6.5. The recommendations below are framed around these biases.

1. *Placement porosity and placement quality.* Specify $n_v \leq 41\,\%$ as a hard upper limit in the placement specification. The supplier-recommended $n_v = 42\,\%$ failed at the lowest tested wave height in a single lab test. The Cubipod Manual stability calibration is based on $n_v = 40.5\,\%$, and no published Cubipod stability data at $n_v \geq 41\,\%$ was found, so the supplier-recommended value is not supported by the present data or by other Cubipod tests in the literature. The placement specification should require rebuild if a sample area exceeds the threshold. Porosity alone is not sufficient: the specification should also require that each placed unit rests in contact with two units of the row below and with the underlayer, so that the interlocking the stability relies on is actually formed.
2. *Design stability number.* Use $N_{sd} = 1.8$ for single-layer Cubipod on the 1:3 impermeable cross-section. This follows from the Medina (2012) percentile method. On this slope the safety factor on IDa sets $N_{sd} = N_s(\mathrm{IDa}_{5\%})/1.10 = 1.81$, where $\mathrm{SF}(\mathrm{IDa}_{5\%}) = 1.10$ is applied to the $5\,\%$-fractile of the laboratory wave height at the initiation of damage (calibrated to Medina's single-layer Cubipod reference value $\mathrm{SF}(\mathrm{IDa}_{5\%}) = 1.06$). The value is supported independently by the value of $1.94$ derived from the Xbloc Manual using the multiplied impermeable and gentle-slope correction factors. The prototype-placement porosity bias gives a further reserve below this value. On the 1:2 slope the corresponding value is $N_{sd} = 1.98$ (the requirement sets the design on both slopes).
3. *Underlayer thickness, stone size and finish.* A $0.5\,D_n$ underlayer is sufficient on the impermeable core. The present data show no stability benefit from doubling the underlayer to $1.0\,D_n$ on either

slope, and the thinner filter reduces material cost. This contradicts the standard Cubipod Manual recommendation of $\sim 1\, D_n$, which was calibrated on permeable cores. For the underlayer stone size, the $W/20$ used here (the lighter end of the Cubipod Manual $W/10$ to $W/20$ range) performed well and is the cheaper choice, so it is recommended. The underlayer should be profiled as smoothly as possible, so that the Cubipods placed on it sit evenly and none protrude, since protruding units are more exposed to wave attack. Underlayer stones were only displaced at wave heights well above the design level ($N_s > 3$ in the single-layer tests, and only above $N_s \approx 4$ in the double-layer test), so underlayer stability is not a concern at the recommended design $N_{sd} \leq 2.0$.

4. *Layer count.* A single-layer placement at the conservative design $N_s$ above is the primary configuration. A double-layer placement provides structural redundancy (the bottom layer of test B1 survived to $N_s \approx 4.56$ after top-layer destruction) but does not raise the intact-armour design $N_s$ and is therefore not required by ULS criteria.
5. *Cross-section verification before roundhead application.* The present 2D trunk results must not be applied to the IJmuiden roundhead without dedicated 3D basin tests. The roundhead is locally as gentle as 1:4 and is subject to oblique wave attack and diffraction not captured in the 2D setup.

### 7.2.1. Design stability and constructability limits

The recommended design stability number for single-layer Cubipod armour on an impermeable 1:3 slope is $N_{sd} = 1.81$, and $N_{sd} = 1.98$ on the 1:2 slope. Both follow from a strict no-damage margin of $1.10$ applied to the $5\,\%$ characteristic value of the initiation of damage (section 5.5), which leaves a destruction margin of $\mathrm{SF}(\mathrm{IDe}_{5\%}) \approx 1.43$ on both slopes, above the $1.31$ of the permeable Cubipod design basis (Medina et al., 2012).

Applying a more conservative safety factor to absorb potential construction inaccuracies is not recommended, because it pushes the design beyond practical constructability limits. The required concrete mass scales with the inverse cube of the stability number, so lowering $N_{sd}$ from $1.81$ to a more conservative $1.74$ would inflate the required unit mass by over $12\,\%$, raising it from an already large $\sim 86$ tonnes to nearly $100$ tonnes per unit at the IJmuiden design conditions ($H_{m0} \approx 7.5\,\mathrm{m}$, section 6.4.1). Units of this scale approach the limits of offshore crane capacity and introduce severe thermal-cracking risk during concrete curing.

Consequently, the efficiency of the $N_{sd} = 1.81$ design is strictly conditional on precise execution. The placement specification must enforce a hard upper limit on the as-built porosity of $n_v \leq 41\,\%$, and surveying must verify that the units are placed in physical contact with their neighbours. If marine contractors cannot guarantee these tolerances during underwater placement, the interlocking mechanism is compromised and the proposed safety factor is voided.

## 7.3. Future research

The present test programme leaves several open questions that follow directly from the gaps identified in the discussion. The recommendations below are ordered by direct relevance to the IJmuiden project. Each is paired with the specific question it would resolve.

1. *3D basin tests for the IJmuiden roundhead at locally 1:4 slopes.* The present 2D trunk results cannot be transferred to the roundhead because oblique wave attack, diffraction and 3D packing transitions are not captured in 2D. Tests on the IJmuiden roundhead geometry at its locally gentler slopes (up to $\cot\alpha = 4$) are required before Cubipods can be specified for that part of the structure.
2. *Permeable-core Cubipod tests at* $\cot\alpha = 2$ *and* $3$*.* The impermeable-core penalty for Cubipods cannot be precisely quantified because no matched permeable-core dataset exists at these slopes. Direct testing on permeable cores would isolate the core-permeability effect from the slope effect and refine the design correction factor derived in section 6.1.5.
3. *Long-duration loading on the 1:3 slope.* The present protocol applies a run duration of $1000\,T_p$ per step, about 1000 to 1040 waves. Long-duration tests ($3000$ to $5000$ waves) at a fixed subcritical $H_{m0}$ on the 1:3 slope would quantify creep behaviour and determine whether Cubipods on impermeable gentle slopes are susceptible to long-term settlement-driven failure, the regime

in which the present catastrophic single-step failures developed. A complementary protocol of extended compaction at the lowest wave-height step (for example $3000$ waves at $H_{m0} = 8$ cm, with re-measurement of the placement spacings $a$ and $b_{\text{slope}}$ before and after) would separate how much of the packing comes from the initial placement and how much from settling under wave loading, which is the main uncertainty in the porosity interpretation of section 6.2. The double-layer test B1 motivates this question: the bottom-layer porosity dropped from approximately $40\,\%$ as placed to $37\,\%$ after the test under damped loads from the top layer, while no comparable bulk porosity reduction was observed in any single-layer 1:3 repetition.

4. *Underlayer thickness sweep ($3$–$5\,D_n$).* The present programme tested two underlayer thicknesses ($0.5$ and $1.0\,D_n$) and found no clear improvement with the thicker filter. A thicker filter ($3$ to $5\,D_n$) might still recover stability by dissipating more plunging-impact energy in the underlayer before it reaches the armour, but this cannot be tested with only two thickness points. Testing $3\,D_n$ and $5\,D_n$ on the 1:3 slope would show whether a thicker underlayer keeps improving stability or whether there is a best thickness, and would help set the underlayer for IJmuiden.
5. *Additional repetitions per configuration.* The present design $N_s$ derivation (section 6.1.5) rests on $n = 4$ per configuration for the A-series and $n = 1$ for B1. Adding repetitions, particularly to the double-layer B1 (currently $n = 1$) and to the design-relevant 1:3 series A3 and A4, would tighten the confidence interval on the lab IDe mean and on the SF-derived design $N_s$, and would reduce the residual uncertainty in the prototype Cubipod size derived in section 6.4.1.
6. *Prototype rocking-sensor deployment and rocking-data analysis methods.* Deploying embedded rocking sensors on an existing prototype Cubipod breakwater would validate the laboratory rocking methodology, set monitoring thresholds for real-time structural health monitoring, and provide prototype rocking intensities under storm conditions. Further development of the rocking-data analysis methodology is equally needed, including extension of the structural-integrity check piloted in chapter E (translation of impact velocities derived from rocking into prototype fatigue damage) and per event signal analysis aimed at distinguishing rocking from extraction precursors at the per unit level.
7. *Wave-steepness effect on the slope comparison.* The present tests used a fixed wave steepness $s_{m-1,0} = 0.04$, which gave plunging waves on the 1:3 slope and surging waves on the 1:2 slope. The slope-related stability shortfall on 1:3 may therefore include a wave-type component. Tests at a lower steepness (for example $s_{m-1,0} = 0.02$), giving surging waves on both slopes, would isolate the slope effect from the breaker-type effect.
8. *Crest-height effect on the slope comparison.* If the prototype is significantly lower-crested than the model, the overburden from the upper armour rows is reduced, possibly weakening interlocking and the 1:2 stability advantage observed here. Test photographs of the present 1:2 series suggest that compaction and settlement at IDa and IDe were concentrated in the rows 4 to 8 below SWL, while the 20-plus rows above SWL did not settle or compact. The 1:2 stability advantage observed here may therefore not depend on overburden from those high rows, but a dedicated low-crested 1:2 test would confirm this and quantify whether the 1:3 versus 1:2 conclusion transfers to the low-crested IJmuiden geometry.

# References


Battjes, Jurjen A. (1974). “Surf Similarity”. In: *Coastal Engineering 1974*. ASCE. DOI: 10.1061/9780872621138.029.

Bosboom, Judith and Marcel J.F. Stive (Jan. 2023). *Coastal Dynamics*. TU Delft OPEN Books. DOI: 10.5074/T.2021.001. URL: https://books.open.tudelft.nl/home/catalog/book/202.

Burcharth, H. F. (1992). “Design of Breakwaters”. In: *Coastal, Estuarial and Harbour Engineering Reference Book*. Ed. by M. B. Abbott and W. A. Price. London: Chapman & Hall, pp. 381–424.

Burcharth, H. F., M. Christensen, T. Jensen, and P. Frigaard (1998). “Influence of Core Permeability on Accropode Armour Layer Stability”. In: *Proceedings International Conference Coastlines, Structures and Breakwaters*. London: Thomas Telford, pp. 34–45.

Burcharth, Hans, Thomas Andersen, and Josep Medina (2011). “Stability of Cubipod armoured roundheads in short-crested waves. A comparison between Cubipod and cube armour stability”. In: *Proceedings of the International Conference on Coastal Engineering; No 32 (2010): Proceedings of 32nd Conference on Coastal Engineering, Shanghai, China, 2010.; structures.39* 1. DOI: 10.9753/icce.v32.structures.39.

Caldera, Ganga (2019). “Rocking of Single-Layer Armour Units on a Breakwater”. MSc thesis. Delft University of Technology. URL: https://resolver.tudelft.nl/uuid:218c0062-4eed-474f-b3bc-25bd0374bf2e.

CIRIA, CUR, and CETMEF (2007). *The Rock Manual: The Use of Rock in Hydraulic Engineering*. 2nd ed. C683. Reprinted 2012. London, UK: CIRIA. ISBN: 978-0-86017-683-1.

Corredor, Antonio, Moises Santos, M. Esther Gómez-Martín, and Josep R. Medina (2012). “Placement of Cubipod armor units in San Andres breakwater (Port of Malaga, Spain)”. In: *International Conference on Coastal Engineering*. DOI: 10.9753/icce.v33.structures.6.

Corredor, Antonio, Rafael Torres, Juan V. Miñana, Enrique Fernández, Carlos F. Menéndez, Moisés Santos, M. Esther Gómez-Martín, Roman Goumy, and Josep R. Medina (2008). *Casting system and drop tests of the Cubipod armor unit*. Conference paper, available via Cubipod Documentation and Publications. URL: https://www.cubipod.com/en/documentation/publications/.

Corredor, Antonio, Rafael Torres, Juan Vicente Miñana, Enrique Fernández, Carlos Fermín Menéndez, Moisés Santos, M. Esther Gómez-Martín, and Josep R. Medina (2010). “Drop tests of prototype cube and Cubipod armor units”. In: *Coastal Engineering Proceedings*. Vol. 1. 32. Shanghai, China: ASCE, structures.43. DOI: 10.9753/icce.v32.structures.43.

Delta Marine Consultants (2024). *Guidelines for Xbloc and XblocPlus Design*. Tech. rep. Delta Marine Consultants. URL: https://www.xbloc.com/sites/bamc/files/2024-02/guidelines-for-xbloc-and-xblocplus-design-2024.pdf (visited on 05/25/2026).

Díaz-Carrasco, Pilar, M. Victoria Moragues, María Clavero, and Miguel A. Losada (2020). “2D water-wave interaction with permeable and impermeable slopes: Dimensional analysis and experimental overview”. In: *Coastal Engineering* 158, p. 103682. DOI: 10.1016/j.coastaleng.2020.103682.

European Committee for Standardization (2004). *EN 1992-1-1:2004 Eurocode 2: Design of Concrete Structures – Part 1-1: General Rules and Rules for Buildings*. CEN. Brussels.

Gómez-Martín, M. and Josep Medina (2008). “Erosion of cube and cubipod armor layers under wave attack”. In: pp. 3461–3473. ISBN: 9789814277365. DOI: 10.1142/9789814277426_0287.

— (2009). “CUBIPOD CONCRETE ARMOUR UNIT AND HETEROGENEOUS PACKING”. In: pp. 140–151. ISBN: 9789814280990. DOI: 10.1142/9789814282024_0013.

Gómez-Martín, M. E. and J. R. Medina (2014). “Heterogeneous Packing and Hydraulic Stability of Cube and Cubipod Armor Units”. In: *Journal of Waterway, Port, Coastal, and Ocean Engineering* 140.1, pp. 100–108. DOI: 10.1061/(ASCE)WW.1943-5460.0000223.

Google (2026). *Google Maps: IJmuiden port entrance*. URL: https://www.google.com/maps (visited on 01/05/2026).

Hofland, Bas, Daan Houtzager, Ganga Caldera, Alessandro Antonini, Marcel Van Gent, Pieter Bakker, and Cock Van der Lem (2023). “Rocking of single-layer armour units measured by embedded sensors”. In: *Journal of Coastal and Hydraulic Structures* 3. DOI: 10.59490/jchs.2023.0028.

Hudson, R. Y. (1959). “Laboratory Investigation of Rubble-Mound Breakwaters”. In: *Journal of the Waterways and Harbors Division* 85.3, pp. 93–122.

Levene, Howard (1960). “Robust Tests for Equality of Variances”. In: *Contributions to Probability and Statistics: Essays in Honor of Harold Hotelling*. Ed. by Ingram Olkin. Stanford, CA: Stanford University Press, pp. 278–292.

Lomonaco, Pedro, Cesar Vidal, Josep Medina, and M. Gómez-Martín (2010). “Evolution of damage on roundheads protected with Cubes and Cubipod armour units”. In: pp. 169–180. ISBN: 978-0-7277-4159-2. DOI: 10.1680/cmsb.41301.0014.

Mansard, E.P.D. and E.R. Funke (1980). “The Measurement of Incident and Reflected Spectra Using a Least Squares Method”. In: *Proceedings of the 17th International Conference on Coastal Engineering*. Sydney, Australia: ASCE, pp. 154–172.

Medina, Josep, M. Gómez-Martín, and Paseo Castellana (2010a). “Influence of armor unit placement on armor porosity and hydraulic stability”. In: *Proceedings of the International Conference on Coastal Engineering; No 32 (2010): Proceedings of 32nd Conference on Coastal Engineering, Shanghai, China, 2010.; structures.41*. DOI: 10.9753/icce.v32.structures.41.

Medina, Josep R., M. Esther Gómez-Martín, and Antonio Corredor (2012). “KD and safety factors of concrete armor units”. In: *Coastal Engineering Proceedings* 1.33. DOI: 10.9753/icce.v33.structures.29.

Medina, Josep R., M. Esther Gómez-Martín, Moises Santos, et al. (2010b). “Prototype drop tests of cube and Cubipod armor units”. In: *Journal of Waterway, Port, Coastal and Ocean Engineering*. DOI: 10.1061/(ASCE)WW.1943-5460.0000064.

Medina, Josep R. and María Esther Gómez-Martín (2016). *Cubipod® Manual 2016*. Double-blind reviewed publication. Valencia, Spain: Editorial Universitat Politècnica de València. ISBN: 978-84-9048-538-5.

Molines, Jorge, Maria Piedad Herrera, and Josep R. Medina (2014). “Laser Scanner Technique to Quantify Randomness in Cube and Cubipod Armor Layers”. In: *Journal of Waterway, Port, Coastal and Ocean Engineering*. DOI: 10.1016/j.oceaneng.2014.06.012.

Molines, Jorge and Josep R. Medina (2011). “Stability of Crown Walls of Cube and Cubipod armored mound breakwaters”. In: *PIANC-Copedec*.

Molines, Jorge, Tomas Perez, Guillermo Zarranz, and Josep Medina (2012). “Influence of Cube and Cubipod Armor Porosity on Overtopping”. In: vol. 1. DOI: 10.9753/icce.v33.structures.43.

Montgomery, Douglas C. (2017). *Design and Analysis of Experiments*. 9th ed. Hoboken, NJ: John Wiley & Sons.

Muttray, M. and J. S. Reedijk (2008). “Design of Concrete Armour Layers”. In: *Hansa International Maritime Journal*. Available via xbloc.com. URL: https://www.xbloc.com/sites/bamc/files/2022-04/xbloc-2008-design-of-concrete-armour-layers-muttray-et-al_0.pdf.

Pardo, V, J Molines, and JR Medina (2010). “Experimental analysis of the influence of armor unit placement method on armor porosity”. In: *Proc. 3rd International Conference on the Application of Physical Modelling to Port and Coastal Protection*, pp. 25–1.

Pardo, Vicente, Maria Herrera, Jorge Molines, and Josep Medina (2012). “Placement grids, porosity and randomness of armor layers”. In: *Coastal Engineering Proceedings* 1. DOI: 10.9753/icce.v33.structures.37.

Pardo, Vicente, Maria Piedad Herrera, Jorge Molines, and Josep R. Medina (2014). “Placement tests, porosity and randomness of cube and Cubipod armor layer”. In: *Journal of Waterway, Port, Coastal and Ocean Engineering* 140.5. DOI: 10.1061/(ASCE)WW.1943-5460.0000245.

Reedijk, Bas, Markus Muttray, Arnoud Van den Berge, and Richard De Rover (2008). “EFFECT OF CORE PERMEABILITY ON ARMOUR LAYER STABILITY”. In: *Coastal Engineering 2008*, pp. 3358–3367. DOI: 10.1142/9789814277426_0278. eprint: https://www.worldscientific.com/doi/pdf/10.1142/9789814277426_0278. URL: https://www.worldscientific.com/doi/abs/10.1142/9789814277426_0278.

Rijkswaterstaat (2023). *Havendam IJmuiden: Evaluatie Proefperiode en Advies voor de Toekomst*. Tech. rep. Version 2.1. The Netherlands: Rijkswaterstaat, Ministerie van Infrastructuur en Waterstaat.

Rijkswaterstaat (2024). *About Us: Mission and Strategy*. Ministry of Infrastructure and Water Management. URL: https://www.rijkswaterstaat.nl/en/about-us (visited on 02/15/2024).

Ruijter, D. (May 13, 2026). "The Effect of Filters on Impermeable Breakwaters: A Study into Stability of a Single Layer Armour of Cubes Influenced by the Underlayer Thickness on Top of an Impermeable Sublayer Related to the IJmuiden Breakwater". MSc thesis. Delft, the Netherlands: Delft University of Technology.

Sande, José, Enrique Peña González, and Enrique maciñeira (2016). "Damage criteria in roundheads with a single layer of Cubipod armor units". In: *Coastal Engineering Proceedings*. DOI: 10.9753/icce.v35.structures.13.

U.S. Army Corps of Engineers (2006). *Coastal Engineering Manual, Part VI: Design of Coastal Project Elements*. EM 1110-2-1100. Part VI of six, change 4 (2011). U.S. Army Corps of Engineers. Washington, D.C.

Van den Berg, Stefan, Rolf Bruins, Arnaud Casteleijn, Niek Leguit, and Peter Brand (2024). "Repair Optimization and Performance Analysis of the Asphalt Protection Layer of the Southern Breakwater in Front of the Port of Amsterdam". In: Paper 306, pp. 1–17.

Van der Meer, Jentsje W. (1988). "Rock Slopes and Gravel Beaches under Wave Attack". PhD thesis. Delft, The Netherlands: Delft University of Technology. URL: https://resolver.tudelft.nl/uuid:67e5692c-0905-4ddd-8487-37fdda9af6b4.

— (2021). "Rock Armour Slope Stability under Wave Attack; the Van der Meer Formula revisited". In: *Journal of Coastal and Hydraulic Structures* 1, p. 8. DOI: 10.48438/jchs.2021.0008.

Van Gent, Marcel R. A., Andrew Smale, and Coen Kuiper (2003). "Stability of Rock Slopes with Shallow Foreshores". In: *Proceedings of Coastal Structures 2003*. Portland, USA: ASCE. DOI: 10.1061/40733(147)9.

Van Gent, Marcel R. A., G. B. H. Spaan, S. E. Plate, E. Berendsen, Jentsje W. Van der Meer, and K. d'Angremond (2000). "Single-Layer Rubble Mound Breakwaters". In: *Proceedings of Coastal Structures '99, Santander, Spain*. Ed. by Iñigo J. Losada. Vol. 1. Rotterdam: Balkema, pp. 231–239.

Van Buchem, R. V. (2009). "Stability of a Single Top Layer of Cubes". MSc thesis. Delft, the Netherlands: Delft University of Technology. URL: https://repository.tudelft.nl/record/uuid:e32b33dc-7b64-4777-b32e-40f2c79e03a3.

Wenneker, Ivo and Bas Hofland (2014). "OPTIMAL WAVE GAUGE SPACINGS FOR SEPARATION OF INCOMING AND REFLECTED WAVES". In.

Wolters, G., M. R. A. Van Gent, N. W. H. Allsop, L. Hamm, and D. Mühlestein (2010). *HYDRALAB III: Guidelines for physical model testing of rubble mound breakwaters*. Deliverable NA3.1-2, EC contract no. 022441 (RII3). HYDRALAB III.

Zanuttigh, Barbara and Jentsje W. Van der Meer (2008). "Wave reflection from coastal structures in design conditions". In: *Coastal Engineering* 55.10, pp. 771–779. DOI: 10.1016/j.coastaleng.2008.02.009.

# Appendix A. Model configuration and drawings

## A.1. Cross-section and flume geometry

Figure A.1 shows the cross-section of the model in the wave flume, with the wave paddle on the left, the gauge array near the centre and the armoured slope at the right. The geometric symbols ($z_{\text{toe}}$, $z_{\text{plank}}$, $z_{\text{armour}}$, $h$, $h_{\text{toe}}$) are defined here and referenced in the per slope dimensions of table A.1.

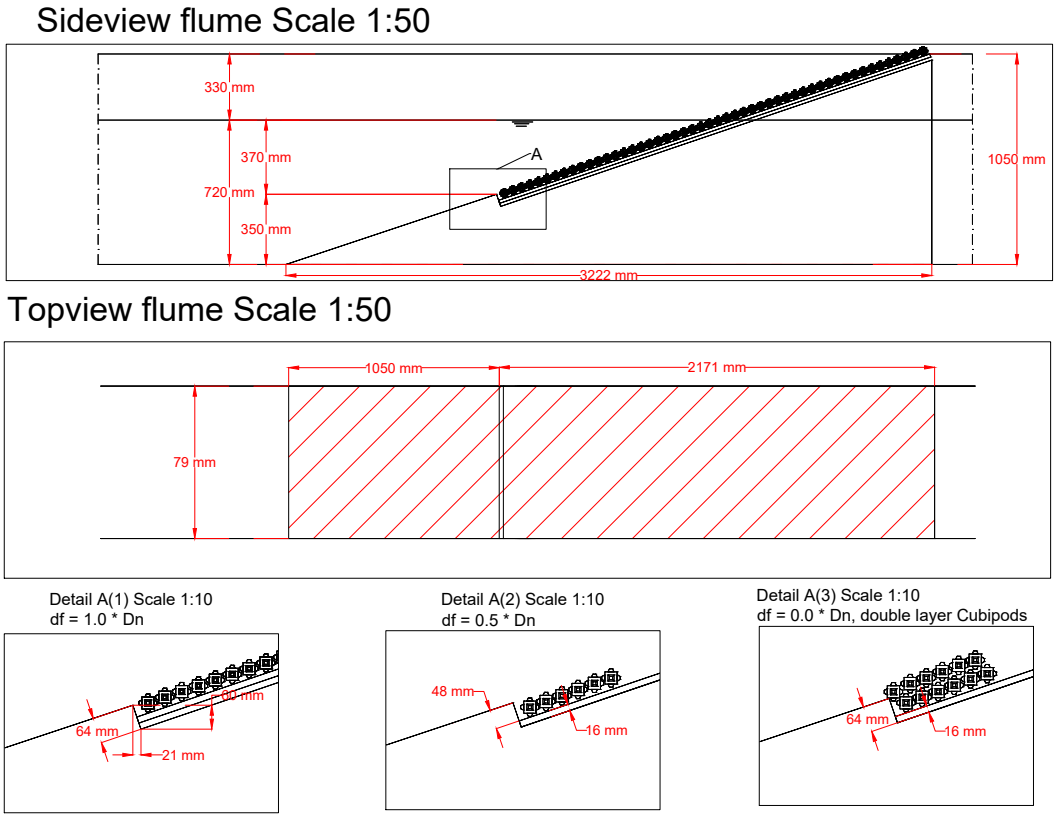


**Figure A.1:** Cross-section of the experimental setup in the wave flume. Geometric parameters per slope configuration are given in table A.1.

table A.1 summarises the as-built geometry for both slope configurations. The cot$\alpha = 2$ setup served the A1 and A2 test series. The cot$\alpha = 3$ setup served the A3, A4, C1, and B1 series.

**Table A.1:** As-built flume geometry per slope configuration. Elevations are measured from the flume floor. Slope length is the distance along the armoured face between the toe and the crest. Flume width $B = 0.79\,\text{m}$ for both configurations.

| Parameter | $\cot\alpha = 2$ | $\cot\alpha = 3$ |
|---|---|---|
| Water depth $h$ | 0.60 m | 0.65 m |
| Toe elevation $z_{\text{toe}}$ | 0.30 m | 0.40 m |
| Crest elevation $z_{\text{top}}$ | 0.92 m | 0.85 m |
| Water depth above toe $h_{\text{toe}}$ | 0.30 m | 0.25 m |
| Vertical armour rise | 0.62 m | 0.45 m |
| Horizontal armour run | 1.24 m | 1.35 m |
| Slope length (face) | $\sim$1.39 m | $\sim$1.43 m |
| Number of rows | 40–41 | 41 |
| Freeboard $R_c = z_{\text{top}} - h$ | 0.32 m | 0.20 m |

### A.1.1. Setup evolution

The $\cot\alpha = 3$ setup deviates from the $\cot\alpha = 2$ setup in three respects. These changes were introduced after the $\cot\alpha = 2$ series was completed and before construction of the $\cot\alpha = 3$ slope.

The toe elevation was raised from 0.30 m to 0.40 m. The original plan was to use 0.35 m for the gentler slope to leave more vertical space for the armour, but this was revised to 0.40 m to reduce the row count. The water depth was raised from 0.60 to 0.65 m, restoring the water depth above the toe to a value that allows the full target range of $H_{m0}$ without toe interference and preserves a deep-water condition at the paddle. The crest elevation was lowered from 0.92 to 0.85 m, reducing the vertical armour rise to 0.45 m and the number of armour rows to 41.

The motivation for the row reduction is operational. On the $\cot\alpha = 2$ slope, units in the upper rows shifted downslope during the compaction run, opening gaps in the crest region. With 40 rows on the $\cot\alpha = 2$ slope, a net downslope shift of 1 mm per row already produces a 4 cm gap at the top of the armour, larger than $D_n$ and large enough to require manual repair before the test could continue. A $\cot\alpha = 3$ slope built with the same vertical rise of 0.62 m would require approximately 60 rows, scaling the compaction gap to roughly 6 cm. Reducing the vertical rise to 0.45 m on the gentler slope keeps the row count comparable to the $\cot\alpha = 2$ case and the compaction gap manageable.

## A.2. Armour unit specifications

**Table A.2:** Physical properties of the Cubipod armour units used in this study.

| Parameter | Symbol | Value |
|---|---|---|
| Nominal diameter | $D_n$ | 32.4 mm |
| Cube body side | $L$ | 30.5 mm |
| Unit volume | $V$ | 34.0 cm$^3$ |
| Unit mass | $M$ | 78 g |
| Mass density | $\rho_s$ | 2300 kg/m$^3$ |
| Buoyant relative density | $\Delta$ | 1.30 |

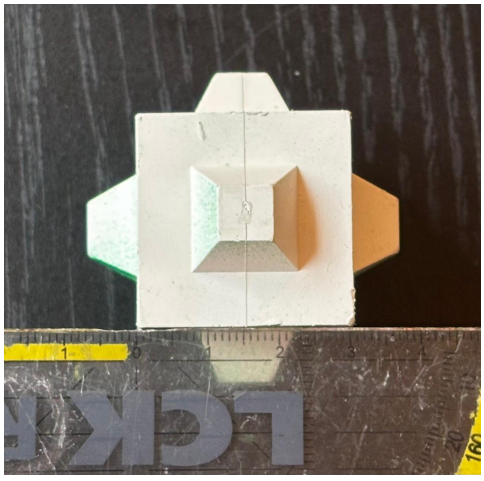

**Figure A.2:** Cubipod armour unit used in this study next to a scale reference ($D_n = 32.4\,\text{mm}$).

# A.3. Armour layer placement grid

## A.3.1. Grid geometry and porosity

The diamond placement grid (see figure 3.6) is defined by two spacings: $a$, the within-row distance between adjacent unit centres (parallel to the crest), and $b_{\text{slope}}$, the distance between row centres measured along the slope face. The corresponding horizontal projection of the row spacing is $b_{\text{horiz}} = b_{\text{slope}} \cos\alpha$, which is the convention used by the Cubipod Manual (Medina and Gómez-Martín, 2016). The placement porosity on the slope surface follows from the ratio of unit cross-section to grid cell area:

$$P = \left(1 - \frac{1}{(a/D_n)\,(b_{\text{slope}}/D_n)}\right) \times 100\,\% \tag{3.1}$$

Solving for the within-row spacing at a target porosity:

$$\frac{a}{D_n} = \frac{1}{(1 - P/100)\,(b_{\text{slope}}/D_n)} \tag{A.1}$$

## A.3.2. Crane versus hand placement

The Cubipod Manual (Medina and Gómez-Martín, 2016) recommends $a/D_n = 1.58$ to 1.61 for crane placement with subsequent wave compaction on a cot$\alpha = 1.5$ slope, targeting a measured as-built porosity of 40 to 42 %. Crane-placed units settle under wave action, so the as-built porosity is lower than the bare grid porosity. This settlement effect has been quantified by (Pardo et al., 2014):

$$P_{\text{real}} = (0.57\,P_{\text{grid}} + 13.8)\,\% \tag{A.2}$$

At the Manual's $a/D_n = 1.59$ with $b_{\text{slope}}/D_n = 1.22$: $P_{\text{grid}} = (1 - 1/(1.59 \times 1.22)) \times 100 = 48.5\,\%$, and equation (A.2) then gives $P_{\text{real}} = 41\,\%$, consistent with the Manual target.

In the present study, all units are placed by hand under dry conditions. No wave-induced settlement occurs between placement and the first wave step, so the as-built porosity is approximately equal to the grid porosity, and equation (A.2) does not apply. The placement target on the slope surface is therefore the Manual's 40 to 42 % as-built range, applied directly through equation (3.1).

## A.3.3. Adopted standard grid

After early trials documented in section A.3.4, the following placement procedure was adopted as the standard for all A1, A2, A3, A4, and B1 tests:

- Within a row: 15 and 16 units alternating per row, giving a constant within-row spacing $a = 49.7$ mm ($a/D_n = 1.53$). This corresponds to $a/D_n$ slightly below the Manual's crane-placement recommendation but is necessary to match the as-built porosity target without crane settlement.
- Between rows: each row is placed flush against the row below, with adjacent units physically touching the units of the preceding row. The row spacing $b_{\text{slope}}$ is therefore not a controlled design parameter but emerges from the geometry of the placement.

The measured $b_{\text{slope}}$ across all standard-grid tests ranges from 34.4 to 36.1 mm (mean 35.5 mm), corresponding to $b_{\text{slope}}/D_n = 1.06$ to 1.11 and $b_{\text{horiz}}/D_n = 1.01$ to 1.06 on cot$\alpha = 3$. The latter falls within the Manual's recommended $b_{\text{horiz}}/D_n = 1.02$ to 1.05 range.

The as-built grid is summarised in table A.3.

**Table A.3:** Placement-grid parameters of the standard procedure. Cube data refer to the C1 series. Double-layer data refer to B1. The Cubipod Manual reference row (Medina and Gómez-Martín, 2016) is the crane-placement target on cot$\alpha = 1.5$ with subsequent wave compaction.

| Configuration | $D_n$ [mm] | Units/row | $a$ [mm] | $b_{\text{slope}}$ [mm] | Porosity [%] |
|---|---|---|---|---|---|
| Cubipod, single, cot$\alpha = 2$ (A1, A2) | 32.4 | 15/16 alt. | 49.7 | 35.5 | 40.5 |
| Cubipod, single, cot$\alpha = 3$ (A3, A4) | 32.4 | 15/16 alt. | 49.7 | 35.1 | 40.0 |
| Cubipod, double, cot$\alpha = 3$ (B1) | 32.4 | 16 | 50.0 | 33.5 | 37.4 |
| Cube, single, cot$\alpha = 3$ (C1) | 31.0 | 19 | 41.8 | 31.1 | 25.0 |
| Manual reference (cot$\alpha = 1.5$, crane) | 32.4 | n.a. | 51.5 | 39.5 | 40.5 |

The mean as-built porosity across all single-layer Cubipod tests is 40.1 %. The Cubipod Manual reports stability results on cot$\alpha = 1.5$ at $n_v = 40.5\,\%$ (figure A.3). The difference of 0.4 percentage points is within the placement repeatability between tests (range 38.6 to 41.5 %), so the present results can be compared with the Manual figures without correction for porosity.

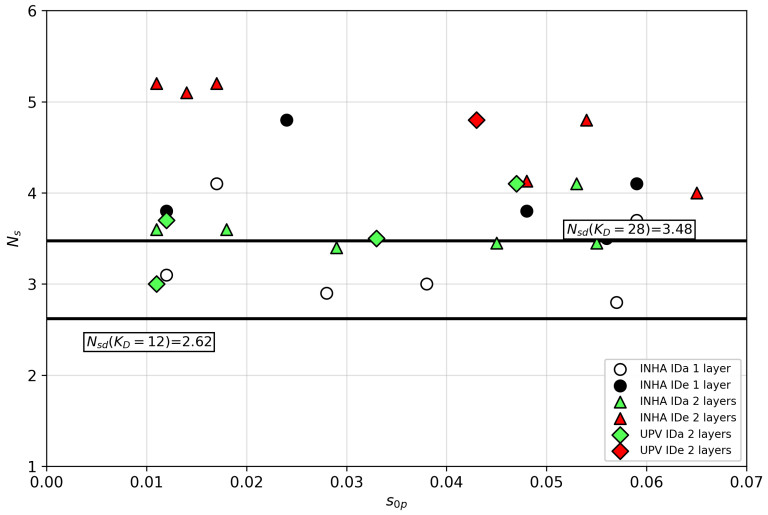


**Figure A.3:** Stability data from the Cubipod Manual (Medina and Gómez-Martín, 2016) at $n_v = 40.5\,\%$ porosity and cot$\alpha = 1.5$, plotting $N_s$ against the deep-water peak wave steepness $s_{0p}$ for single-layer and double-layer Cubipods. The mean as-built porosity in the present study is 40.1 %, allowing direct comparison.

## A.3.4. Trial grids

Two earlier placement variants were tested before the standard grid was adopted.

The first variant used $a = 46.76$ mm with 17 units per row, applied on the cot$\alpha = 2$ slope during the trial sessions A1_trial_wed and A1_trial_thu, and during the first attempt of A1_R1. This grid was abandoned because the within-row density was too high to allow the unit count of the alternating 15/16 scheme later adopted as standard.

The second variant followed the Cubipod manufacturer's recommendation given during a site visit by Antonio Corredor: $a \approx 49$ mm and a fixed $b_{\text{slope}} \approx 37$ mm, targeting a porosity of about 42 to 43 %. This combination was attempted in A1_R2. During the compaction run, the larger inter-row spacing left visible gaps between rows, the units did not interlock with the row below, and the underlayer started to fail before any wave step had reached the design target. The test was terminated during the compaction run. The standard procedure documented in section A.3.3, in which each row is placed flush against the row below, was adopted from A1_R3 onwards.

## A.3.5. Unit counts and porosity tolerance

Expected unit counts per configuration are given in table A.4, based on the standard placement geometry of table 3.5. The acceptance criterion during placement is $\pm 2$ percentage points on as-built porosity, evaluated from the total unit count and the measured slope area. The slope is rebuilt if the count falls outside the acceptable range.

**Table A.4:** Unit counts per configuration. Flume width $B = 0.79$ m. Armoured face area follows from the slope length in table A.1. The cube and double-layer counts refer to a single test each in the present campaign.

| Configuration | Units/row | Rows | Total units (face) | Porosity range [%] |
|---|---|---|---|---|
| Cubipod, single, cot$\alpha = 2$ (A1, A2) | 15/16 alt. | 40–41 | 620–635 | 38.7–41.5 |
| Cubipod, single, cot$\alpha = 3$ (A3, A4) | 15/16 alt. | 41 | 636 | 38.6–40.7 |
| Cubipod, double, cot$\alpha = 3$ (B1) | 16 | 41 | 656/layer, 1312 total | 37.4 |
| Cube, single, cot$\alpha = 3$ (C1) | 19 | 46 | 874 | 25.0 |

# Appendix B. Test programme and conditions

## B.1. Performed tests

The experimental campaign comprises 24 tests spread across six configurations. Each test steps the wave height in 2 cm increments of target $H_{m0}$ from 8 cm (compaction) to 22 cm, with a damage assessment after each step (section 3.10). table B.1 summarises every test in chronological order, grouped by configuration. The reported damage number $N_{od}$ is the cumulative count at the end of the last completed step, normalised by the structure width ($N_{od} = N_d/(B/D_n)$).

**Table B.1:** Summary of performed tests. Steps run as 8 cm (0, compaction), 10 cm (1), 12 cm (2), 14 cm (3), 16 cm (4), 18 cm (5), 20 cm (6), 22 cm (7). $H_{m0,\max}$ refers to the target machine value of the last completed step. $N_{od,\text{final}}$ is the cumulative damage at the end of the last completed step. "n.a." indicates premature termination before damage counting was possible.

| Test ID | Date | Steps | $H_{m0,\max}$ [cm] | $N_{od,\text{final}}$ | Remark |
|---|---|---|---|---|---|
| *Configuration A1: cot$\alpha = 2$, single-layer Cubipod, $t_f/D_n = 0.5$* | | | | | |
| A1_trial_wed | 01-04-2026 | 0–2 | 14 | 0.123 | Trial, manufacturer grid, not in primary dataset |
| A1_trial_thu | 02-04-2026 | 0–4 | 16 | 0.123 | Trial, revised grid, not in primary dataset |
| A1_R1 | 07-04-2026 | 0–6 | 20 | n.a. | Complete failure of armour + underlayer at step 6 |
| A1_R2 | 08-04-2026 | 0 | 8 | n.a. | Discarded, underlayer failure during compaction |
| A1_R3 | 09-04-2026 | 0–4 | 16 | 0.287 | Valid |
| A1_R4 | 10-04-2026 | 0–4 | 16 | 0.163 | Valid |
| A1_R5 | 13-04-2026 | 0–4 | 16 | 0.204 | Valid |
| A1_R6 | 20-04-2026 | 0–4 | 16 | 0.041 | Valid, step 5 not run (time) |
| *Configuration A2: cot$\alpha = 2$, single-layer Cubipod, $t_f/D_n = 1.0$* | | | | | |
| A2_R1 | 14-04-2026 | 0–3 | 14 | 0.285 | Valid, terminated after extensive damage at step 3 |
| A2_R2 | 15-04-2026 | 0–4 | 16 | 0.203 | Valid, rocking sensors added (S4, S5) |
| A2_R3 | 16-04-2026 | 0–4 | 16 | 0.608 | Valid, sensor sync via DASYLab marker |
| A2_R4 | 17-04-2026 | 0–4 | 16 | 0.364 | Valid |
| *Configuration A3: cot$\alpha = 3$, single-layer Cubipod, $t_f/D_n = 0.5$* | | | | | |
| A3_R1 | 22-04-2026 | 0–4 | 16 | 2.038 | Valid, rapid damage at step 4, step 5 not run |
| A3_R2 | 23-04-2026 | 0–4 | 16 | 0.693 | Valid, step 4 stopped at $\sim$11 min |
| A3_R3 | 24-04-2026 | 0–3 | 14 | 0.611 | Valid, step 4 not run (rapid damage progression) |
| A3_R4 | 28-04-2026 | 0–4 | 16 | 0.693 | Valid, deliberate dense placement (lowest porosity, 0.386) |
| *Configuration A4: cot$\alpha = 3$, single-layer Cubipod, $t_f/D_n = 1.0$* | | | | | |
| A4_R1 | 29-04-2026 | 0–3 | 14 | 1.263 | Valid, rapid damage at step 3 |
| A4_R2 | 30-04-2026 | 0–3 | 14 | 1.752 | Valid, rapid damage at step 3 |
| A4_R3 | 01-05-2026 | 0–3 | 14 | 0.448 | Valid, milder than R1/R2 at same step |
| A4_R4 | 04-05-2026 | 0–4 | 16 | 1.019 | Valid, survived step 3, rapid at step 4 (higher porosity 0.403) |
| *Configuration C1: cot$\alpha = 3$, single-layer cube, $t_f/D_n = 1.0$* | | | | | |
| C1_R1 | 07-05-2026 | 0–2 | 12 | 1.287 | Valid, rapid IDe at step 2 (cubes, 31 mm) |
| C1_R2 | 08-05-2026 | 0–2 | 12 | 1.092 | Valid, rapid IDe at step 2 |
| C1_R3 | 11-05-2026 | 0–2 | 12 | 1.247 | Valid, rapid IDe at step 2 |
| *Configuration B1: cot$\alpha = 3$, double-layer Cubipod, $t_f/D_n = 0.5$* | | | | | |
| B1_R1 | 12-05-2026 | 0–7 | 22 | 26.91 | Pilot, full programme. Top layer collapsed at steps 6–7, bottom layer intact (5 extractions at step 7) |

The C1 series uses precast concrete cubes ($D_n = 31$ mm, $\rho_s = 2240$ kg/m$^3$) instead of Cubipods. All other configurations use single-layer Cubipods ($D_n = 32.4$ mm, $\rho_s = 2300$ kg/m$^3$) except B1, which

uses double-layer Cubipods. Slope length, placement grid, and as-built porosity per test are recorded in the damage log (`data/damage_log.csv`).

## B.2. Pre-test stability predictions

Before the campaign the wave-height range, the candidate unit sizes, and the flume-capacity check were set from a pre-test stability prediction. The prediction extrapolated the $1{:}1.5$ Cubipod Manual *laboratory* stability data (Medina and Gómez-Martín, 2016) to the $1{:}2$ and $1{:}3$ slopes using Hudson scaling, $N_{s,\text{new}} = N_{s,\text{ref}} \left(\cot \alpha_{\text{new}} / \cot \alpha_{\text{ref}}\right)^{1/3}$. These are laboratory stability numbers $N_s$, not design values $N_{sd}$: only the slope factor of the Hudson relation is applied to the Manual lab data, and no safety factor is introduced. This gave $N_s$ ranges of approximately 3 to 6 for the $1{:}2$ slope and 3 to 7 for the $1{:}3$ slope (figure B.1), and placed IDa at $N_s \approx 2.88$ on $\cot \alpha = 2$ and $N_s \approx 3.30$ on $\cot \alpha = 3$, with IDe approximately one step ($\Delta N_s \approx 0.5$) above the corresponding IDa. The flume capacity ($H_{m0,\max} \approx 0.22\,\text{m}$, at $D_n = 3.24\,\text{cm}$) yields $N_{s,\max} \approx 5.2$, sufficient to reach destruction for most configurations under the predicted curves. The measured stability (section 5.2) deviates from this Hudson-based extrapolation. The interpretation is given in chapter 6. The prediction is documented here because it set the rationale for the test programme, not because it describes the measured behaviour.

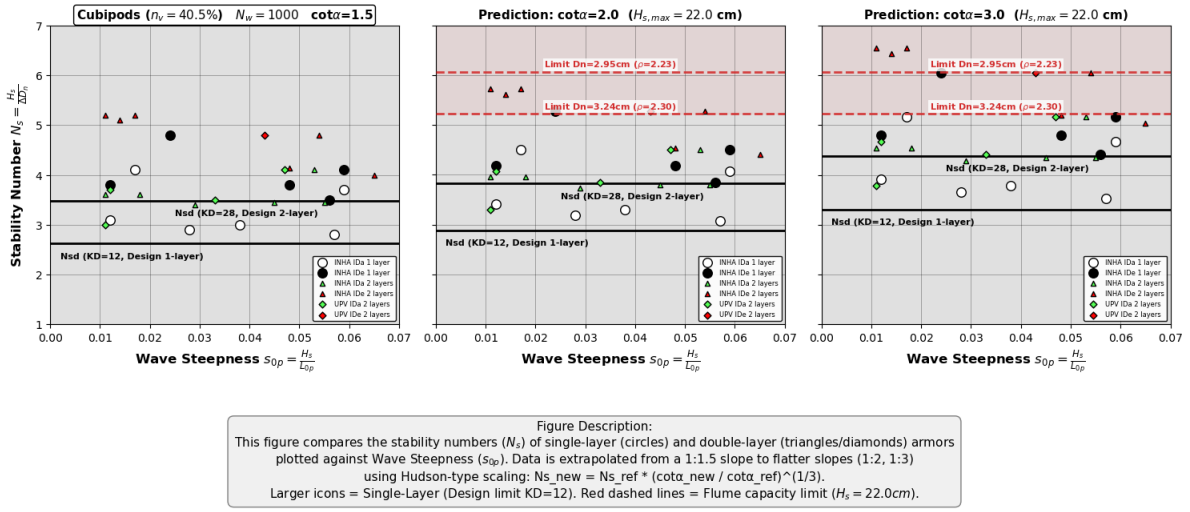


**Figure B.1:** Pre-test stability number predictions for $\cot \alpha = 2$ and $\cot \alpha = 3$, extrapolated from the $1{:}1.5$ Cubipod Manual data (Medina and Gómez-Martín, 2016) using Hudson scaling, $N_{s,\text{new}} = N_{s,\text{ref}} \left(\cot \alpha_{\text{new}} / \cot \alpha_{\text{ref}}\right)^{1/3}$. The leftmost panel shows the $1{:}1.5$ reference data and the other two panels the extrapolation. Stability number $N_s$ is plotted against wave steepness $s_{0p}$. Circles are single-layer placements and triangles and diamonds are double-layer placements, with larger markers for the single-layer data. The black horizontal lines are the Hudson design values for the single-layer ($K_D = 12$) and double-layer ($K_D = 28$) reference. The red dashed lines mark the flume capacity limit at the maximum wave height $H_s = 22$ cm for the two candidate unit sizes, $D_n = 2.95$ and $3.24$ cm. The actual measured values are reported in section 5.2.

## B.3. Wave field realisation

All tests use a single JONSWAP wave field realisation (seed 1). Applying the same seed at every $H_{m0}$ step across every test means the paddle command signal is identical between tests, so measured incident $H_{m0}$ values are directly comparable without correction for wave-field variability. Only one short pause occurred mid-run during the campaign (A3_R2 step 1, split into two $\sim$12 min segments). The realisation is otherwise continuous across the full run duration of each step.

## B.4. Wave-gauge calibration

Each gauge was calibrated once at the start of the test campaign by recording the mean voltage at seven submerged depths from 40 to 10 cm in 5 cm steps, with the water still. A linear fit $h = aV + b$ then gives the scale factor $a$ for each gauge, which is entered in DASYLab as the calibration coefficient. The three calibration lines are shown in figure B.2 and the fit parameters are listed in table B.2. All three gauges give $a$ within $0.5\,\%$ of each other and $R^2 > 0.9999$, so the linear-fit assumption holds well. The

calibration was redone once during the campaign, on 02-04-2026, after a wiring change that swapped two DASYLab channels.

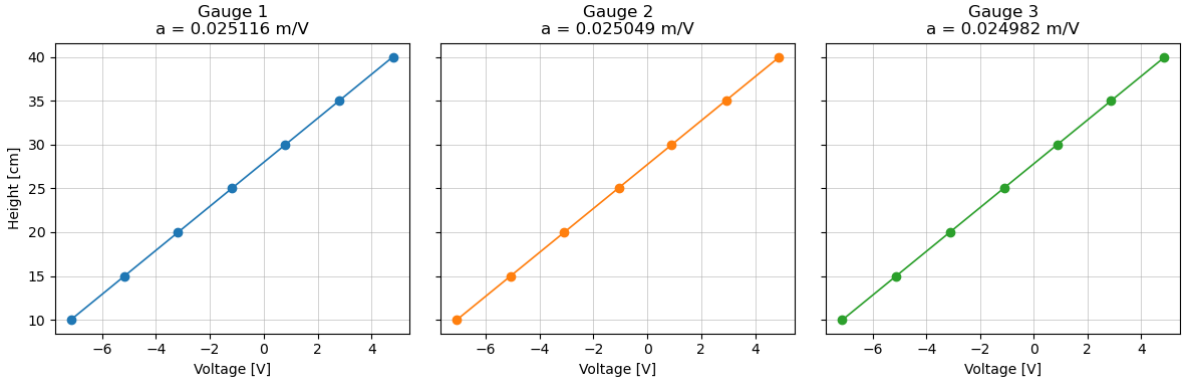


**Figure B.2:** Calibration lines for the three resistance-type wave gauges. Submerged height $h$ is plotted against mean DASYLab voltage $V$ at seven depths from 10 to 40 cm. The slope $a$ (in m/V) is used as the calibration coefficient in DASYLab.

**Table B.2:** Calibration fit parameters for the three wave gauges. The fit is $h = a\,V + b$, with $h$ in m and $V$ in V.

| Gauge | $a$ [m/V] | $b$ [m] | $R^2$ |
|---|---|---|---|
| 1 | 0.025116 | 0.279745 | 0.99998 |
| 2 | 0.025049 | 0.277124 | 0.99998 |
| 3 | 0.024982 | 0.278087 | 0.99999 |

## B.5. Target and measured wave parameters

tables B.3 and B.4 list the target machine settings and the mean measured incident wave parameters per step, separated by slope angle. The incident $H_{m0,\text{inc}}$ is separated from the reflected signal using the three-gauge method of (Mansard and Funke, 1980) and averaged across all valid repetitions of each configuration on that slope. The peak period $T_p$ is the spectral peak measured at the array, and $K_r$ is the corresponding reflection coefficient.

The wave generation was set to a fixed spectral steepness $s_{m-1,0} = H_{m0}/(gT_{m-1,0}^2/2\pi) = 0.040$, based on the spectral period $T_{m-1,0}$ and the deep-water dispersion relation. This is the period that was held to a constant steepness, and it matches the recommendation of Van der Meer (2021) for the intermediate water depths used here. For JONSWAP with $\gamma = 3.3$ the peak period follows as $T_p \approx 1.1\,T_{m-1,0}$, so the steepness based on $T_p$ is lower and varies slightly between realisations.

The realized incident steepness is below the target. The wave paddle sits roughly $32$ m from the structure toe. Over that distance the wall and floor drag take energy out of the waves, so the height at the gauge array is lower than the paddle setting. The peak period does not change, so $s = H_{m0}/L_0$ at the structure ends up below the target. Averaged over the $\cot\alpha = 2$ tests the realized value is $s_{m-1,0} = 0.034$, about $15\,\%$ below the $0.040$ target, with peak-period steepness $s_{op} = 2\pi H_{m0,\text{inc}}/(gT_p^2) = 0.030$. Three contributions lower it: the incident height after reflection separation is on average $11\,\%$ below the machine setting and $s \propto H_{m0}$, the realized periods are marginally longer, and at the highest steps depth-induced breaking occurred seaward of the structure, clipping the height reaching the toe. Over the steepness range covered here this has no measurable effect on stability: the Cubipod Manual steepness tests ($s_{0p} \approx 0.01$ to $0.06$) show the design stability to be essentially independent of steepness (Medina and Gómez-Martín, 2016).

**Table B.3:** Wave parameters per step for the cot$\alpha = 2$ slope (water depth $h = 0.60$ m). Target columns are the machine input values. Measured columns are the mean across configurations A1 and A2 (valid repetitions only).

| Step | $H_{m0,\text{target}}$ [cm] | $T_p$ [s] | $T_{m-1,0}$ [s] | $H_{m0,\text{inc}}$ [cm] | $T_{p,\text{meas}}$ [s] | $K_r$ |
|---|---|---|---|---|---|---|
| 0 (comp.) | 8.0 | 1.24 | 1.13 | 7.08 | 1.25 | 0.265 |
| 1 | 10.0 | 1.40 | 1.27 | 8.94 | 1.37 | 0.322 |
| 2 | 12.0 | 1.53 | 1.39 | 10.77 | 1.49 | 0.379 |
| 3 | 14.0 | 1.65 | 1.50 | 12.59 | 1.65 | 0.417 |
| 4 | 16.0 | 1.76 | 1.60 | 14.43 | 1.71 | 0.438 |
| 5[a] | 18.0 | 1.87 | 1.70 | 16.18 | 1.80 | 0.473 |
| 6[a] | 20.0 | 1.97 | 1.79 | 16.28 | 2.09 | 0.463 |

[a] Steps 5 and 6 from A1_R1 only ($n = 1$). At step 6 the structure collapsed. Reported values reflect the partial run before termination.

**Table B.4:** Wave parameters per step for the cot$\alpha = 3$ slope (water depth $h = 0.65$ m). Target columns are the machine input values. Measured columns are the mean across configurations A3, A4, C1, and B1 (valid repetitions only).

| Step | $H_{m0,\text{target}}$ [cm] | $T_p$ [s] | $T_{m-1,0}$ [s] | $H_{m0,\text{inc}}$ [cm] | $T_{p,\text{meas}}$ [s] | $K_r$ |
|---|---|---|---|---|---|---|
| 0 (comp.) | 8.0 | 1.24 | 1.13 | 7.30 | 1.24 | 0.176 |
| 1 | 10.0 | 1.40 | 1.27 | 9.28 | 1.36 | 0.193 |
| 2 | 12.0 | 1.53 | 1.39 | 11.17 | 1.51 | 0.227 |
| 3 | 14.0 | 1.65 | 1.50 | 13.14 | 1.65 | 0.249 |
| 4 | 16.0 | 1.76 | 1.60 | 15.06 | 1.76 | 0.268 |
| 5[a] | 18.0 | 1.87 | 1.70 | 17.10 | 1.89 | 0.260 |
| 6[a] | 20.0 | 1.97 | 1.79 | 18.87 | 1.88 | 0.271 |
| 7[a] | 22.0 | 2.07 | 1.88 | 19.50 | 2.00 | 0.330 |

[a] Steps 5–7 from B1_R1 only ($n = 1$, double-layer test).

Two patterns are visible across the two tables. First, the measured incident $H_{m0,\text{inc}}$ on the cot$\alpha = 3$ slope is consistently 3 to 5 % higher than on cot$\alpha = 2$ at the same step. This is consistent with the deeper flume water on the gentler slope ($h = 0.65$ vs $0.60$ m), giving slightly less shoaling-induced energy loss between paddle and toe. Second, $K_r$ on cot$\alpha = 3$ is approximately 0.10 to 0.18 below the corresponding value on cot$\alpha = 2$ at every step, as expected from the gentler slope geometry. A figure of $K_r$ versus $N_s$ for all configurations is shown in section 5.4.

## B.6. Reynolds numbers per step

The stability Reynolds number is computed as

$$Re = \frac{\sqrt{g\, H_{m0,\text{inc}}}\, D_n}{\nu} \tag{B.1}$$

with $g = 9.81$ m/s$^2$, the kinematic viscosity of fresh water at laboratory temperature $\nu = 1.0 \times 10^{-6}$ m$^2$/s, and the nominal armour size $D_n = 32.4$ mm (Cubipod) or 31 mm (cube). The Cubipod Manual recommends $Re > 3 \times 10^4$ to keep viscous scale effects below the resolution of typical damage counts (Medina and Gómez-Martín, 2016). Below this threshold, residual stability and the magnitude of small displacements may be overestimated relative to prototype scale.

table B.5 reports $Re$ per step for both slope geometries and both armour-unit sizes used in the campaign, based on the mean measured incident $H_{m0,\text{inc}}$ from tables B.3 and B.4.

**Table B.5:** Stability Reynolds number per step for the configurations tested. Cubipods were tested on both slopes, cubes only on cot$\alpha = 3$. The compaction step (step 0) lies below the $3 \times 10^4$ threshold. The principal damage range (step 2 and higher) sits above it for Cubipods and just above it for cubes. Steps not run for a given unit type are left blank.

| Step | $H_{m0,\text{target}}$ [cm] | Cubipod ($D_n = 32.4$ mm) | | Cube ($D_n = 31$ mm) |
|---|---|---|---|---|
| | | cot$\alpha = 2$ | cot$\alpha = 3$ | cot$\alpha = 3$ |
| 0 (comp.) | 8 | 27 000 | 27 400 | 26 200 |
| 1 | 10 | 30 300 | 30 900 | 29 500 |
| 2 | 12 | 33 300 | 33 900 | 32 400 |
| 3 | 14 | 36 000 | 36 800 | |
| 4 | 16 | 38 500 | 39 400 | |
| 5 | 18 | 40 800 | 42 000 | |
| 6 | 20 | 40 900 | 44 100 | |
| 7 | 22 | | 44 800 | |

The cube series (C1) only reaches step 2 before rapid damage, so its operational $Re$ range is $26\,200$ to $32\,400$. The Cubipod series exceeds the $3 \times 10^4$ recommendation from step 1 onwards on both slopes. The compaction step lies just below the threshold. No damage statistics are derived from compaction data, so this does not affect the headline stability results.

## B.7. Data organisation

table B.6 lists the data produced per test step.

**Table B.6:** Data output per test step.

| Source | Format | Rate | Content |
|---|---|---|---|
| Wave gauges | `.ASC` (DASYLab) | 100 Hz | 3-channel surface elevation time series |
| Rocking sensors | `.csv` on microSD | 100 Hz | Angular velocity and acceleration per instrumented unit |
| Camera | `.jpg` / `.mp4` | per step / continuous | Top-view photographs for $N_{od}$ assessment and side-view video for failure mechanisms |
| Wave generator | paddle command (DASYLab log) | per step | $H_{m0}$, $T_p$, JONSWAP spectrum parameters |

Raw data are stored under `data/raw/<test_id>/`, one folder per repetition. Each folder contains the DASYLab `.ASC` file for that repetition (all wave-height steps in a single recording), plus subfolders `photos/`, `video/`, and `rocking/`. Processed wave parameters for all configurations are collected in `data/processed/wave_params.csv`, with one row per configuration and step combination. Damage counts per step are recorded in `data/damage_log.csv`.

# Appendix C. Rocking sensor design and development

This appendix documents the hardware construction, moment-of-inertia calibration, firmware architecture, and time-synchronisation of the embedded rocking sensors. The measurement methodology is described in section 4.2.

## C.1. Hardware and 3D-printed shell

The instrumented Cubipod units consist of a 3D-printed hollow shell containing a TinyCircuits electronics stack, a 290 mAh LiPo battery, and lead ballast. The outer geometry follows the nominal Cubipod dimensions ($D_n = 32.4$ mm). The CAD model is shown in figure C.1 and the build sequence in figure C.2.

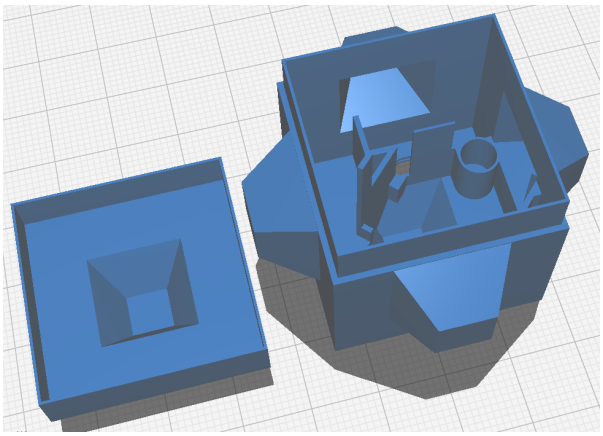

**Figure C.1:** 3D model of the instrumented Cubipod shell as prepared for printing in Ultimaker Cura. The internal cavity hosts the TinyCircuits stack, battery, reed switch, and lead ballast. The six extrusions provide the lead-ball cavities used in the moment-of-inertia calibration (section C.2).

The shell is resin-cast with a wall thickness of 1.2 mm and sealed with epoxy. The electronics stack comprises a TinyZero processor (ASM2021), a 9-axis IMU shield (ASD2511), and a MicroSD shield (ASD2201), shown individually in figure C.3. A reed switch in the battery supply line serves as a hardware power cutoff, activated by an external magnet. The wiring is given in figure C.4. This isolates the battery between test days and guarantees clean SD-card shutdown without reopening the sealed shell. The battery capacity is sufficient for continuous recording throughout a full test day.

Seven instrumented shells were constructed. Their as-built masses and operational status are listed in table C.1. Units 2 and 7 were lost or unfinished during construction. The remaining five units (1, 3, 4, 5, 6) were successfully deployed, with as-built masses within $\pm 2\,\%$ of the 78.0 g target.

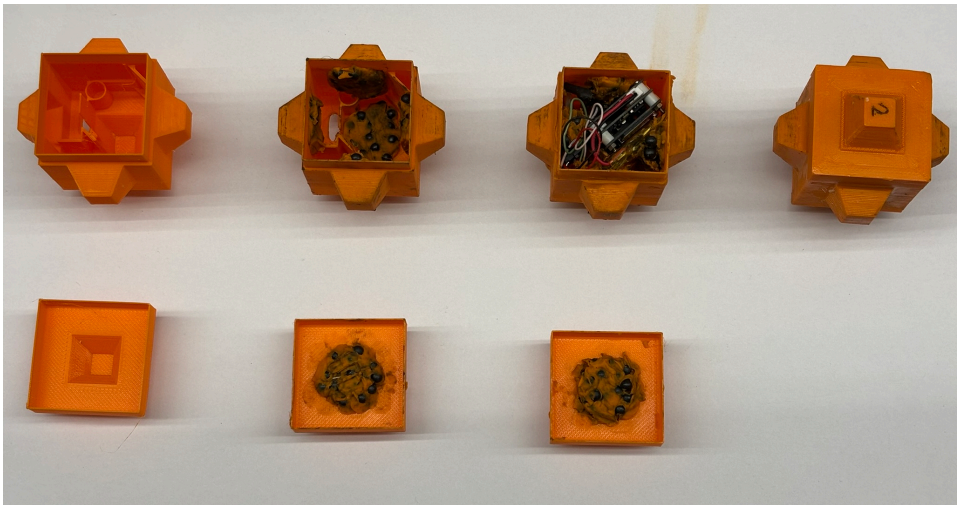

**Figure C.2:** Construction stages of the instrumented Cubipod (from left to right): empty 3D-printed shell, shell partially filled with plasticine and lead ballast, shell with plasticine, lead ballast, and the TinyCircuits electronics stack in place, and the fully assembled and sealed unit ready for deployment.

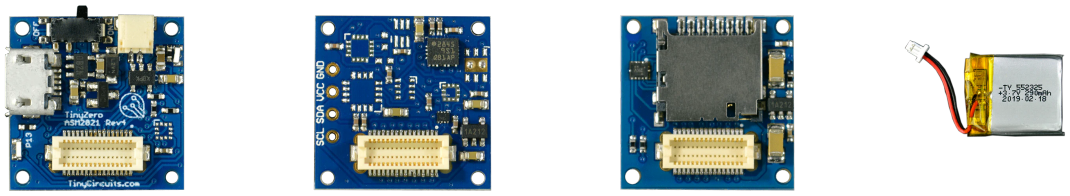

**(a)** TinyZero processor (ASM2021) **(b)** 9-axis IMU shield (ASD2511) **(c)** MicroSD shield (ASD2201) **(d)** 290 mAh LiPo battery

**Figure C.3:** Individual hardware components of the rocking sensor assembly. All boards are TinyCircuits standard modules.

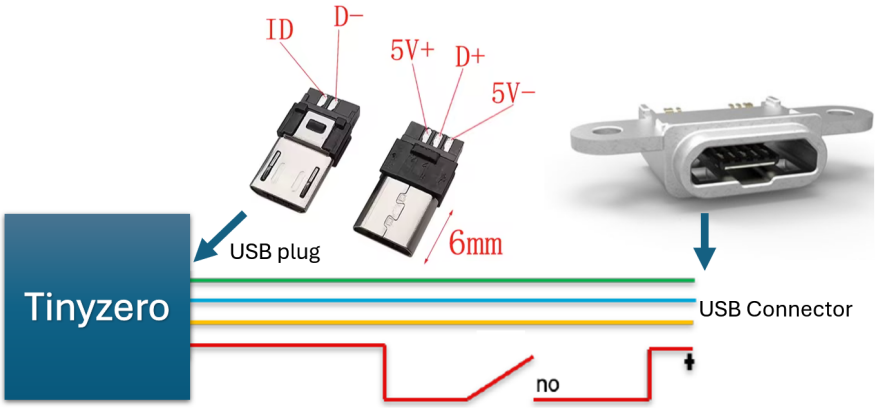


**Figure C.4:** Wiring of the rocking sensor electronics. The TinyZero stack (left) carries a male micro-USB plug whose four signal lines (5V+, 5V−, D+, D−) run to the waterproof IP67 panel-mount micro-USB connector (right) bonded into the shell wall. The reed switch interrupts the 5V+ rail and closes when a magnet is brought against the unit, connecting the battery and enabling recording.

**Table C.1:** As-built mass of each instrumented Cubipod unit and its operational status during the test programme. The target mass corresponds to the cast concrete reference Cubipod ($\rho_s = 2300\,\text{kg/m}^3$, $D_n = 32.4\,\text{mm}$).

| Unit ID | Mass [g] | Deviation [%] | Status |
|---|---|---|---|
| 1 | 77.73 | $-0.35$ | Deployed |
| 2 | n.a. | n.a. | Lost during construction |
| 3 | 77.39 | $-0.78$ | Deployed |
| 4 | 77.33 | $-0.86$ | Deployed |
| 5 | 79.53 | $+1.96$ | Deployed |
| 6 | 78.43 | $+0.55$ | Deployed |
| 7 | n.a. | n.a. | No epoxy coating, not usable in flume |
| Target | 78.00 | 0.00 | Cast concrete Cubipod reference |

## C.2. Moment of inertia calibration

The moment of inertia of the instrumented unit must match the concrete Cubipod to ensure representative rocking dynamics. The deficit caused by the internal cavity is compensated by distributing lead balls in the six extrusion cavities at radius $r_{\text{extr}} = 16\,\text{mm}$.

The battery breaks the static symmetry. To restore static balance, the lead-ball count is adjusted: $n_s = 33$ balls in the four standard extrusions and $n_b = 31$ in the two battery-adjacent extrusions. The body-frame inertia along the rotation axis then satisfies the balance condition

$$I_c \;=\; I_{\text{fill}} + I_{\text{clay}} + I_{\text{batt}} + (3n_s + n_b)\, m_{\text{ball,net}}\, r_{\text{extr}}^2 \tag{C.1}$$

where $m_{\text{ball,net}}$ is the lead-ball mass net of the epoxy it displaces. The resulting per component mass and inertia budget is given in table C.2. The internal lead-ball layout is illustrated in figure C.5.

**Table C.2:** Mass and moment-of-inertia budget of the instrumented Cubipod (selected configuration, lead-ball radius $r_{\text{extr}} = 16\,\text{mm}$). The body-frame inertia $I_y$ is taken about the unit centre along the chosen rotation axis. $I_{\text{out}}$ is the parallel-axis-transferred inertia about the extrusion tip, $d_{\text{out}} = 3L/4 = 22.9\,\text{mm}$. Source: `cubipod_moi_calculation.ipynb`.

| Component | Mass [g] | $I_y$ [kg mm$^2$] |
|---|---|---|
| Concrete reference (78.0 g, scaled CAD) | 78.00 | 13.31 |
| Resin shell + electronics + epoxy fill | 41.50 | 7.08 |
| Battery, net of displaced epoxy | 1.85 | 0.05 |
| Plasticine bedding, net ($6 \times 1.5\,\text{g}$) | 2.65 | 0.45 |
| Lead, 4 standard extrusions ($n_s = 33$) | 21.76 | 4.18 |
| Lead, 2 battery-adjacent extrusions ($n_b = 31$) | 10.22 | 1.31 |
| Assembled total (instrumented unit) | 77.98 | 13.07 |
| Match relative to concrete reference | 100.0 % | 98.2 % |
| $I_{\text{out}}$ match (pivot at extrusion tip) | n.a. | 99.5 % |

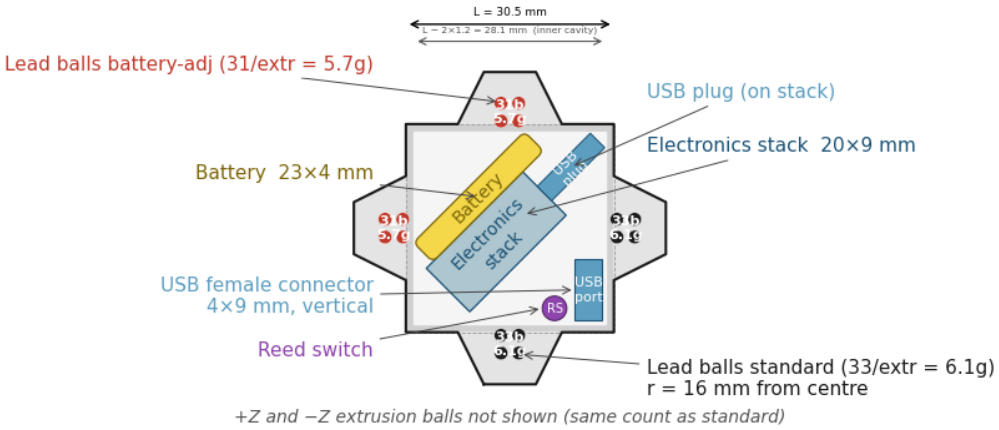


**Figure C.5:** Internal layout of the instrumented Cubipod (cross-section through the cube mid-height). The electronics stack sits diagonally inside the cube cavity, with the USB plug at the upper-right end. The LiPo battery is fixed against the $+Y/-X$ corner. The reed switch sits adjacent to the USB female connector. Lead-ball clusters occupy the four extrusion cavities visible in this section, with the two battery-adjacent extrusions holding two fewer balls than the standard extrusions to restore static balance about the rotation axis. The $+Z$ and $-Z$ extrusions (not shown) carry the same ball count as the standard extrusions.

The selected configuration gives an assembled mass of 77.98 g (100.0 % match to the 78.0 g target) and a body-frame inertia $I_y = 13.07\,\mathrm{kg\,mm^2}$ (98.2 % match to the $13.31\,\mathrm{kg\,mm^2}$ reference). The match is practically exact (99.5 %) once the parallel-axis transfer to the rocking pivot at the extrusion tip is included.

## C.3. Firmware architecture and reliability

The sensor firmware is written in C++ (Arduino framework, built with PlatformIO) for the TinyZero board. The predecessor used two separate Arduino programs, one for recording and one for reading the SD card, so the sensor had to be re-flashed each time it switched between the two (Caldera, 2019; Hofland et al., 2023). The firmware here does both in a single program. A short command sent over USB switches the sensor between recording and sending its stored file back to the computer, so no re-flashing is needed. It also adds a per sensor identifier and a more reliable way of saving data to the SD card, described below.

The predecessor sketch lost data when the SD card was slow to accept new readings. While the card was busy, fresh sensor samples kept arriving with nowhere to go, so some were dropped. The new firmware avoids this in three ways:

- A fast connection to the SD card, so each save finishes quickly and the card is rarely busy for long.
- A small block of memory that holds about five seconds of recent readings. If the card is briefly busy, new samples wait here instead of being lost.
- Saving at the right moment. The sensor keeps reading at full speed while a wave hits, and writes the collected data to the card in the calmer gaps between waves, when there is time to spare.

Zero firmware-induced data loss was recorded on 13 instrumented runs across all 5 active sensors during the campaign.

Recording and readout are controlled from Python notebooks rather than by hand. The readout notebook downloads each sensor's file over USB, saves it directly into the correct test folder under a structured name, and adds an absolute clock time to every sample from the session-start marker. Before the card is cleared it checks the data by comparing the number of samples the firmware reports against the number actually received, so a missing or interrupted run is flagged and the card is not erased when a download looks incomplete.

## C.4. Time synchronisation and crystal drift

Accurate timestamps are required to match sensor logs with the wave-gauge record. The TinyZero real-time clock relies on an internal RC oscillator without a precision crystal. This induces measurable clock drift.

Drift is corrected post-test using an affine transformation between two synchronisation markers (initial and final). Markers are generated by sharply shaking the active sensor in front of a camera before and after submersion. The internal clock time and the wave-gauge time (visible on camera) establish fixed anchors. The mean per sensor drift over five testdays is given in table C.3. An example of the per session fit is shown in figure C.6 with the start- and end-pair zooms in figure C.7. Drift varied from $+200$ to $+1190$ ppm depending on the unit but stayed consistent and linear during operation, so the affine correction fully compensated it over the run-time durations.

**Table C.3:** Mean per sensor clock drift relative to DASYLab over five testdays (ppm).

| Sensor | Mean drift [ppm] |
|---|---|
| 1 | $\sim 800$ |
| 3 | $\sim 520$ |
| 4 | $\sim 200$ |
| 5 | $\sim 1190$ |
| 6 | $\sim 310$ |

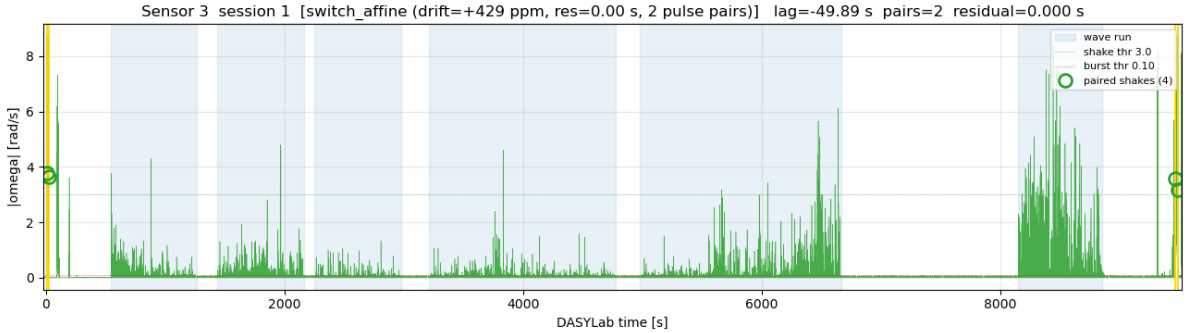


**Figure C.6:** Time-synchronisation overview for sensor 3, session 1 of test A4_R1. Green: $|\omega|$ trace at $100$ Hz, with the rocking detection threshold (red dashed) and the shake threshold (green dashed). Blue bands: wave-run windows from the DASYLab record. Yellow bands: switch ON windows. Green circles: paired-shake centroids that anchor the affine sync. The fit gives a per session drift of $+429$ ppm and a two-pair residual of zero by construction.

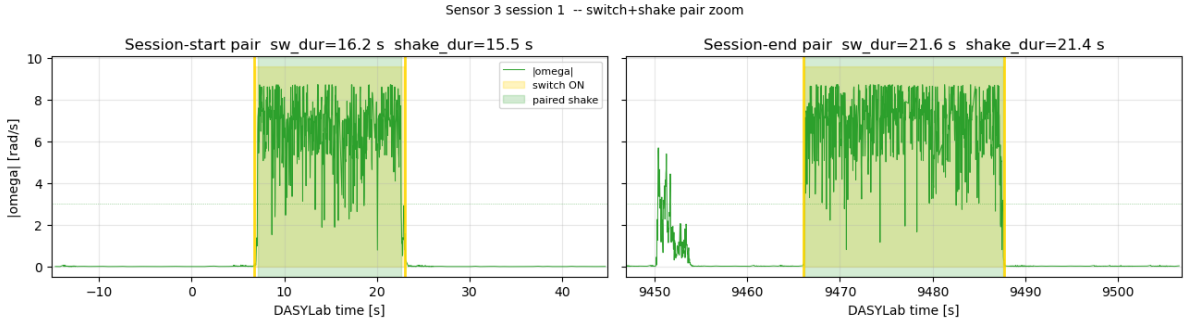


**Figure C.7:** Zoom on the start (left) and end (right) switch-plus-shake pair for the same session as figure C.6. The switch ON window (yellow) and the paired shake (green) overlap to within about one second. The shake $|\omega|$ trace reaches values well above the $3$ rad/s shake threshold (grey dotted line). The midpoint of the shake gives the time anchor on both the sensor axis and the DASYLab axis.

# Appendix D. Extended rocking-sensor results

This appendix provides the rocking-sensor figures and supporting comparisons referenced in section 5.3.3. These details extend the main results: the correlation between rocking activity and damage, the comparison with the Xbloc reference curves, the visual-detection threshold context, the per axis breakdown of the rocking signature, and the per test raw sensor traces.

## D.1. Rocking activity versus damage

Figure D.1 correlates the rocking signal directly to the measured damage per slope, with the initial settling-in compaction step excluded.

The left panel plots the per run average rocking rate (events per 1000 waves) against the per run damage rate ($N_d$ per 1000 waves). The rank correlation (Spearman $\rho$) is robust on the $1{:}3$ slope ($\rho = 0.58$, $p = 5 \times 10^{-4}$), demonstrating that increased rocking tracks damage progression. On the $1{:}2$ slope, there is no significant correlation ($\rho = 0.29$). The armour layer does not fail, yet rocking continues.

The right panel compares cumulative rocking events against cumulative damage ($N_{od}$). The trend persists strongly on the $1{:}3$ slope ($\rho = 0.69$) while decoupling on the $1{:}2$ slope. Rocking serves as a structural-level indicator of impending failure on flatter slopes, but not as a reliable per unit alarm for immediate displacement.

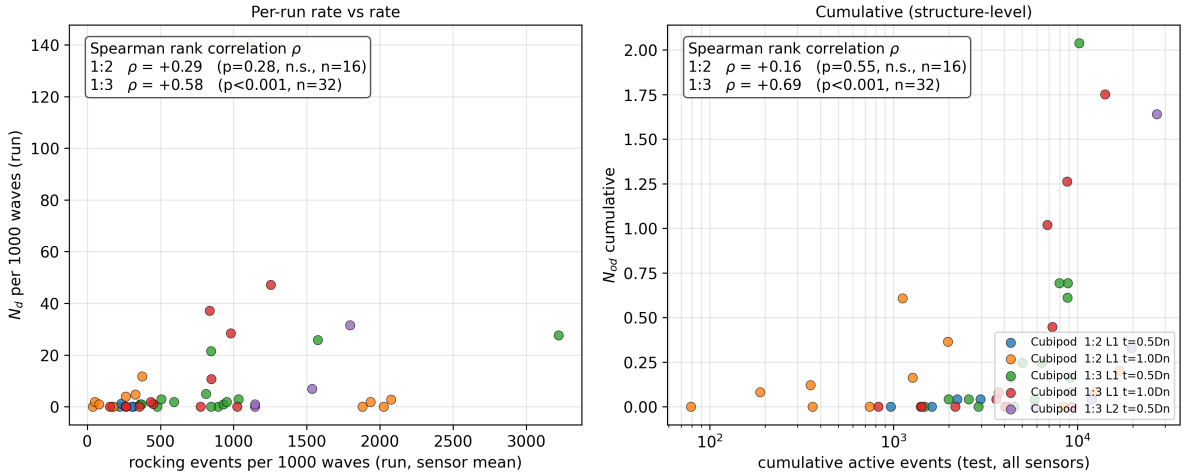


**Figure D.1:** Correlation between measured rocking activity and measured damage. Left: per run event rate versus per run damage rate. Right: cumulative events versus cumulative $N_{od}$. The rank correlation ($\rho$) is strong and significant on the $1{:}3$ slope but absent on the $1{:}2$ slope, where units rock continuously without displacement. The initial compaction step is excluded.

## D.2. Per slope rocking magnitudes

Aggregating all Cubipod stability events by slope angle gives the comparison in table D.1. The 1:3 slope rocks both more frequently ($+40\,\%$ per sensor per 1000 waves) and far more intensely than the 1:2 slope, with peak rotation rates about four times higher and rotation amplitudes about eight times higher.

**Table D.1:** Per slope rocking magnitudes for Cubipod configurations. Compaction step and post-extraction events excluded. Rates and amplitudes are normalised per sensor per 1000 waves and per event respectively, so they are directly comparable across tests despite different sensor counts and run durations.

| Metric | 1:2 slope | 1:3 slope | ratio |
|---|---|---|---|
| Mean event rate per sensor per 1000 waves | 612 | 843 | 1.4 |
| Mean per run max $\omega$ (rad/s) | 1.38 | 4.88 | 3.5 |
| $p_{99}$ per event $\omega$ (rad/s) | 0.94 | 4.38 | 4.7 |
| $p_{99}$ per event $d\theta$ (°) | 1.76 | 14.66 | 8.3 |

## D.3. Comparison with the Xbloc reference

(Hofland et al., 2023) provides the primary reference for single-layer embedded IMU dynamics using Xbloc. Figure D.2 presents the exceedance probability of peak angular velocity $\omega_s$ for the Cubipod tests, alongside Hofland's empirical design fit for Xbloc on a $1{:}1.5$ slope. The Cubipod on a $1{:}3$ slope displays systematically higher exceedance probabilities than the Xbloc fit, while the $1{:}2$ slope stays below it. The more cubic shape of the Cubipod provides less rotational redundancy compared to the long interlocking legs of the Xbloc, making it more prone to rocking under matched loads. The velocity is written in the Froude-scaled form $\omega^* = |\omega|_{\text{peak}}/\sqrt{g/D_n}$, which does not depend on model scale. At the same stability number and exceedance, the single-layer Cubipod on the $1{:}3$ slope rocks about $1.2$ to $1.8$ times faster than the Xbloc design fit. On the $1{:}2$ slope it rocks slower, at about half or less. The single double-layer test rocks harder still. The ratio is largest at low stability numbers and gets smaller in the extreme tail. The comparison uses Hofland's design fit, not his raw Xbloc data. The implications are discussed in section 6.4.2.

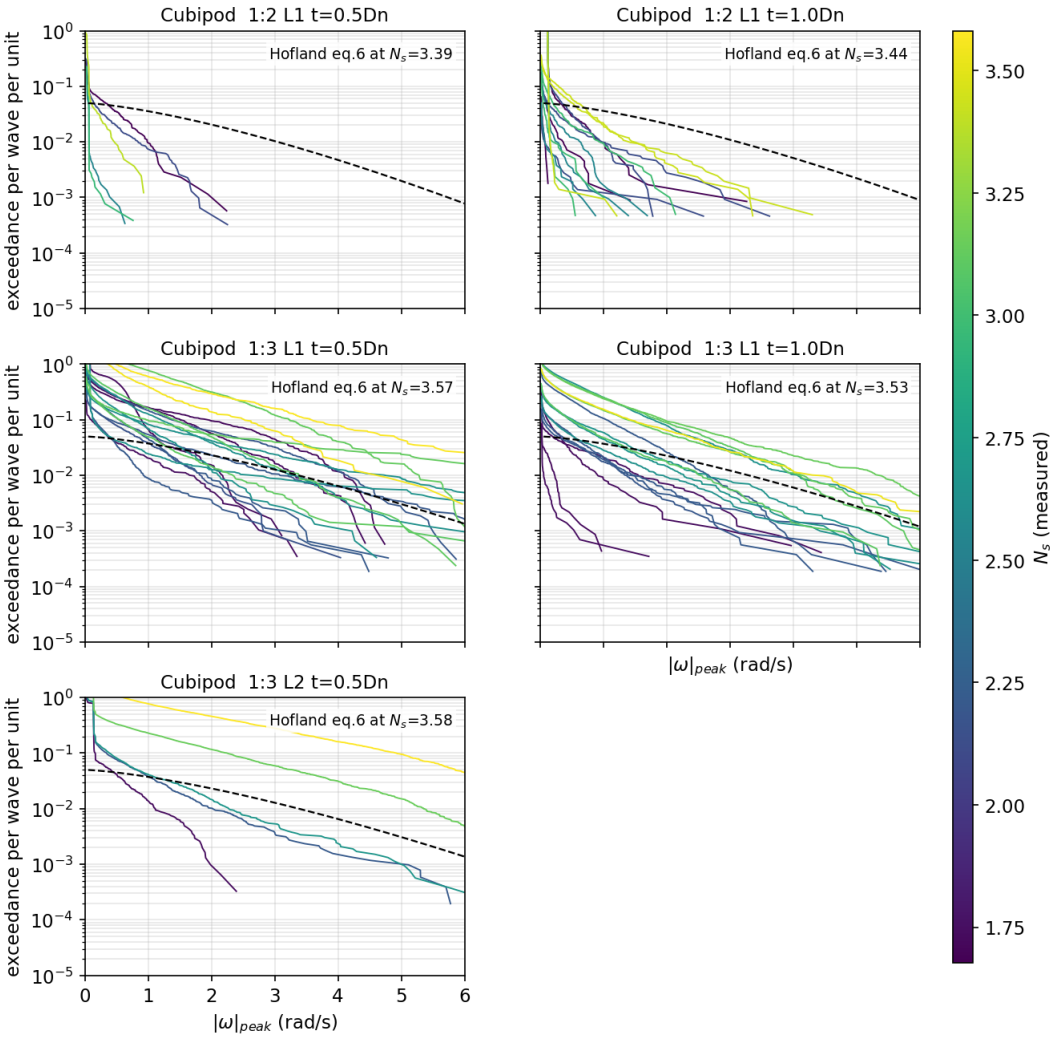


**Figure D.2:** Exceedance probability of peak angular velocity $\omega_s$ per wave, grouped by slope and underlayer thickness. The dashed grey line represents the empirical design fit for Xbloc (Hofland et al., 2023) at matched $N_s$. Rocking is more prevalent for Cubipods on gentler slopes than for Xblocs.

Figure D.3 evaluates directional symmetry. Events are separated into the first impact peak (corresponding to wave uprush) and the second peak (downrush). The overall least-squares correlation gives a slope of 0.92, indicating approximately symmetric rocking. In contrast, Hofland found a slope of 1.54 for Xblocs, meaning Xbloc primarily rocks during uprush. Cubipod's symmetric rocking profile reflects its more symmetrical geometry.

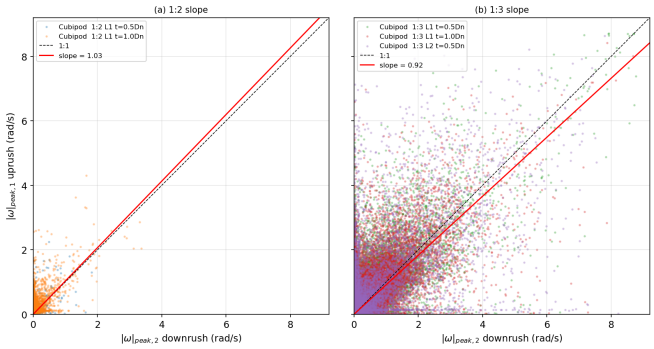


**Figure D.3:** Peak uprush angular velocity versus peak downrush angular velocity per rocking event. The least-squares slope of 0.92 indicates that Cubipods rock almost symmetrically in both directions.

## D.4. Visual versus instrumented detection

Visual detection during video analysis requires significant unit movement. A rotation of $5°$ is generally imperceptible under water, while $10°$ is noticeable. As figure D.4 shows, the fraction of instrumentally recorded events exceeding the $10°$ visual threshold is effectively zero on the $1{:}2$ slope and between about $1.5\,\%$ and $3.5\,\%$ on the $1{:}3$ slope. The majority of the rocking events recorded by the IMU are entirely invisible to camera-based observation.

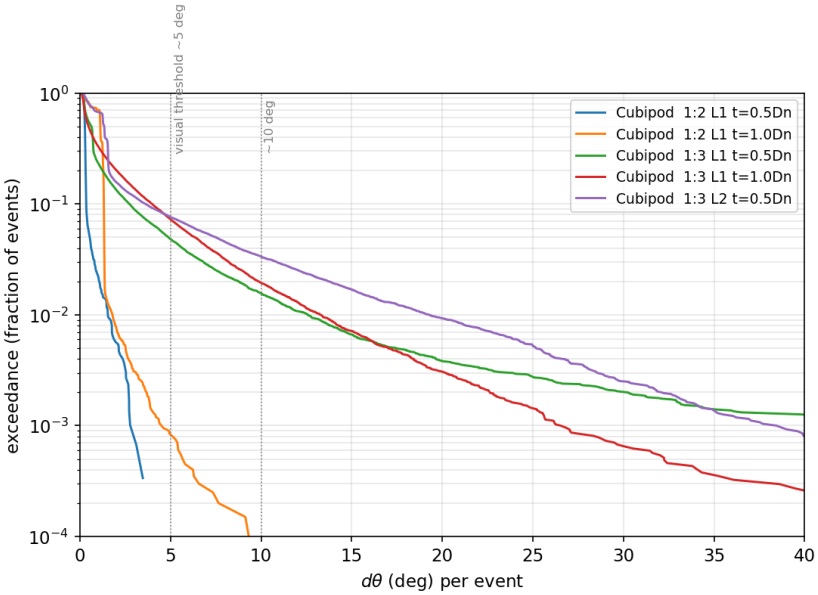


**Figure D.4:** Exceedance probability of the per event rotation amplitude $\Delta\theta$. Fewer than $4\,\%$ of measured rocking events exceed $10°$, making most rocking invisible to video-based observation.

## D.5. Per axis rocking signature

Figure D.5 shows the distribution of the dominant-axis ratio for all events. For approximately $65\,\%$ of recorded events, over $80\,\%$ of the total angular kinetic energy is concentrated along a single coordinate axis. The motion is effectively 1D planar rotation rather than 3D tumbling, validating the use of the single highest per axis peak velocity as a representative metric for structural impact computations.

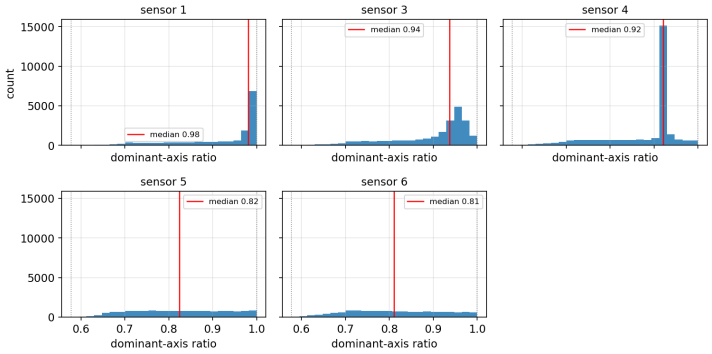


**Figure D.5:** Distribution of the dominant-axis energy fraction across all recorded events. Most events concentrate over $80\,\%$ of their rotational energy on a single axis, indicating primarily 1D planar rocking rather than complex 3D tumbling.

## D.6. Per test rocking traces

Figure D.6 presents the full raw time series of the measured peak angular velocity for all deployed sensors, arranged by configuration. Compaction stages (where high initial mobility frequently occurs) are clearly visible at the start of most tests. Black markers indicate extraction: events triggered by a sensor unit being structurally extracted from the armour layer. These post-extraction noise spikes are excluded from all quantitative aggregate analyses.

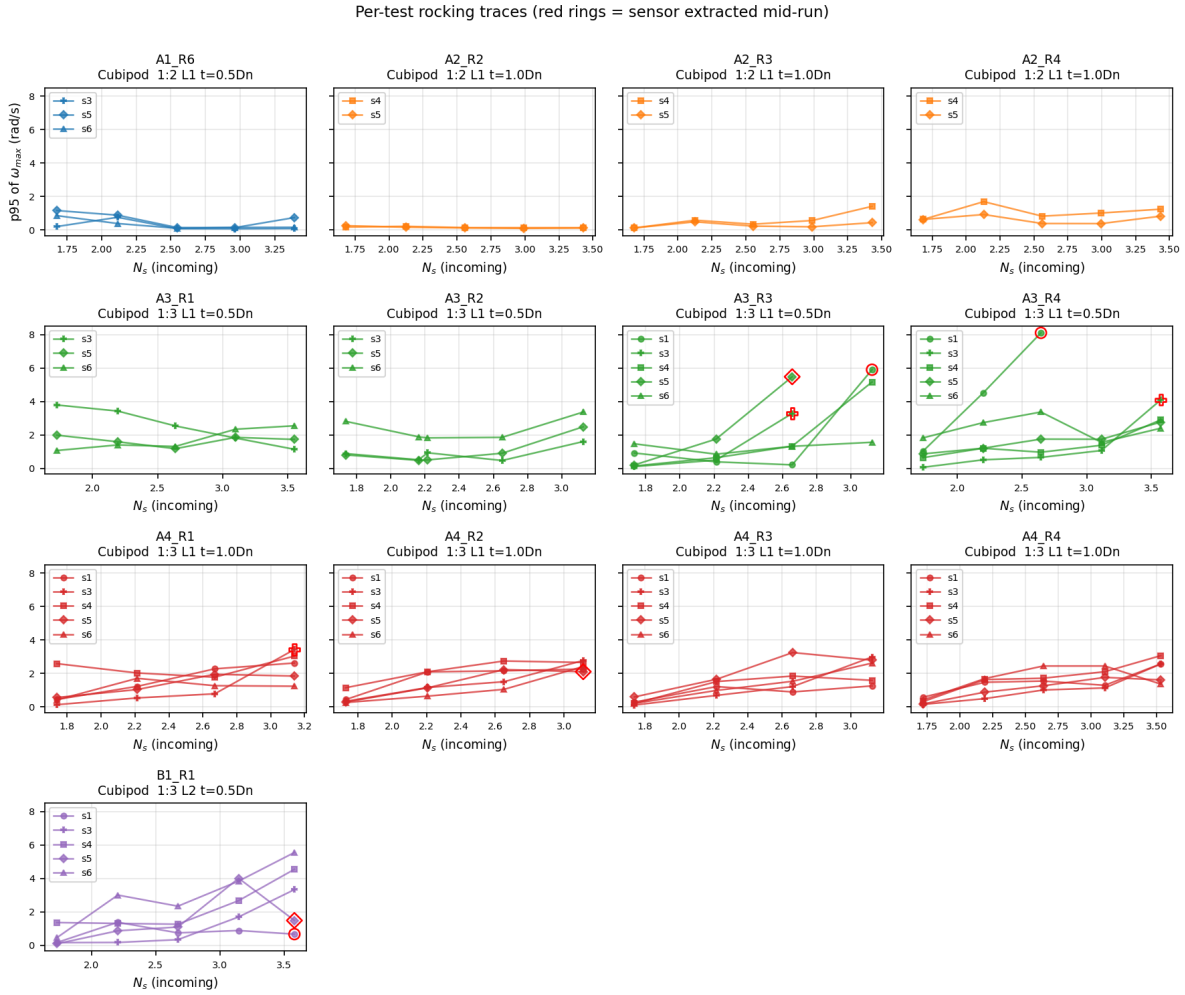


**Figure D.6:** Raw peak angular velocities $\omega_s$ over the incident significant wave height $H_{m0}$. Black rings denote the point of extraction from the armour layer. Subsequent data points from these units are excluded from aggregate metrics. The high initial peaks during the first step represent initial settling (compaction).

# Appendix E. Rocking-induced structural integrity

This appendix provides a first-order check on whether the rocking impacts measured by the embedded sensors could structurally break a prototype Cubipod over a 100 year design life. The check combines three established components, the measured rocking rates, a Cubipod drop-test failure curve, and the Palmgren-Miner fatigue rule, with several simplifying assumptions listed at the end of the appendix. Most assumptions are deliberately on the conservative side, so the result is intended as a safe upper bound rather than a structural design verification.

## E.1. Methodology

### E.1.1. From angular velocity to impact velocity

Each rocking event is a rotation of an armour unit about a contact point on the underlayer. The sensor records the peak angular velocity $|\omega|_{\text{max}}$ of the event, which is converted to a linear impact velocity at the striking face following (Hofland et al., 2023, eq. 3):

$$v_{i,\text{model}} \;=\; D_{\text{unit}} \cdot |\omega|_{\text{max}}, \tag{E.1}$$

where $D_{\text{unit}}$ is the lever arm from the rotation axis to the impact point. Hofland uses the unit height for Xbloc ($1.44\,D_n$). The Cubipod analogue is the tip-to-tip distance across two opposite face protrusions. With $\ell$ the side of the central cube and each protrusion a frustum of height $\ell/4$, $D_{\text{unit}} = \frac{3}{2}\ell = \frac{3}{2}(9/11)^{1/3}D_n \approx 1.40\,D_n$, where $(9/11)^{1/3}$ converts $\ell$ to $D_n$ through the total Cubipod volume. At model scale this gives $D_{\text{unit}} \approx 45.4$ mm.

Prototype impact velocities follow from Froude similarity:

$$v_{i,\text{proto}} \;=\; v_{i,\text{model}} \cdot \sqrt{n_L}, \qquad n_L = D_{n,\text{proto}}/D_{n,\text{model}}. \tag{E.2}$$

### E.1.2. Palmgren-Miner fatigue rule

Damage is accumulated with the linear Palmgren-Miner rule, as adopted in Eurocode 2 for concrete fatigue (European Committee for Standardization, 2004). Each impact consumes a fraction $1/N_{\text{fail}}(v_i)$ of the unit's fatigue life, and failure is taken to occur once the running sum $D$ reaches one:

$$D \;=\; \sum_i \frac{1}{N_{\text{fail}}(v_i)} \;\le\; 1. \tag{E.3}$$

### E.1.3. S-N curve from the Corredor drop tests

The number of impacts a unit survives at velocity $v$, $N_{\text{fail}}(v)$, is taken from the prototype drop tests of Corredor et al. (2010). They dropped 16-tonne Cubipods (nominal diameter $D_n \approx 1.93$ m) from a range of heights $h$, repeating each drop $n$ times. The reported mass loss collapses onto a single curve when expressed through an equivalent drop height

$$h_e \;=\; h \cdot n^a, \qquad a = 0.25, \tag{E.4}$$

with core breakage (relative mass loss above $4\,\%$) first reached at $h_{ec} = 3.1$ m. Converting drop height to impact velocity through $v = \sqrt{2gh}$ and solving for $n$ at the breakage height gives the S-N curve

$$N_{\text{fail}}(v) \;=\; \left(\frac{v_{\text{crit}}}{v}\right)^{2/a} \;=\; \left(\frac{v_{\text{crit}}}{v}\right)^{8}, \qquad v_{\text{crit}} = \sqrt{2g\,h_{ec}} \approx 7.80 \text{ m/s}, \tag{E.5}$$

where the velocity exponent $2/a = 8$ follows from $h \propto v^2$. The reference $v_{\text{crit}} = 7.80$ m/s is computed from the measured $h_{ec}$, not assumed. The exponent $a = 0.25$ is calibrated on few drops (of the order of tens of impacts) and is here extrapolated to $10^4$ to $10^6$ events. The sensitivity of the result to this value is examined in table E.1. The drop-test Cubipods used a strong $60$ MPa concrete (Corredor et al., 2008), higher than typical Dutch armour concrete (around C30/37). Using the drop-test value unadjusted is therefore on the strong side, flagged below.

### E.1.4. Wave climate and procedure

Damage is accumulated over a simplified IJmuiden 100 year wave-climate schedule: storms with $H_{m0} = 7.5,\ 6.5,\ 5.5,\ 4.5$ m occurring $1,\ 10,\ 100,\ 1000$ times respectively, with $5000$ waves per storm (a round middle value of the Rock Manual range $N = 1000$ to $3000$, extended in some Van der Meer formulations to $N = 7500$). The schedule is a Weibull-tail rule of thumb, and a site-specific scatter diagram would refine it. For each storm intensity, the lab events at the closest matching $N_s$ step are Froude-scaled to prototype with equation (E.2). Each event contributes $1/N_{\text{fail}}(v_i)$ to $D$. The lab-sample sum is rescaled to one prototype storm per unit by $n_{\text{waves per storm}}/(n_{\text{lab waves}} \cdot n_{\text{sensor runs}})$, and storm contributions are summed weighted by their lifetime occurrence count. The $8$ cm compaction step is excluded as one-time settling. For prototype sizes whose design-wave $N_s$ falls below the lab range ($D_n \gtrsim 3.5$ m), $D$ is projected by log-linear extrapolation of the in-range data.

## E.2. Results

Figure E.1 shows the static check (left) and the lifetime Palmgren-Miner sum $D$ (right) against prototype $D_n$. The worst single impact at the design wave reaches $0.40\, v_{\text{crit}}$ for the $1{:}3$ slope with $0.5\, D_n$ underlayer at $D_n = 2$ m. All other static unity checks are below $0.3$.

The lifetime sum $D$ stays below $1$ for every tested configuration. The most demanding case is $D \approx 0.17$ for the $1{:}3$ slope with $0.5\, D_n$ underlayer at the smallest size $D_n = 1.5$ m, a margin of about a factor $6$. The margin grows past a factor $50$ for $D_n \geq 2$ m and past $10^4$ for $D_n \geq 3$ m.

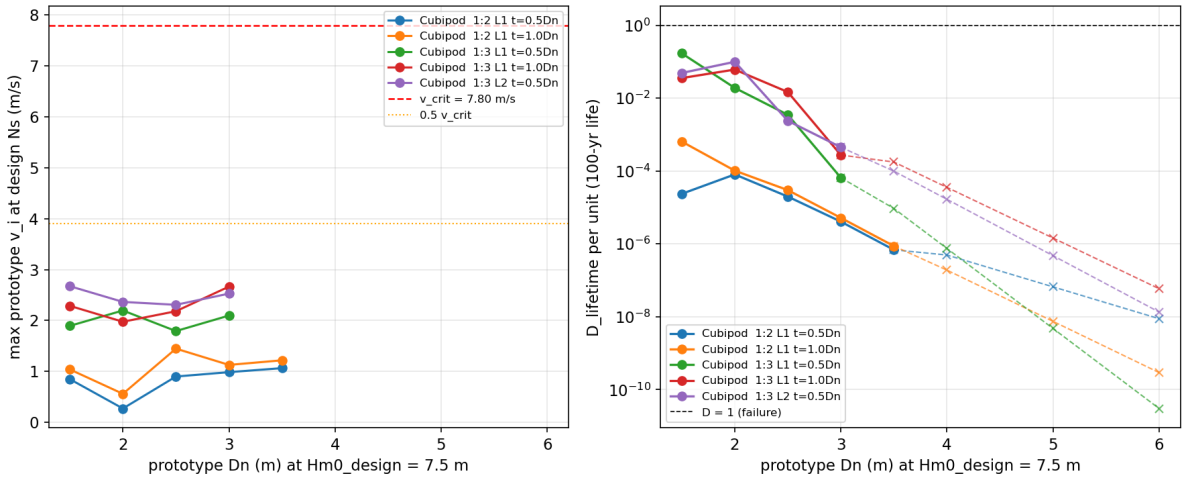


**Figure E.1:** Rocking-induced structural integrity check. Left: maximum prototype impact velocity compared with the $7.8$ m/s single-impact threshold. Right: lifetime Palmgren-Miner sum $D$ over 100 years. Solid lines denote lab-matched data ($D_n \leq 3.0$ m), dashed lines denote log-linear extrapolation. The criterion $D = 1$ is not exceeded.

Table E.1 gives a sensitivity scan of $D$ to the empirical exponent $a$ in equation (E.4). The purpose is to show how far $a$ would have to differ from the Corredor value of $0.25$ for the conclusion to flip, given that the exponent is calibrated on few drops and extrapolated over several orders of magnitude. Across the realistic range of $\pm 20\,\%$ around $a = 0.25$, $D$ stays well below the failure threshold, confirming that the conclusion is robust for standard unit sizes.

**Table E.1:** Sensitivity of the lifetime fatigue sum $D$ to the empirical exponent $a$ (from $h_e = h\,n^a$) for the most demanding configuration ($1{:}3$ slope, $0.5\,D_n$ underlayer). $D \geq 1$ indicates failure.

| $a$ | velocity exponent $2/a$ | $D$ at $D_n = 1.5$ m | $D$ at $D_n = 2.0$ m |
|---|---|---|---|
| $0.20$ | $10.00$ | $0.017$ | $0.00098$ |
| $0.222$ | $9.00$ | $0.053$ | $0.0041$ |
| $0.25$ (baseline) | $8.00$ | $0.169$ | $0.019$ |
| $0.286$ | $7.00$ | $0.549$ | $0.095$ |
| $0.30$ | $6.67$ | $0.810$ | $0.162$ |

## E.3. Assumptions and limitations

Because this check combines several disparate sources, its limitations heavily influence the safety margin:

- **Conservative impact metric:** $D_{\text{unit}}$ spans the entire unit height, and every rocking event is counted at its peak structural velocity, overestimating the average impact.
- **Extrapolated reference curve:** the S-N exponent $a = 0.25$ is calibrated on tens of drops and applied here to $10^4$ to $10^6$ events. Model units do not break, so the curve cannot be validated at the present scale.
- **Concrete strength:** the Corredor et al. (2010) drop tests used $60$ MPa concrete (about C50/60). A weaker Dutch prototype (around C30/37) would lower $v_{\text{crit}}$ and raise the lifetime damage roughly as $\sqrt{f_{ck}}$.
- **Wave climate placeholder:** the $10^0$ to $10^3$ storm exceedance schedule is a Weibull-tail rule of thumb, and a site-specific IJmuiden scatter diagram would refine it.
- **Failure mode scope:** the S-N curve targets whole-unit core breakage only. Slow processes such as abrasion, corner chipping and freeze-thaw degradation fall outside its scope.

Despite these limitations, the available margin across all $D_n \geq 2$ m units is so large (factor $> 50$) that intermediate deviations in concrete strength or extrapolation errors will not alter the conclusion that rocking does not cause structural breakage.

# Appendix F. Photogrammetric reconstruction (B1)

A photogrammetric reconstruction of the armour slope was performed as a three-dimensional damage assessment, applied to the double-layer test B1_R1 only to evaluate the workflow before extending it across the programme. The displacement maps and comparison with the top-view photographs are presented in section 5.2.6.

Image capture used an iPhone 15 with the RealityScan mobile app (Epic Games). Each of the seven scans (pre-test plus after each $H_{m0} = 10, 14, 16, 18, 20, 22$ cm step) comprised 190 to 240 frames. The compaction step and the $12$ cm step were skipped to limit acquisition time.

Cloud reconstruction ran in the RealityScan cloud service. Meshes were exported to Wavefront `.obj` via Sketchfab, sampled in CloudCompare 2.13 at $10^6$ points per cloud, and aligned to the pre-test scan by point-pair picking on stable features outside the armour zone (flume walls, toe, crest, taped markers). Cloud-to-cloud differencing then produces a per point displacement field. A reference stick gave a scale factor of $\sim 1.0$ on all scans, so no rescaling was applied.

The registration RMS errors per scan are $3.5, 4.0, 4.8, 1.4, 10.0$ and $9.0$ mm for $H_{m0} = 10$ to $22$ cm respectively. The mid-range scans resolve displacements above $5$ to $10$ mm reliably. For the two highest-$H_{m0}$ scans only the spatial damage pattern is interpretable, not absolute magnitudes.

The main limitations are as follows. Photo-only acquisition needs good texture and contrast (wet surfaces reduce both). Alignment precision depends on stable anchor features that become scarcer as damage progresses. Several manual steps (point-pair picking, scale verification) introduce operator-dependent variability.

figure F.1 shows the three main steps of the pipeline in RealityScan: the input photos and reconstructed point cloud, the same cloud coloured by reconstruction quality (used during acquisition to decide where to take extra photos), and the final 3D model after processing.

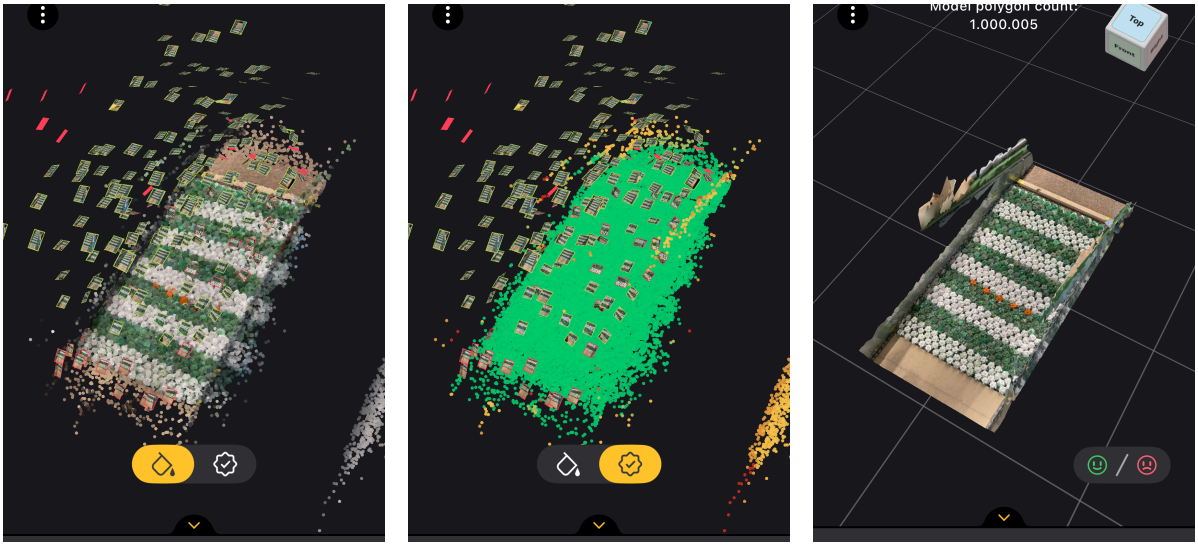


**(a)** Input photos and point cloud (real colours).

**(b)** Point cloud coloured by reconstruction quality.

**(c)** Final 3D model after processing.

**Figure F.1:** Three steps of the photogrammetric pipeline for B1_R1, shown in RealityScan. (a) The camera positions of the input photos overlaid on the reconstructed point cloud, with points coloured by their real flume colour. (b) The same point cloud, but with points coloured by reconstruction quality: green is good, yellow is moderate, red is poor. Red and yellow areas were used during the scan to decide where to take extra photos. (c) The final 3D model after cloud processing.

The two representative scans (first damage at $H_{m0,\text{inc}} = 13.3$ cm and best alignment at $H_{m0,\text{inc}} = 17.1$ cm, $RMS = 1.4$ mm) are presented in the results chapter (figure 5.6 of section 5.2.6). The full per step series follows below.

## F.1. Step-by-step displacement and photographic record

The six post-step displacement maps for B1_R1 are collected in figure F.2. The top-view photographic record of the same test is shown in figure F.3. Step labels below use the measured incident wave height $H_{m0,\text{inc}}$ at the gauge array (target values are listed in the figure captions).

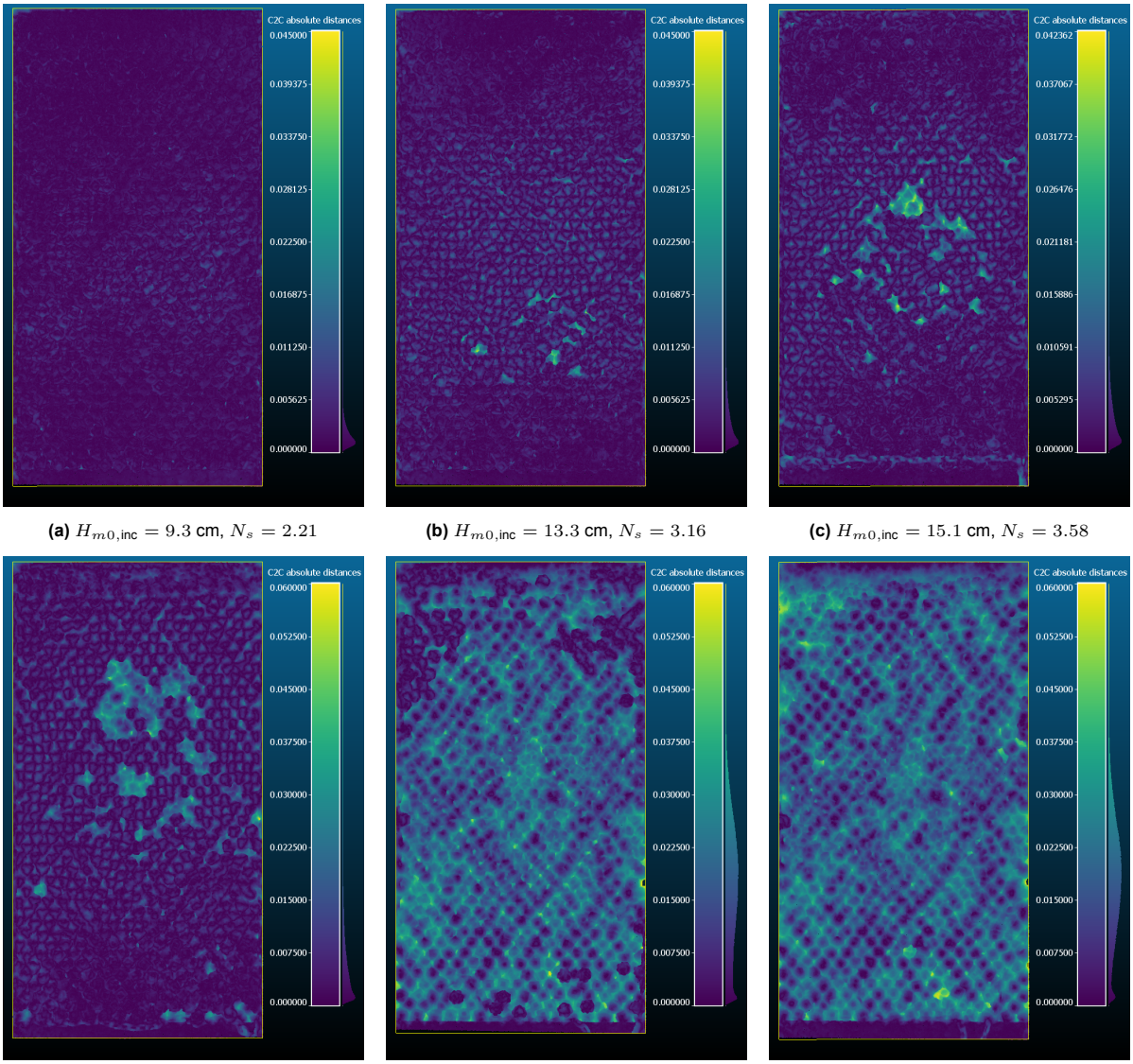


**(a)** $H_{m0,\text{inc}} = 9.3$ cm, $N_s = 2.21$ **(b)** $H_{m0,\text{inc}} = 13.3$ cm, $N_s = 3.16$ **(c)** $H_{m0,\text{inc}} = 15.1$ cm, $N_s = 3.58$

**(d)** $H_{m0,\text{inc}} = 17.1$ cm, $N_s = 4.06$ **(e)** $H_{m0,\text{inc}} = 18.9$ cm, $N_s = 4.49$ **(f)** $H_{m0,\text{inc}} = 19.5$ cm, $N_s = 4.63$

**Figure F.2:** Photogrammetric cloud-to-cloud displacement maps for test B1_R1, one per post-step scan. Top row: $H_{m0,\text{inc}} = 9.3, 13.3$ and $15.1$ cm (colour scale $0$ to $45$ mm). Bottom row: $H_{m0,\text{inc}} = 17.1, 18.9$ and $19.5$ cm (colour scale $0$ to $60$ mm). Viridis colour map, purple low and yellow high, absolute scale within each row. The two highest-$H_{m0,\text{inc}}$ panels should be read qualitatively because alignment RMS is approximately $10$ mm.

At $H_{m0,\text{inc}} \approx 9.3$ cm the slope showed only a small amount of compaction. The displacement map and the photograph show no damage.

At $H_{m0,\text{inc}} \approx 13.1$ cm the first damage appears. A few top-layer units were extracted around the still-water line, and the displacement map picks up localised peaks in that band.

At $H_{m0,\text{inc}} \approx 15.1$ cm more top-layer units came out at the water line, in the same way as the previous step. The visible gap moves upward in the photograph, but this is not new extraction higher on the slope: units from below were rolling down the face, so the gap follows them while new damage continues to occur at the water line.

At $H_{m0,\text{inc}} \approx 17.1$ cm the same pattern continued, but the toe also started to fail. The toe was repaired by hand before the next step because it had to remain stable for the rest of the test.

At $H_{m0,\text{inc}} \approx 18.9$ cm even though the toe was repaired, most of the top layer was gone including the toe. Damage now extended well below the water line. Only the top few rows still held top-layer units.

The bottom layer was fully intact.

At $H_{m0,\text{inc}} \approx 19.5$ cm the entire top layer was lost. The bottom layer crossed its single-layer threshold IDe,s (more than five units extracted) but did not collapse. It simply compacted, with the armoured length shortening from $137.5$ cm before this final step to $136$ cm at the end, down from $143$ cm as placed.

**(a)** Before testing

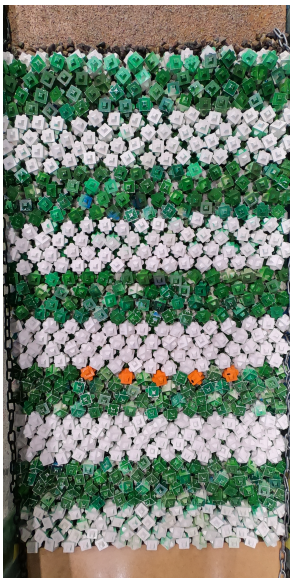

**(b)** After $H_{m0,\text{inc}} = 9.3$ cm, $N_s = 2.21$

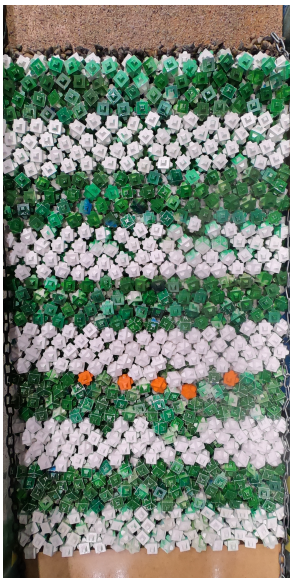

**(c)** After $H_{m0,\text{inc}} = 13.3$ cm, $N_s = 3.16$

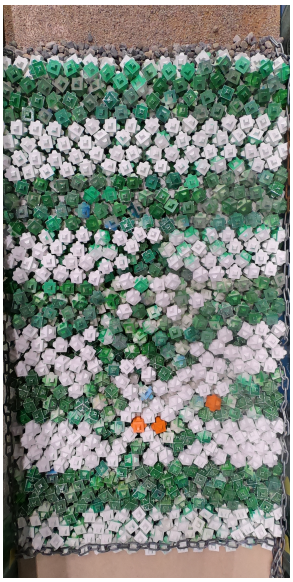

**(d)** After $H_{m0,\text{inc}} = 15.1$ cm, $N_s = 3.58$

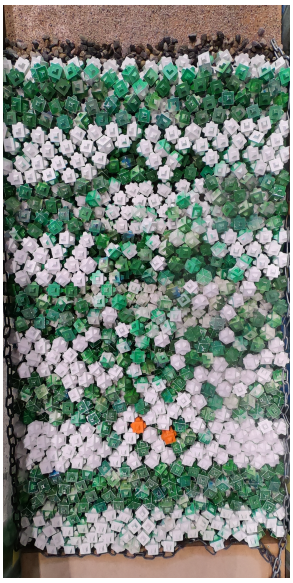

**(e)** After $H_{m0,\text{inc}} = 17.1$ cm, $N_s = 4.06$, toe repaired

**(f)** After $H_{m0,\text{inc}} = 18.9$ cm, $N_s = 4.49$

**(g)** After $H_{m0,\text{inc}} = 19.5$ cm, $N_s = 4.63$ (final)

**Figure F.3:** Top-view photographic record of armour-slope state during test B1_R1, ordered from pre-session through the final wave-height step. Photographs taken from above the slope with the flume drained for visibility. The $H_{m0} = 8$ cm compaction step and the $H_{m0} = 12$ cm step were not photographed. Each panel is rotated $90°$ counterclockwise and cropped by 5% on the (original) left and right and 20% on the (original) top and bottom to focus on the armoured slope.

# Appendix G. Extended stability results

This appendix presents full individual damage curves for all repetitions to assess test scatter, followed by an evaluation of the back-calculated Hudson coefficient and the derivation of the characteristic safety factors used for design.

## G.1. Repeatability of damage curves

In the following figures, damage ($N_{od}$) is plotted against stability ($N_s$) for all repetitions. Curves are grouped by slope and unit type. Marker shape distinguishes underlayer thickness ($t_f = 0.5\,D_n$: circles, $t_f = 1.0\,D_n$: squares). Marker colour indicates the as-built placement porosity. The IDe failure threshold ($N_{od} = 0.2$) is marked individually per test.

### G.1.1. Overview of all tests

Figure G.1 shows every single-layer test on its own panel, with IDe (red dashed) and complete failure (black dotted) marked per test. The presentation allows a direct test-by-test comparison. The slope-grouped overlays in the next subsections give a more quantitative view of the scatter between repetitions of the same configuration.

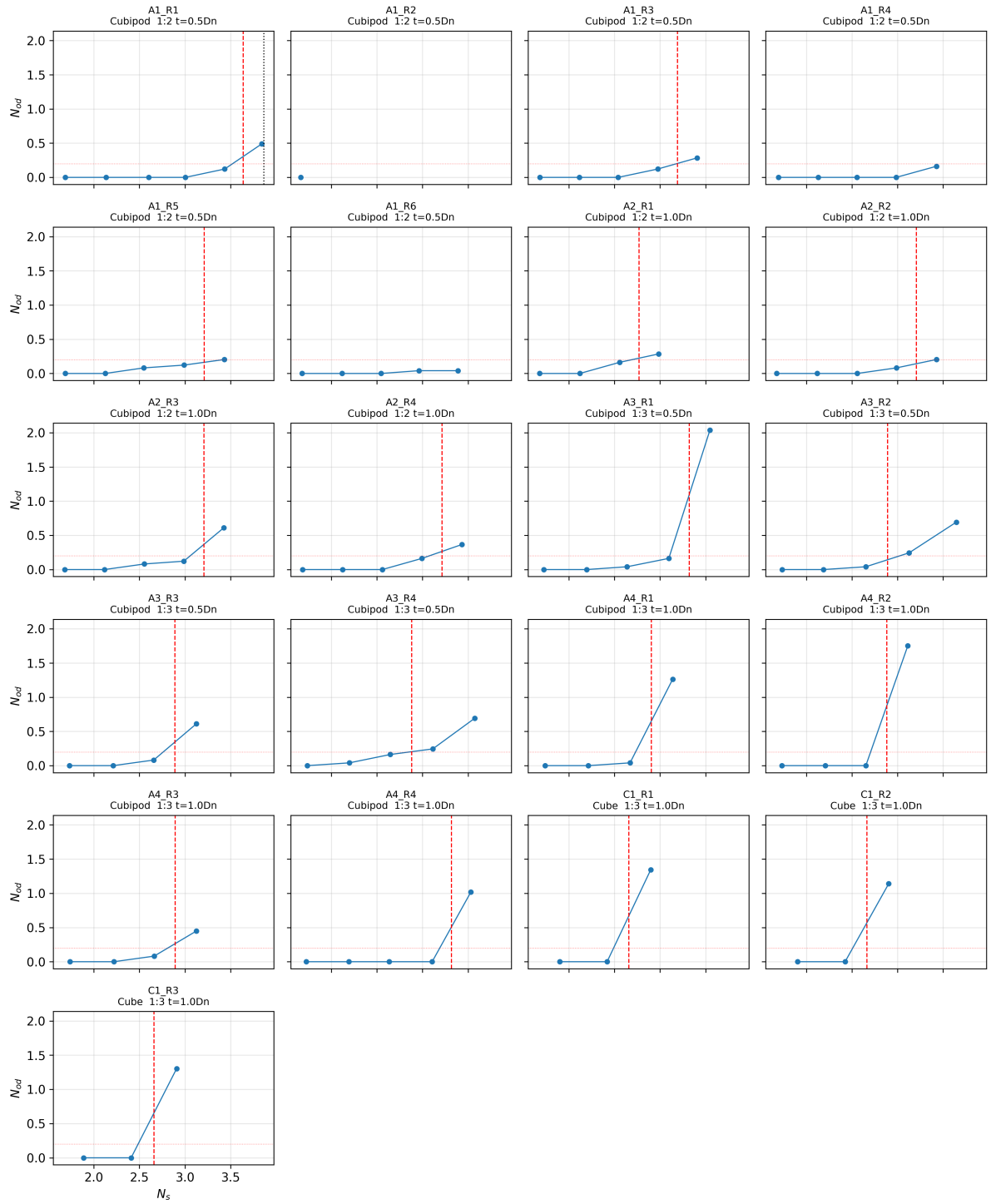


**Figure G.1:** Individual $N_{od}$–$N_s$ curves for every single-layer test. Red dashed line: IDe threshold ($N_{od} = 0.2$). Black dotted line: complete failure point.

The double-layer test B1_R1 is shown separately in figure G.2 because its destruction criterion IDe,d ($N_{od} = 2.0$ over both armour layers) differs from the single-layer criterion IDe,s used above.

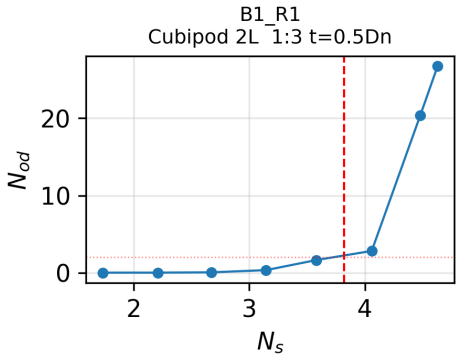


**Figure G.2:** Double-layer test B1_R1 (1:3 slope). The destruction threshold is the double-layer convention IDe,d ($N_{od} = 2.0$).

## G.1.2. Per configuration damage curves

Figure G.3 shows the individual damage curves grouped by configuration, with each panel pooling all repetitions of one (unit, slope) combination. Panel (a) gives the 1:2 Cubipod slope (A1 with $t_f = 0.5\,D_n$, A2 with $t_f = 1.0\,D_n$). Panel (b) the 1:3 Cubipod slope (A3 and A4). Panel (c) the single double-layer test B1_R1 (1:3, $t_f = 0.5\,D_n$, $n = 1$). Panel (d) the three cube repetitions on 1:3 (C1, $t_f = 1.0\,D_n$). The within-configuration scatter on 1:3 Cubipod (panel (b)) is wider than on 1:2 (panel (a)), reflecting the more rapid single-step failures observed on the flatter slope. The cube panel (d) shows almost completely overlapping curves, that is, minimal scatter between repetitions. With $n = 1$ for B1, no scatter assessment is possible from panel (c). It is included for completeness.

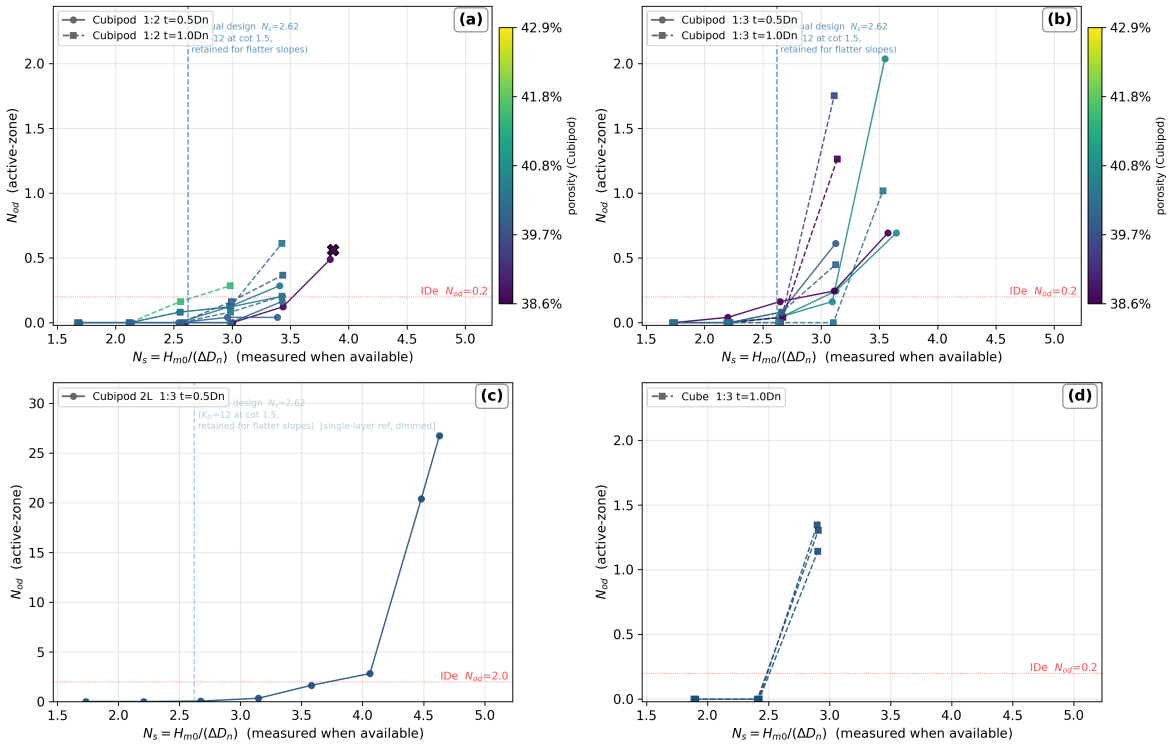


**Figure G.3:** Individual $N_{od}$–$N_s$ curves per (unit, slope) configuration. (a) Single-layer Cubipod, $\cot\alpha = 2$. (b) Single-layer Cubipod, $\cot\alpha = 3$. (c) Double-layer Cubipod, $\cot\alpha = 3$ (B1_R1, $n = 1$). (d) Single-layer cube, $\cot\alpha = 3$ (C1). Marker colour in the Cubipod panels encodes as-built placement porosity. The cube panel uses a fixed colour (uniform $n_v = 25.0\,\%$). Vertical blue dashed line in the Cubipod panels: Cubipod Manual permeable design $N_s = 2.62$ (dimmed in the double-layer panel because it is a single-layer reference). Red dotted horizontal: IDe threshold.

## G.2. Back-calculated Hudson coefficient

The Hudson stability coefficient, $K_D = N_s^3 / \cot\alpha$, assumes that unit stability does not decrease on flatter slopes. This holds for random rock or double-layer units, but not for interlocking single-layer armour like Cubipods (Medina and Gómez-Martín, 2016; Muttray and Reedijk, 2008). Interlocking relies on the along-slope gravity component, which weakens on flatter slopes.

The present data confirm this failure in Hudson scaling. The back-calculated $K_D$ drops by $51\,\%$, from a median of $16.5$ on the $1{:}2$ slope to $8.1$ on the $1{:}3$ slope (figure G.4). Because the required unit mass scales cubically with $N_s$, this drop substantially reduces design predictions. Hence, stability is reported exclusively as $N_s$ in the main text.

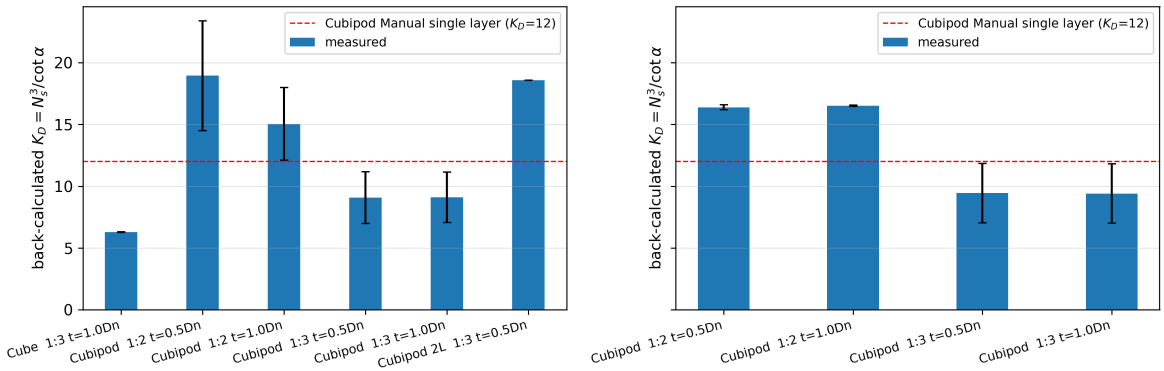


**Figure G.4:** Back-calculated $K_D = N_s^3 / \cot\alpha$ at IDe ($N_{od} = 0.2$). Left: all valid repetitions. Right: subset isolated to the $39$–$41\,\%$ porosity band. Dashed line: Cubipod Manual single-layer reference $K_D = 12$.

## G.3. Percentile-based safety factors

The derivation of the design stability number $N_{sd}$ and the percentile-based safety-factor method are presented in the main text (section 5.5). This appendix provides the supporting test statistics per configuration (table G.1), the resulting global safety factors per slope (table G.2), the reference calibration against the permeable Cubipod Manual (figure G.5), and a sensitivity analysis of the no-damage margin.

For the per slope design Gaussians (table G.2) the mean is taken per slope, using only the underlayer thicknesses tested in this thesis ($0.5$ and $1.0\,D_n$). For the Cubipod the standard deviation is pooled across all four single-layer series, both slopes and both underlayer thicknesses, into one value that is applied to both slopes while each slope keeps its own mean. Pooling a common standard deviation across groups that differ in mean but not in spread is the standard pooled-variance approach (Montgomery, 2017), and follows the way Medina et al. (2012) pool test data of one unit across conditions. A Levene test confirms the four series have statistically equal variance ($W \approx 0.02$, $p \approx 0.99$) (Levene, 1960). The standard error of a sample standard deviation scales as $1/\sqrt{2(n-1)}$, so the value from one four-test series, roughly $40\,\%$, falls to about $18\,\%$ when the four are pooled. By contrast, the mean of a single series is already determined to about $4$ to $8\,\%$ (its standard error, $\mathrm{CV}/\sqrt{n}$), so it does not benefit from pooling. For the cube on $\cot\alpha = 2$ the standard deviation additionally pools the $0$, $3$ and $5\,D_n$ series of (Ruijter, 2026) as a wider sample of scatter, and those series contribute to the standard deviation only, not to the mean.

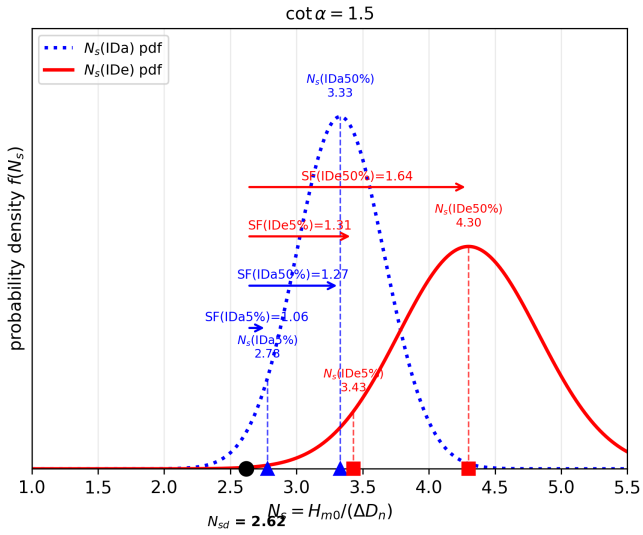


**Figure G.5:** Cubipod Manual reference at $\cot\alpha = 1.5$. The $1.31$ and $1.06$ boundaries dictate the $1.31$ anchor and $1.10$ no-damage requirement factor derived from Medina et al. (2012).

**Table G.1:** Overview of sample sizes, means ($\mu$), and standard deviations ($\sigma$) for $N_s$ at IDa and IDe thresholds. Values for cubes on $\cot\alpha = 2$ pool literature data (Ruijter, 2026) for variance.

| Unit | Slope | $t_f/D_n$ | $n_{\text{IDa}}$ | $\bar{N}_{s,\text{IDa}}$ | $\sigma_{\text{IDa}}$ | $n_{\text{IDe}}$ | $\bar{N}_{s,\text{IDe}}$ | $\sigma_{\text{IDe}}$ |
|---|---|---|---|---|---|---|---|---|
| Cubipod | 1:2 | 0.5 | 5 | 2.85 | 0.369 | 3 | 3.35 | 0.253 |
| Cubipod | 1:2 | 1.0 | 4 | 2.56 | 0.252 | 4 | 3.10 | 0.219 |
| Cubipod | 1:3 | 0.5 | 4 | 2.31 | 0.229 | 4 | 3.00 | 0.217 |
| Cubipod | 1:3 | 1.0 | 4 | 2.77 | 0.420 | 4 | 3.00 | 0.212 |
| Cube | 1:2 | 0.0 | 2 | 3.04 | 0.004 | 0 | — | — |
| Cube | 1:2 | 0.5 | 3 | 3.05 | 0.612 | 1 | 3.23 | — |
| Cube | 1:2 | 1.0 | 2 | 2.88 | 0.476 | 2 | 3.06 | 0.227 |
| Cube | 1:2 | 3.0 | 2 | 3.40 | 0.228 | 2 | 3.57 | 0.010 |
| Cube | 1:2 | 5.0 | 3 | 3.66 | 0.373 | 2 | 3.74 | 0.202 |
| Cube | 1:3 | 1.0 (C1) | 3 | 2.66 | 0.003 | 3 | 2.66 | 0.003 |

**Table G.2:** Global safety factors per slope from the $N_{sd}$ procedure. In all configurations $N_{sd}$ is set by the safety factor on IDa. The cube uses a stricter cap on IDa ($\text{SF}(\text{IDa}_{5\%}) = 1.20$) than the Cubipod ($1.10$), reflecting its greater brittleness.

| | $N_s$ at IDa | | $N_s$ at IDe | | | | | | |
|---|---|---|---|---|---|---|---|---|---|
| Unit, slope | $50\%$ | $5\%$ | $50\%$ | $5\%$ | $N_{sd}$ | $\text{SF}(\text{IDa}_{5\%})$ | $\text{SF}(\text{IDa}_{50\%})$ | $\text{SF}(\text{IDe}_{5\%})$ | $\text{SF}(\text{IDe}_{50\%})$ |
| Cubipod, $\cot\alpha = 2$ | 2.72 | 2.18 | 3.21 | 2.84 | 1.98 | 1.10 | 1.37 | 1.43 | 1.62 |
| Cubipod, $\cot\alpha = 3$ | 2.54 | 2.00 | 3.00 | 2.63 | 1.81 | 1.10 | 1.40 | 1.45 | 1.66 |
| Cube, $\cot\alpha = 2$ | 2.99 | 2.28 | 3.12 | 2.83 | 1.90 | 1.20 | 1.57 | 1.49 | 1.64 |
| Cube, $\cot\alpha = 3$ | 2.66 | 1.95 | 2.66 | 2.37 | 1.62 | 1.20 | 1.64 | 1.46 | 1.64 |
| *Reference* | | | | | | | | | |
| Cubipod 1L, $\cot\alpha = 1.5$, permeable (Medina et al., 2012) | 3.33 | 2.78 | 4.30 | 3.43 | 2.62 | 1.06 | 1.27 | 1.31 | 1.64 |

## G.3.1. Sensitivity of the no-damage margin

The chosen design values ($N_{sd} = 1.98$ for $\cot\alpha = 2$ and $N_{sd} = 1.81$ for $\cot\alpha = 3$) rely on a no-damage safety factor of $1.10$ applied to the $5\,\%$ characteristic IDa value. Table G.3 presents a sensitivity analysis of this margin. It demonstrates the direct trade-off between the selected margin against first damage and the resulting margin against ultimate destruction ($\text{SF}(\text{IDe}_{5\%})$).

Choosing a highly conservative no-damage margin (for example $1.20$) would lower the design stability numbers to $1.82$ and $1.67$, respectively. While this slightly increases the theoretical buffer against ultimate destruction, it incurs a severe penalty on the required unit mass, which is evaluated against constructability constraints in section 7.2.1.

**Table G.3:** Sensitivity of the design stability number $N_{sd}$ and the resulting ultimate-destruction margin $\mathrm{SF}(\mathrm{IDe}_{5\%})$ to the choice of the no-damage safety factor $\mathrm{SF}(\mathrm{IDa}_{5\%})$. The adopted margin is $\mathrm{SF}(\mathrm{IDa}_{5\%}) = 1.10$ (centre column).

| | $N_{sd}$ at varying $\mathrm{SF}(\mathrm{IDa}_{5\%})$ | | | $\mathrm{SF}(\mathrm{IDe}_{5\%})$ | | |
|---|---|---|---|---|---|---|
| Slope | $1.06$ | $1.10$ | $1.15$ | at $1.06$ | at $1.10$ | at $1.15$ |
| $\cot\alpha = 2$ ($N_s(\mathrm{IDa}_{5\%}) = 2.18$) | 2.06 | 1.98 | 1.90 | $\sim 1.38$ | $\sim 1.43$ | $\sim 1.49$ |
| $\cot\alpha = 3$ ($N_s(\mathrm{IDa}_{5\%}) = 2.00$) | 1.89 | 1.81 | 1.74 | $\sim 1.39$ | $\sim 1.45$ | $\sim 1.51$ |

# Appendix H. Reflection coefficient measurements

This appendix describes how the linear reflection coefficient $K_r$ was obtained, compares it with two reference curves, and gives a power-law fit calibrated on the present data.

## H.1. Determination of $K_r$

The surface elevation was sampled at 100 Hz on three resistance gauges seaward of the structure, with spacings of 0.60 m and 0.50 m (section 4.1). For each wave step the incident and reflected spectra were separated with the three-gauge method of Mansard and Funke (1980), over the steady part of the run (the central 1000–2000 s window) and the band $0.40$–$1.46$ Hz. This band spans about $f_p/2$ to $2.5\,f_p$ and excludes low-frequency drift and the gauge noise floor. The reflection coefficient is

$$K_r = \frac{H_{m0,\mathrm{ref}}}{H_{m0,\mathrm{inc}}}, \tag{H.1}$$

with $H_{m0,\mathrm{inc}}$ and $H_{m0,\mathrm{ref}}$ the spectral wave heights of the two components. All step-level values are listed in chapter B.

## H.2. Comparison with reference curves

Figure H.1 plots $K_r^2$ against the dimensionless wave parameter $\beta = (h/L_0)(H_I/L_0)$, with $L_0 = g\,T_p^2/(2\pi)$, next to two references. The dashed curves are the smooth impermeable sigmoid of Díaz-Carrasco et al. (2020), the no-armour upper bound. The horizontal lines are the armoured permeable formula of Zanuttigh and Van der Meer (2008) for $\gamma_f = 0.46$ (Cubipod) and $\gamma_f = 0.50$ (cube), calibrated for $\cot\alpha = 1.5$–$2.5$ and extrapolated at $\cot\alpha = 3$.

The measured values fall between the two references on both slopes. This is the expected position for an armour layer on an impermeable core: the armour adds dissipation relative to a smooth slope, while the impermeable core suppresses dissipation through the structure relative to a permeable rubble mound. Underlayer thickness has no visible effect, which indicates that $K_r$ is set by the armour surface rather than by the filter layer.

## H.3. Calibrated power-law fit

A power law

$$K_r^2 = a\,\beta^{\,b} \tag{H.2}$$

was fitted by least squares in $(\log_{10}\beta,\ \log_{10}K_r^2)$, with the compaction step excluded. Results per (slope, underlayer thickness) are given in table H.1.

The power law is the simplest form that matches the trend. One exponent $b$ captures the decrease of $K_r^2$ with $\beta$, and the five to seven steps per test do not support a more flexible model. The log-space fit weights the low cot 3 points equally to the higher cot 2 points. On the linear axis of figure H.1 the relation appears as a gentle curve. An Iribarren fit $K_r = \tanh(a\,\xi^{\,b})$ (Zanuttigh and Van der Meer, 2008) was rejected: the steepness was fixed at $s_0 = 0.040$, so $\xi$ barely varies within a slope and carries no information, whereas $\beta$ varies because $H_I$ and $L_0$ change independently between steps.

**Table H.1:** Power-law fit equation (H.2) of $K_r^2$ against $\beta$. $R^2$ is computed in $\log_{10}$ space. The Cubipod single-layer rows are the fits drawn in figure H.1. The double-layer (B1) and cube (C1) rows cover a single test each.

| Configuration | $d_F \,/\, D_n$ | $n$ | $a$ | $b$ | $R^2$ |
|---|---|---|---|---|---|
| Cubipod single, $\cot\alpha = 2$ (A1) | $0.5$ | 22 | $2.49 \times 10^{-3}$ | $-0.77$ | $0.60$ |
| Cubipod single, $\cot\alpha = 2$ (A2) | $1.0$ | 15 | $6.70 \times 10^{-4}$ | $-1.00$ | $0.68$ |
| Cubipod single, $\cot\alpha = 3$ (A3) | $0.5$ | 15 | $4.05 \times 10^{-5}$ | $-1.36$ | $0.83$ |
| Cubipod single, $\cot\alpha = 3$ (A4) | $1.0$ | 13 | $7.49 \times 10^{-5}$ | $-1.25$ | $0.80$ |
| Cubipod double, $\cot\alpha = 3$ (B1) | $0.5$ | 7 | $6.00 \times 10^{-6}$ | $-1.69$ | $0.85$ |
| Cube single, $\cot\alpha = 3$ (C1) | $1.0$ | 6 | $6.69 \times 10^{-3}$ | $-0.47$ | $0.78$ |

The exponent $b$ is negative throughout: steeper or longer waves dissipate more energy, so $K_r^2$ drops as $\beta$ grows. It steepens from about $-0.8$ on $\cot\alpha = 2$ to about $-1.3$ on $\cot\alpha = 3$, in line with stronger breaking on the gentler slope. Within each slope the $0.5\,D_n$ and $1.0\,D_n$ fits differ by less than the scatter, confirming the weak underlayer effect. The double-layer fit is steepest ($b \approx -1.69$), from the extra dissipation of the second layer. The cube fit is shallowest ($b \approx -0.47$), in line with its lower roughness factor.

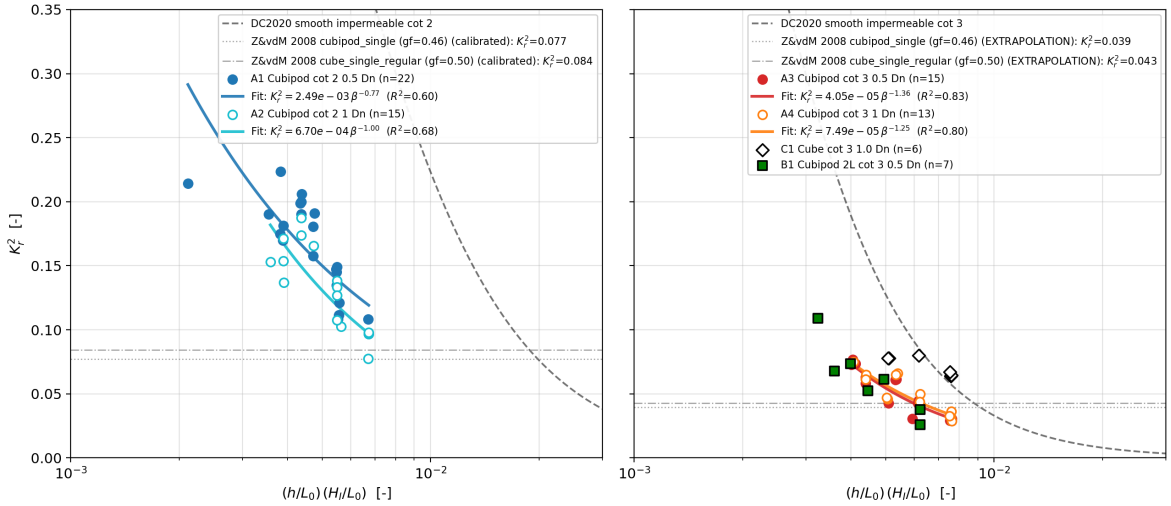


**Figure H.1:** Reflection coefficient squared against $\beta = (h/L_0)(H_I/L_0)$, left $\cot\alpha = 2$ and right $\cot\alpha = 3$ on shared axes. Solid lines: power-law fits per (slope, underlayer thickness) from table H.1, filled markers $0.5\,D_n$ and open markers $1.0\,D_n$. Cube (C1) and double-layer (B1) data are shown as context in the $\cot\alpha = 3$ panel without fit lines. Dashed lines: smooth impermeable sigmoid (Díaz-Carrasco et al., 2020). Dotted and dashdot lines: armoured permeable formula (Zanuttigh and Van der Meer, 2008), calibrated at $\cot\alpha = 2$ and extrapolated at $\cot\alpha = 3$.

# Appendix I. Rocking-sensor firmware and code

## I.1. Code repository access

The firmware for the embedded rocking sensors and the host-side readout tools are available online. The repository contains the TinyZero firmware, written in C++ and built with PlatformIO, together with the Python notebooks used to start a measurement and to download the recorded data over USB. It can be accessed by scanning the QR code in Figure I.1 or via the direct link below.

**Figure I.1:** QR code linking to the repository with the rocking-sensor firmware and readout code.

Direct URL:
`https://github.com/DePeterR/Thesis-Cubipods`